



VNIVERSITAT  
DE VALÈNCIA

Search for associated production of a Higgs  
boson and a single top quark in the  $2\ell + \tau_{had}$   
final state using proton-proton collisions  
at  $\sqrt{s} = 13$  TeV with the ATLAS detector

PhD Thesis

**Pablo Martínez Agulló**

Instituto de Física Corpuscular (IFIC)  
Departament de Física Atòmica, Molecular i Nuclear  
Programa de Doctorat en Física

Under the supervision of

**Carlos Escobar Ibáñez**  
and  
**Susana Cabrera Urbán**

València, 22nd December 2022



**Carlos Escobar Ibáñez,**  
investigador científico del Consejo Superior de Investigaciones Científicas, y

**Susana Cabrera Urbán,**  
científica titular del Consejo Superior de Investigaciones Científicas,

**Certifican:**

Que la presente memoria, **Search for associated production of a Higgs boson and a single top quark in the  $2\ell + \tau_{had}$  final state using proton-proton collisions at  $\sqrt{s} = 13$  TeV with the ATLAS detector**, ha sido realizada bajo su dirección en el Instituto de Física Corpuscular, centro mixto de la Universitat de València y del CSIC, por **Pablo Martínez Agulló**, y constituye su Tesis para optar al grado de Doctor en Física.

Y para que así conste, en cumplimiento de la legislación vigente, presenta en el Departamento de Física Atómica, Molecular y Nuclear de la Universidad de Valencia la referida Tesis Doctoral, y firman el presente certificado.

València, a DD de MES de 2023,

Carlos Escobar Ibáñez

Susana Cabrera Urbán



*C'est quoi ce bordel ???*

—DANIEL BOSSON,



# Preface

The Standard Model of particle physics is both incredibly successful and glaringly incomplete theory. It brings together all elementary particles that make up the known universe in a single theory. Among these, the top quark and the Higgs boson are of special interest because they can help to answer some of the open questions. The object of study of this thesis focusses in these two singular particles and its interplay.

The studies presented at this dissertation have been carried using an integrated luminosity of  $139 \text{ fb}^{-1}$  of proton-proton collision data at center-of-mass energy of 13 TeV collected by the ATLAS detector during the Large Hadron Collider (LHC) Run 2. Located at the European Organization for Nuclear Research, the LHC is the most powerful particle accelerator in the world and ATLAS one of its largest detectors. The experimental setup in which this work is contextualised is described in Chapter 3. The data and generation of Monte Carlo simulations within ATLAS is described in Chapter 4. The reconstruction and identification of physical objects is explained in Chapter 5.

The discovery of a Higgs boson by the ATLAS [1] and CMS [2] experiments in 2012 opened a new field for exploration in the realm of particle physics. In order to better understand Standard Model, it is of prominent interest to determine the Yukawa coupling of the Higgs boson to the top quark ( $y_t$ ), being the latter the most massive fundamental particle and, consequently, the one with the largest coupling to the Higgs boson.

The direct measurement of  $y_t$  is only possible at the LHC via two associated Higgs productions: with a top-quark-antiquark pair ( $t\bar{t}H$ ) and with a single-top quark with an additional parton ( $tHq$ ). While the  $t\bar{t}H$  just permits the determination of the magnitude of  $y_t$ , the only way of simultaneously measuring its sign and magnitude is through the  $tH$  production [3]. The possible observation of an excess of signal events with respect to the Standard Model prediction, would be an evidence of new physics in terms of CP-violating  $y_t$  coupling.

In this work it is presented a search for the  $tHq$  production in a final state with two light-flavoured-charged leptons (electrons or muons) and one hadronically-decaying  $\tau$  lepton (named  $2\ell + 1\tau_{\text{had}}$  channel). This search is exceptionally challenging due to the extremely small cross-section of the  $tHq$  process (70 fb [4]), and of the  $2\ell + 1\tau_{\text{had}}$  final-state channel, in particular, which only accounts for a 3.5% of the total  $tHq$  production.

Therefore, to distinguish the  $tHq$  signal events from background events, machine-learning techniques are used. Particularly, boosted-decision trees are employed to define signal-enriched regions as well as control regions that constrain the most important background processes. The most relevant backgrounds are those related to top-quark-antiquark-pair production without and with an additional boson ( $t\bar{t}$ ,  $t\bar{t}H$ ,  $t\bar{t}W$  and  $t\bar{t}Z$ ) and  $Z$  boson plus jets.

Additionally, to help identifying signal events within the data, the reconstruction of the event plays an important role. Different tools are used to retrieve the four momentum of the top quark and Higgs boson from the reconstructed objects. This information can be later used to build variables that help separating the signal events from the processes that mimic the  $2\ell + 1\tau_{\text{had}}$  signature. The reconstruction of the events is also enhanced by similar machine-learning methods since in the scenario in which the light-flavour leptons have the same sign, a priori, it is not possible to determine which lepton is originated from the Higgs boson and which from the top quark.

Significant suppression of the background events with jets wrongly selected as leptons or non-prompt leptons originating from heavy-flavour decays is achieved by demanding electrons and muons to pass strict identification and isolation requirements. Simultaneously, hadronic- $\tau$  leptons are demanded to pass the requirement of a recurrent-neural-network-based discriminator to reduce misidentifications from jets.

The tools and methods developed for the associated  $tHq$  production search are described in Chapter 6.

# Acknowledgements

This work would not have been possible without the invaluable assistance of a large number of people, whom I have been fortunate to meet. I would like to thank them all and dedicate this thesis to them.

Special mention to Stack Overflow, this thesis is as much yours as it is mine. Thanks.

Gracias gracias



# Contents

Preface	v
Acknowledgements	vii
<b>1 Theoretical Framework</b>	<b>1</b>
1.1 The Standard Model of particle physics . . . . .	1
1.1.1 Introduction to the SM and its elementary particles . . . . .	2
1.1.2 Quantum electrodynamics . . . . .	6
1.1.3 Electroweak interactions . . . . .	8
1.1.4 Quantum chromodynamics . . . . .	15
1.1.5 Particle masses . . . . .	18
1.1.6 Wrap up . . . . .	25
<b>2 Top quark and Higgs boson physics</b>	<b>31</b>
2.1 Top quark . . . . .	31
2.1.1 Top-quark discovery . . . . .	32
2.1.2 Top quark production at LHC . . . . .	33
2.1.3 Top-quark decay . . . . .	39
2.2 Higgs boson . . . . .	43
2.2.1 Higgs-boson discovery . . . . .	43
2.2.2 Higgs boson production at LHC . . . . .	44
2.2.3 Higgs-boson decay . . . . .	45
2.3 Top quark and Higgs boson interplay . . . . .	47

2.3.1	$t\bar{t}H$	48
2.3.2	$tHq$	49
<b>3</b>	<b>The ATLAS experiment at the Large Hadron Collider of CERN laboratory</b>	<b>53</b>
3.1	CERN	53
3.2	Large Hadron Collider	55
3.2.1	Machine design	56
3.2.2	Accelerator complex	58
3.2.3	LHC Experiments	59
3.2.4	LHC Computing grid	61
3.2.5	Energy, Luminosity and Cross-section	63
3.2.6	The Pile-up effect	69
3.2.7	Phenomenology of proton-proton collisions	70
3.3	ATLAS	73
3.3.1	Coordinate system	76
3.3.2	Inner Detector	77
3.3.3	Calorimeters	82
3.3.4	Muon Spectrometer	87
3.3.5	Magnet system	89
3.3.6	Trigger and Data Acquisition System	92
3.4	Alignment of the inner detector	93
3.4.1	Track based alignment	96
3.4.2	Alignment results during Run-2	98
3.4.3	Alignment towards Run-3	98
3.4.4	Web-based display for alignment monitoring	99
<b>4</b>	<b>Recording data and simulating events in ATLAS</b>	<b>101</b>
4.1	Data	101
4.1.1		101

4.1.2	.....	101
4.1.3	.....	101
4.2 Monte Carlo	.....	101
4.2.1 MC simulations	.....	102
4.2.2 MC generators	.....	103
<b>5 Object reconstruction and identification</b>		<b>105</b>
5.1 Tracking	.....	105
5.1.1 Sagitta method	.....	106
5.2 Vertices	.....	106
5.3 Electrons and photons	.....	106
5.4 Muons	.....	106
5.5 Jets	.....	106
5.5.1 Jet energy calibration and resolution	.....	107
5.5.2 Bottom quark induced jets	.....	108
5.6 Missing transverse energy	.....	108
5.7 Overlap removal	.....	108
<b>6 Search for rare associate <math>tHq</math> production</b>		<b>109</b>
6.1 Introduction	.....	109
6.2 Data and simulated events	.....	110
6.2.1 Single lepton triggers	.....	111
6.3 Object definition	.....	111
6.4 Signal	.....	111
6.4.1 Signal generation and validation	.....	111
6.4.2 Parton-level truth validation	.....	111
6.4.3 Lepton assignment	.....	112
6.4.4 Top quark and Higgs boson reconstruction	.....	116
6.5 Background estimation	.....	116
6.5.1 Fakes estimation	.....	117

6.5.2	Reducible backgrounds . . . . .	118
6.6	Event selection . . . . .	119
6.6.1	Preselection . . . . .	120
6.6.2	Discriminant variables . . . . .	121
6.6.3	BDT . . . . .	121
6.6.4	Signal Region . . . . .	122
6.6.5	Control Regions . . . . .	122
6.7	Systematic uncertainties . . . . .	123
6.7.1	Theoretical uncertainties . . . . .	123
6.7.2	Modelling uncertainties . . . . .	123
6.7.3	Experimental uncertainties . . . . .	123
6.8	Fit results . . . . .	123
6.8.1	Likelihood fit . . . . .	123
6.8.2	Strategy . . . . .	125
6.8.3	Fit with Asimov data . . . . .	125
6.8.4	Fit to data . . . . .	125
6.8.5	Results . . . . .	125
6.8.6	Data fit . . . . .	125
6.9	Combination results . . . . .	125
6.10	Conclusions . . . . .	125
<b>7</b>	<b>Conclusion</b>	<b>127</b>
<b>A</b>	<b>Effect of negative weights</b>	<b>129</b>
A.1	Negative weights uncertainties . . . . .	129
A.2	Statistical uncertainty of negative weights . . . . .	129
A.2.1	Errors in binned histograms . . . . .	131
A.3	Negative weights in MVA methods . . . . .	132

<b>Appendices</b>	<b>128</b>
<b>B Boosted Decision Trees</b>	<b>133</b>
B.1 How does a BDT work? . . . . .	133
B.1.1 Training . . . . .	134
B.1.2 Evaluation / Validation . . . . .	137
B.1.3 Application . . . . .	137
B.2 Treatment of negative weights . . . . .	137
B.3 Cross validation and $k$ -folding . . . . .	137
<b>Abbreviations</b>	<b>140</b>
<b>Bibliography</b>	<b>143</b>
<b>Summary of the results</b>	<b>157</b>
<b>Resum de la tesi</b>	<b>159</b>
1 Marc teòric . . . . .	159
1.1 El Model Estàndard . . . . .	159
1.2 La física del quark top . . . . .	159
1.3 La física del bosó de Higgs . . . . .	159
2 Dispositiu experimental . . . . .	159
3 L'experiment ATLAS del LHC al CERN . . . . .	160
3.1 El gran col·lisionador d'hadrons . . . . .	160
3.2 El detector ATLAS . . . . .	160
4 Mesura de la polarització del quark top al canal- $t$ . . . . .	160
4.1 Selecció d'esdeveniments . . . . .	160
4.2 Estimació del fons . . . . .	160
4.3 Fonts d'incertesa . . . . .	160
4.4 Resultats . . . . .	160
5 Recerca de processos $tH$ amb un estat final $2\ell + 1\tau_{\text{had}}$ . . . . .	160

---

5.1	Selecció d'esdeveniments . . . . .	160
5.2	Estimació del fons . . . . .	160
5.3	Fonts d'incertesa . . . . .	160
5.4	Resultats . . . . .	160
6	Conclusions . . . . .	160

# Chapter 1

## Theoretical Framework

### 1.1 The Standard Model of particle physics

Since the very first moment of our history, the humankind has pursued the knowledge of nature, has tried to understand and describe how the universe works at a fundamental level. In fact, the word physics comes from the Greek “*φύσικη*” which means “nature” [5][6]. Most of the enquires regarding this, can be boiled down to two basic questions: What are the ultimate building blocks of reality? and which are the rules that govern them?

In the 7<sup>th</sup> century BCE, the pre-Socratic philosopher Thales of Miletus already proclaimed that every event had a natural cause [7]. Later, to understand how the basic components of the matter were formed, the ancient Indian philosophers such as Kanada and Dignaga on the 6<sup>th</sup> century BCE and Greeks Democritus and Leucippus on the 5<sup>th</sup> century BCE, developed the atomism, which comes from “*ατομον*” meaning uncuttable or indivisible [8][9].

From then to our days, the search for the minute fragments that comprise the matter and its interactions has led us to the Standard Model (SM) of particle physics, one of the most successful scientific theories cultivated so far. This understanding of the universe can explain phenomena from behaviour of atoms to how stars burn.

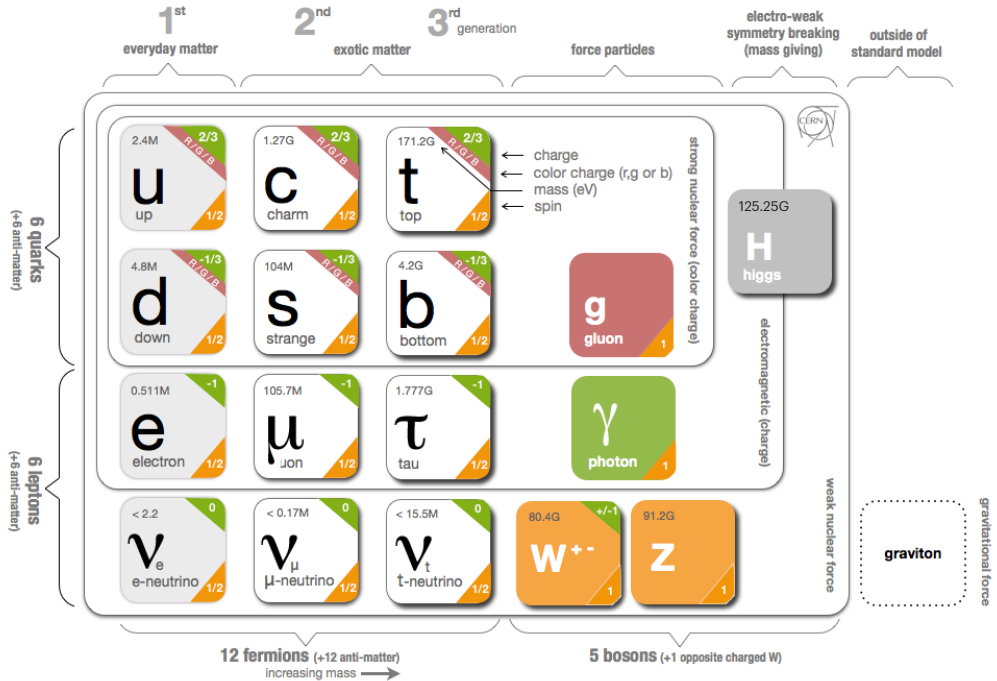


**Figure 1.1:** Fundamental particles of the Standard Model (image modified from [10]).

### 1.1.1 Introduction to the SM and its elementary particles

Based on Quantum Field Theory (QFT), the SM of particle physics provides the theoretical framework that constitutes what is currently accepted as the best description of particles physics. It aims to explain both all particles of matter and their interactions. The completion of the SM was a collaborative effort of several scientists during the second half of the 20<sup>th</sup>, being the current formulation finalised in the decade of 1970. A representation of the fundamental particles, i.e. particles that are not made of anything else, that compose the SM is presented in Figure 1.1. Most of these particles are unstable and decay to lighter particles within fractions of a second. As the scheme in Figure 1.1 indicates, the 12 fermions have their corresponding 12 anti-fermions and the quarks and gluons carry colour charge.

The SM is a gauge theory based on the symmetry group  $SU(3)_C \otimes SU(2)_L \otimes U(1)_Y$ , which describes all fundamental interactions except from the gravitational force<sup>1</sup>. This theory provides an explanation to strong, weak and electromagnetic interactions via the exchange of

<sup>1</sup>The gravitational interaction is described by Einstein's General Relativity (GR) [11].

Interaction	Theory	Mediator	Relative strength	Range (m)
Strong	QCD	$g$	1	$10^{-15}$
Electromagnetic	QED/EW	$\gamma$	$1/137$	$\infty$
Weak	EW	$W^\pm, Z$	$10^{-6}$	$10^{18}$
Gravitational	GR	-	$6 \times 10^{-39}$	$\infty$

**Table 1.1:** Typical strength of the fundamental interactions with respect to the strong interaction. Here the strength is understood as the coupling constant or gauge coupling parameter. In GR the gravitational interaction is not a force but the effect of the four-dimensional spacetime curvature and, hence, it has no mediator in this formalism.

the corresponding vector<sup>2</sup> bosons (spin-1 gauge fields). The mediation for the electromagnetic interaction (explicated in 1.1.2) is done by one massless photon ( $\gamma$ ), this force is invariant under the  $U(1)$  symmetry group. While for the weak interactions, guided by  $SU(2)$ , three massive bosons,  $W^+$ ,  $W^-$  and  $Z$ , act as mediators ( $m_{W^\pm} = 80.385 \pm 0.015$  GeV [12] and  $m_Z = 91.1876 \pm 0.02$  GeV [13]). Although the electromagnetic and weak interactions seem completely different at low energies, they are two aspects of the same force and can be described simultaneously by the  $SU(2)_L \otimes U(1)_Y$  symmetry group, which represents the so called Electro-Weak (EW) sector (detailed in Section 1.1.3). The strong force, with its eight massless gluons ( $g$ ), is described by the  $SU(3)_C$  colour group (see Section 1.1.4). All these interactions differ in their magnitude, range and the physical phenomena that describe. These features are summarised in Table 1.1, where not only the interactions of the SM are included but the gravitation is as well.

Apart from the vector bosons, there is one massive scalar boson, the Higgs boson ( $m_H = 125.25 \pm 0.17$  GeV). Through the interaction with this particle, all massive particles of Figure 1.1 gain their mass via the EW spontaneous symmetry breaking. This mechanism was first described by Englert, Brout [14] and Higgs [15], and its summarised in Section 1.1.5.1.

Before describing the fundamental interactions of the SM in the QFT formalism, let's introduce the main two types of particles according to their spin, i.e. intrinsic angular momentum: fermions and bosons.

## Fermions

The fermions are the particles that follow the Fermi-Dirac statistics, i.e. obey the Pauli exclusion principle [16], resulting in a distribution of particles over energy levels in which two elements with the same quantum numbers

---

<sup>2</sup>“Vector bosons” refer to all particles that have spin 1 in contrast to the “scalar boson’s” which have spin 0.

cannot occupy the same states. The fermions include all particles with half-integer spin: quarks, leptons and baryons. A baryon is a non-fundamental particle composed of an odd number of valence quarks may be encountered or experienced in everyday life is baryonic matter. Some examples of baryons are<sup>3</sup> the proton ( $u u d$ ), the neutron ( $d d u$ ),  $\Lambda$  ( $u d s$ ),  $\Lambda_c^+$  ( $u d c$ ) and  $\Sigma^+$  ( $u u s$ ). Apart from the 3-quark baryons, an exotic pentaquark state has been observed at LHCb experiment of the LHC [17].

The fundamental fermionic matter (Table 1.2) is organised in the three families of leptons and quarks:

$$\begin{bmatrix} \nu_e & u \\ e^- & d \end{bmatrix}, \begin{bmatrix} \nu_\mu & c \\ \mu^- & s \end{bmatrix}, \begin{bmatrix} \nu_\tau & t \\ \tau^- & b \end{bmatrix}$$

These three generations, which are defined as the columns in Figure 1.1, exhibit the same kind of gauge interactions and they only differ in their mass [18]. According to the EW symmetry, each family can be classified as:

$$\begin{bmatrix} \nu_\ell & q_u \\ \ell^- & q_d \end{bmatrix} \equiv \begin{pmatrix} \nu_\ell \\ \ell^- \end{pmatrix}_L, \begin{pmatrix} q_u \\ q_d \end{pmatrix}_L, \ell^-_R, q_{uR}, q_{dR}$$

(plus the corresponding antiparticles) where the subindices  $L$  and  $R$  stand from left and right handed particles respectively. This structure responds to the fact that left-handed particles convert different than right-handed ones under  $SU(2)$  transformations. The left-handed fields are  $SU(2)_L$  doublets and the right-handed ones  $SU(2)_L$  singlets. This difference is explained with more detail in Section 1.1.3.

The fundamental representation of  $SU(3)$  is a triplet, this is why each quark can appear in three different colours, whereas each antiquark can exhibit one of the corresponding “anticolours”.

The SM fermions properties are summarised in Table 1.2. As can be seen in its last rows, the neutrino flavour states do no correspond to the mass states ( $\nu_1, \nu_2, \nu_3$ ). What happens is that each flavour state is a quantum mechanical combination of neutrinos of different masses and viceversa. More details about the neutrino masses can be found in a dedicated text in Section 1.1.6.2

The fundamental fermions are usually understood as the fundamental building blocks of matter. However, while the building blocks are important, there is a point that also has to be taken into account, the force. Without

---

<sup>3</sup>Between round brackets, the valence quarks are shown.

Family	Name	Mass	Q
Quarks	Up ( $u$ )	$2.16^{+0.49}_{-0.26}$ MeV	$2/3$
	Down ( $d$ )	$4.67^{+0.48}_{-0.17}$ MeV	$-1/3$
	Charm ( $c$ )	$1.27 \pm 0.02$ GeV	$2/3$
	Strange ( $s$ )	$93^{+11}_{-5}$ MeV	$-1/3$
	Top ( $t$ )	$172.76 \pm 0.30$ GeV	$2/3$
	Bottom ( $b$ )	$4.18^{+0.03}_{-0.02}$ GeV	$-1/3$
Leptons	Electron ( $e^-$ )	$0.5109989461 \pm 0.0000000031$ MeV	$-1$
	Muon ( $\mu$ )	$105.6583745 \pm 0.0000024$ MeV	$-1$
	Tau ( $\tau$ )	$776.86 \pm 0.12$ MeV	$-1$
	Electron neutrino ( $\nu_e$ )	$\nu_e, \nu_\mu, \nu_e$	0
	Muon neutrino ( $\nu_\mu$ )	$\neq$	0
	Tau neutrino ( $\nu_\tau$ )	$\nu_1, \nu_2, \nu_3$	0

**Table 1.2:** Properties of the quarks and leptons. The electric charge, represented by Q, is presented in units of elementary charge ( $1.602 \times 10^{-19}$  C). The  $\nu_1, \nu_2, \nu_3$  are the neutrino mass eigenstates.

force these fermions would not interact with each other. The particles that mediate these interactions are the gauge bosons.

### Bosons

Bosons differ from fermions by obeying the Bose-Einstein statistics, thus, bosons are not limited to single occupancy for a determined state. In other words, the Pauli exclusion principle is not applied. All particles with integer spin are bosons; from the particles shown on the right columns of Figure 1.1 to the mesons. Mesons, along with baryons, are part of the hadron family, i.e. particles composed of quarks (see Section 1.1.4). The particularity of mesons is that they are formed from an equal number of quarks and antiquarks (usually one of each) bound together by strong interactions. Some examples of mesons are  $\pi^+$  ( $u \bar{d}$ ),  $\pi^0$  ( $\frac{u\bar{u}-d\bar{d}}{\sqrt{2}}$ ),  $K^+$  ( $u \bar{s}$ ) and  $J/\psi$  ( $c \bar{c}$ ).

The elementary vector bosons are the force carriers and presented in Table 1.1 while the Higgs boson is a fundamental particle as well.

### Gauge Invariance

Constituting one of the most successful theories of Physics, the SM is able to provide an elegant mathematical framework to describe the experimental physics results with great precision. Another key element to understand the SM is the concept of gauge invariance. As it is illustrated during the rest

of the Section 1.1, by demanding that the Lagrange density (also denoted as Lagrangian) invariant under local gauge transformations, the existence of the SM force-carrier bosons ( $\gamma$ ,  $W^+$ ,  $W^-$ ,  $Z$  and  $g$ ).

### 1.1.2 Quantum electrodynamics

The gauge invariance refers to the invariance of a theory under transformations which the theory is said to posses internal symmetry. The transformations which are applied in all space-time locations simultaneously are known as “global” transformations while the ones that vary from one point to another are “local”. Each local symmetry is the basis of a gauge theory and requires the introduction of its own gauge bosons as it is discussed in the following pages.

In QFT, particles are described as excitations of quantum fields that satisfy the corresponding mechanical field equations. The Lagrangians in QFT are used analogous to those of classical mechanics, where the equation of motion can be derived from the Lagrangian density function ( $\mathcal{L}$ ) and the Euler-Lagrange equations for fields:

$$\frac{\partial \mathcal{L}}{\partial \phi} - \partial_\mu \frac{\partial \mathcal{L}}{\partial (\partial_\mu \phi)} = 0,$$

where  $\partial_\mu = \frac{\partial}{\partial x^\mu}$  denotes the partial derivatives with respect to the four-vector  $x^\mu$  and  $\phi = \phi(\vec{x}, t)$  is the quantum field of a fermion or boson. The Lagrangian is used to express the dynamics of the quantum field. In QFT, Noether’s theorem [19] relates a symmetry in the  $\mathcal{L}$  to a conserved current.

The Dirac equation,  $(i\gamma^\mu \partial_\mu - m)\Psi(x) = 0$ , is one of the simplest relativistic field equations. Its Lagrangian describes a free Dirac fermion:

$$\mathcal{L}_0 = i\bar{\Psi}(x)\gamma^\mu \partial_\mu \Psi(x) - m\bar{\Psi}(x)\Psi(x), \quad (1.1)$$

being  $\Psi$  the wave function (spinor represented by four complex-valued components) of the particle,  $\gamma^\mu$  are the Dirac or gamma matrices,  $\{\gamma^0, \gamma^1, \gamma^2, \gamma^3\}$ ,  $m$  the rest-mass of the fermion and  $\bar{\Psi} = \Psi^\dagger \gamma^0$ , the hermitic conjugate of the wave function. The gamma matrices build a set of orthogonal basis vectors for covariant vectors in a Minkowski space. The first term of  $\mathcal{L}_0$  is the kinetic term while the second is the mass term.

This Lagrangian is invariant under  $U(1)$  global transformations such as:

$$\Psi(x) \xrightarrow{U(1)} \Psi'(x) \equiv \exp\{iQ\theta\}\Psi(x), \quad (1.2)$$

where  $Q\theta$  is a real constant. The phase of  $\Psi(x)$  is a pure convention-dependent quantity without a physical meaning since the observables depend on  $|\Psi(x)|^2$ .

However, if  $\theta$  was  $x$  dependent, the transformation 1.2 would be:

$$\Psi(x) \xrightarrow{U(1)} \Psi'(x) \equiv \exp\{iQ\theta(x)\}\Psi(x), \quad (1.3)$$

which is not longer a global transformation but a local transformation instead. The transformation in 1.3 would not let the  $\mathcal{L}_0$  in 1.1 invariant because the derivative in the kinetic term would go as:

$$\partial_\mu \Psi(x) \xrightarrow{U(1)} \exp\{iQ\theta\}(\partial_\mu + iQ\partial_\mu\theta)\Psi(x). \quad (1.4)$$

The gauge principle is the requirement that the  $U(1)$  phase invariance should hold locally. In order to do so, it is necessary to introduce an additional term to the Lagrangian so that when one applies  $\Psi'(x) \equiv \exp\{iQ\theta(x)\}\Psi(x)$ , the  $\partial_\mu\theta$  term is canceled in 1.4. To achieve this invariance, a term with the vector gauge field  $A_\mu$  is inserted. This field transforms as

$$A_\mu(x) \xrightarrow{U(1)} A'_\mu(x) \equiv A_\mu(x) + \frac{1}{e}\partial_\mu\theta \quad (1.5)$$

with a new  $D_\mu$ , which acts as follows:

$$D_\mu\Psi(x) \equiv [\partial_\mu + ieQA_\mu(x)]\Psi(x) \quad (1.6)$$

which transforms like the field:

$$D_\mu\Psi(x) \xrightarrow{U(1)} (D_\mu\Psi)'(x) \equiv \exp\{iQ\theta\}D_\mu\Psi(x).$$

The Lagrangian density can be defined by replacing the partial derivatives in  $\mathcal{L}_0$  (1.1) by the covariant derivative in 1.6:

$$\begin{aligned} \mathcal{L}_{QED} &\equiv i\bar{\Psi}(x)\gamma^\mu D_\mu\Psi(x) - m\bar{\Psi}(x)\Psi(x) \\ &= i\bar{\Psi}(x)\gamma^\mu[\partial_\mu + ieQA_\mu(x)]\Psi(x) - m\bar{\Psi}(x)\Psi(x) \\ &= i\bar{\Psi}(x)\gamma^\mu\partial_\mu\Psi(x) - \bar{\Psi}(x)\gamma^\mu eQA_\mu\Psi(x) - m\bar{\Psi}(x)\Psi(x) \\ &= \mathcal{L}_0 - eQA_\mu\bar{\Psi}(x)\gamma^\mu\Psi(x). \end{aligned} \quad (1.7)$$

The resulting Lagrangian is invariant under  $U(1)$  local transformation. When the conversions 1.3 and 1.5 take place, the effects of the transformation are canceled out. Along with the original Lagrangian ( $\mathcal{L}_0$ ), the  $\mathcal{L}_{QED}$  has an additional term describing the interaction between the fermion  $\Psi$  and the gauge field  $A_\mu$  with a strength proportional to the charge  $eQ$ . This

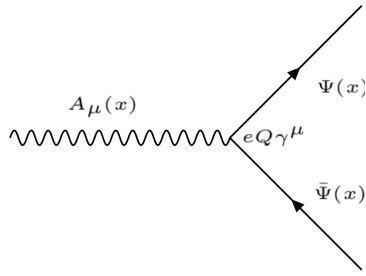


**Figure 1.2:** Three-point interaction vertex of QED.

term,  $eQA_\mu\bar{\Psi}\gamma^\mu\Psi$ , that has been generated only by demanding the gauge invariance under  $U(1)$ , is not other than the vertex of QED (Figure 1.2).

This new  $A_\mu$  term is the electromagnetic field and its quanta is the photon. A mass term containing  $A^\mu A_\mu$  is forbidden because it would violate the  $U(1)$  local invariance. In consequence, the mediator of the new  $A_\mu$  field, the photon, is predicted to be a massless particle. To make  $A_\mu$  a propagating field it is necessary to add the kinetic term of the field  $A_\mu$ :

$$\mathcal{L}_{kin} \equiv -\frac{1}{4}F_{\mu\nu}(x)F^{\mu\nu}(x), \quad (1.8)$$

where  $F^{\mu\nu} \equiv \partial_\mu A_\nu - \partial_\nu A_\mu$ . The kinetic term  $F_{\mu\nu}F_{\mu\nu}F^{\mu\nu}$  is already invariant under local  $U(1)$  phase transformations. From the QED Lagrangian in 1.7 and the kinetic term in 1.8, the Maxwell equations can be derived to describe electromagnetism, the infinite range<sup>4</sup> interaction that occurs between particles with electrical charge. The  $\mathcal{L}_{QED}$  with this kinetic term is written as:

$$\mathcal{L}_{QED} = \bar{\Psi}(x)(i\gamma^\mu\partial_\mu - m)\Psi(x) - eQ\bar{\Psi}(x)\gamma^\mu A_\mu\Psi(x) - \frac{1}{4}F_{\mu\nu}(x)F^{\mu\nu}(x). \quad (1.9)$$

### 1.1.3 Electroweak interactions

#### 1.1.3.1 Weak interactions and Symmetries

The weak interaction is mediated by the  $W^+$ ,  $W^-$  and  $Z$  massive gauge bosons. Due their large mass, the range of the interactions is within a scale of  $\sim 10^{-18}$  m. It is responsible for radioactive decays and flavour changing<sup>5</sup> decays of fermions such as the decay of the muon ( $\mu^- \rightarrow e^-\bar{\nu}_e\nu_\mu$ ).

Another particularity of this interaction is that it is the only interaction that violates several fundamental symmetries. There is a relation between

<sup>4</sup>Since the photon is (predicted to be) massless, the electromagnetic interaction has an infinite range.

<sup>5</sup>The leptonic charges are conserved.

symmetries and conservations laws which is known as Noether's theorem. Classical physics examples of how the symmetries leads to conserved quantities are:

- Invariance under change of time → Conservation of energy
- Invariance under translation in space → Conservation of momentum
- Invariance under rotation → Conservation of angular momentum

The three discrete symmetries that are fundamental for the SM formulation and are always hold for electromagnetic and strong interactions are:

- **Charge conjugation ( $\mathcal{C}$ ):** Replace positive quantum charges by negative charges and vice versa. It does not affect mass, energy, momentum or spin. Essentially, it is a transformation that switches all particles with their corresponding antiparticles.

$$\mathcal{C}\Psi(\vec{r}, t) = \bar{\Psi}(\vec{r}, t)$$

- **Parity ( $\mathcal{P}$ ):** Parity involves a transformation that changes the algebraic sign of the spatial coordinate system. It does not reverse time, mass, energy or other scalar quantities.

$$\mathcal{P} : \begin{pmatrix} x \\ y \\ z \end{pmatrix} \rightarrow \begin{pmatrix} -x \\ -y \\ -z \end{pmatrix} \quad \mathcal{P}\Psi(\vec{r}, t) = \Psi(-\vec{r}, t)$$

- **Time reversal ( $\mathcal{T}$ ):** Consists in flipping the sign of the time

$$\mathcal{T} : t \rightarrow -t \quad \mathcal{T}\Psi(\vec{r}, t) = \Psi(\vec{r}, -t)$$

The simultaneous combination of this three symmetries mentioned above results in the  $\mathcal{CPT}$  symmetry, a profound symmetry of QFT which is consistent through all experimental observations [20]. Meanwhile, the  $\mathcal{P}$ -symmetry and the  $\mathcal{C}$ -symmetry can be combined to create the  $\mathcal{CP}$ -symmetry, the product of the two transformations. The weak interaction violates  $\mathcal{P}$  and  $\mathcal{C}$  symmetries. It also violates the combined  $\mathcal{CP}$ -symmetry. Therefore, through the CPT theorem [21], if the  $\mathcal{CP}$  is violated,  $\mathcal{T}$  is violated as well to preserve the  $\mathcal{CPT}$  invariance [22].

### Parity violation

Previously theorised by Lee and Yang [23], the confirmation of the non-conservation of  $\mathcal{P}$  in weak interactions arrived with the Wu experiment in 1957 [24]. Studying the beta decay of the Cobalt-60, Wu and collaborators found that the neutrino and the antineutrino have the relative orientations of spin and linear momentum fixed. The neutrino spin is always opposite to the linear momentum, this is called left-handed particles. Meanwhile, for the antineutrinos, the momentum is always aligned in the same direction as the spin (right-handed particles). This causes the weak interactions which emit neutrinos or antineutrinos to violate the conservation of parity.

Only left-handed particles and right-handed antiparticles are sensitive to the weak force. Dirac fermion fields,  $\psi$ , exhibit chiral symmetry and the right and left handed chiral states can be expressed as:

$$\psi_L(x) = \frac{1}{2}(1 - \gamma_5)\psi(x) \equiv P_L\psi(x) \quad (1.10)$$

$$\psi_R(x) = \frac{1}{2}(1 + \gamma_5)\psi(x) \equiv P_R\psi(x) \quad (1.11)$$

with

$$\gamma^5 \equiv \gamma_5 \equiv \gamma^0\gamma^1\gamma^2\gamma^3 = \begin{pmatrix} 1 & 0 \\ 0 & 1 \end{pmatrix}$$

where  $P_L$  and  $P_R$  are known as projection operators. The last equality is valid in the Dirac representation.

### $\mathcal{CP}$ violation

While  $\mathcal{P}$  and  $\mathcal{C}$  are violated in a maximal way by the weak interactions, the product of these two discrete transformations,  $\mathcal{CP}$ , is still a good symmetry (left-handed fermions  $\leftrightarrow$  right-handed fermions). Experiences such as the Wu experiment respect the  $\mathcal{CP}$  symmetry and, in fact, in the  $\mathcal{CP}$  is a symmetry of nearly all the observed phenomena. However, in 1964 Cronin and Fitch discovered a slight (2%) violation of the  $\mathcal{CP}$  symmetry in the decays of neutral kaons [25]. The  $\mathcal{CP}$  violation plays a fundamental role to explain the dominance of matter over antimatter in the present universe. More information about the matter-antimatter asymmetry can be found in the dedicated text in Section 1.1.6.2.

Direct  $\mathcal{CP}$  violation is allowed in the SM if a complex phase is present in the CKM matrix (described below). The “direct”  $\mathcal{CP}$  violation is a phenomenon where the same decay process has a different probability for a particle than for an antiparticle. An example of strong global  $\mathcal{CP}$  asymmetry observed corresponds to the decay into two kaons and one pion. The probability of  $B^+ \rightarrow \pi^+ K^+ K^-$  is 20% higher than for  $B^- \rightarrow \pi^- K^+ K^-$ .

### CKM matrix

The eigenstates that interact through weak interactions, known as “weak eigenstates” ( $d'$ ,  $s'$ ,  $u'$ ), are different from the the physically observed mass eigenstates ( $d$ ,  $s$ ,  $u$ ). This make possible the charged-flavour-changing-weak decays trough the Cabibbo-Kobayashi-Maskawa (CKM) matrix. The CKM matrix,  $V_{CKM}$ , describes the mixing between the three generations of quarks in the SM. The coupling of two quarks  $i$  and  $j$  to a  $W$  boson is proportional to the CKM matrix element  $V_{ij}$ .

$$\begin{pmatrix} d' \\ s' \\ u' \end{pmatrix} = \begin{pmatrix} V_{ud} & V_{us} & V_{ub} \\ V_{cd} & V_{cs} & V_{cb} \\ V_{td} & V_{ts} & V_{tb} \end{pmatrix} \begin{pmatrix} d \\ s \\ u \end{pmatrix} \quad (1.12)$$

It is a  $3 \times 3$  unitary matrix described by four independent parameters: three angles ( $\theta_{ij}$ ) and one phase ( $\delta_{13}$ ). Different equivalent representations of the CKM matrix can be found in literature but the Particle Data Group recommends the standard CKM parameterisation:

$$V_{CKM} = \begin{pmatrix} c_{12}c_{13} & -s_{12}c_{13} & s_{13}e^{-i\delta_{13}} \\ -s_{12}c_{23} - c_{12}s_{23}s_{13}e^{i\delta_{13}} & -c_{12}c_{23} - s_{12}s_{23}s_{13}e^{i\delta_{13}} & s_{23}c_{13} \\ s_{12}s_{23} - c_{12}c_{23}s_{13}e^{i\delta_{13}} & -c_{12}s_{23} - s_{12}c_{23}s_{13}e^{i\delta_{13}} & c_{23}c_{13} \end{pmatrix} \quad (1.13)$$

where  $c_{ij} \equiv \cos \theta_{ij}$  and  $s_{ij} \equiv \sin \theta_{ij}$ , with  $i$  and  $j$  labelling the generations ( $i, j \in \{1, 2, 3\}$ ). The angles  $\theta_{12}$ ,  $\theta_{23}$  and  $\theta_{13}$  are known as Euler angles. The complex phase  $\delta_{13}$  allows the  $\mathcal{CP}$  violation [26].

The different elements of the CKM matrix are determined experimentally and are summarised in Table 1.3. As can be seen in this table, the largest values correspond to the diagonal elements of the CKM matrix. This implies that the processes that do not change the flavour are strongly preferred over the family-changing charged currents. For instance, for the top quark, the decay to any of the three down-type quarks is allowed but only  $|V_{td}|^2 \times 100\% = 0.0064\%$  of times will decay to a down quark and  $|V_{ts}|^2 \times 100\% = 0.14\%$  to a strange quark.

#### 1.1.3.2 Electroweak unification

At energies above the scale of the mass of the weak vector bosons ( $E_{EW} \sim m_Z \sim m_W \sim 100$  GeV), the electromagnetic and weak interactions are unified into the Electroweak (EW) force. In other words, electromagnetism and weak interactions are simultaneously described by the symmetry group  $SU(2)_L \otimes U(1)_Y$ . The subindex  $L$  refers to left-handed fields and  $Y$

CKM element	Value
$V_{ud}$	$0.9740 \pm 0.00011$
$V_{us}$	$0.22650 \pm 0.00048$
$V_{cd}$	$0.22636 \pm 0.0048$
$V_{cs}$	$0.97340 \pm 0.011$
$V_{cb}$	$0.04053^{+0.00083}_{-0.00061}$
$V_{ub}$	$0.00361^{+0.00011}_{-0.00009}$
$V_{td}$	$0.00854^{+0.00023}_{-0.00016}$
$V_{ts}$	$0.03978^{+0.00082}_{-0.00060}$
$V_{tb}$	$0.999172^{+0.000024}_{-0.000035}$

**Table 1.3:** Magnitude of the nine elements of the CKM matrix. The mean for the different measurements has been done by [27]. Note how the elements that refer to quarks of the same generation are favoured over the flavour-changing currents.

to the weak hypercharge. In contrast, at low energies, this interactions are treated as independent phenomena, the electromagnetism is described QED and the weak interaction by Fermi's theory.

In the EW model (Glashow-Salam-Weinberg model), two new quantum numbers are assigned to the particles of the SM: the weak isospin ( $\vec{T}$ ) and  $Y$ . Here, the left-handed chiral states of fermions form isospin doublets ( $\chi_L$ ) with  $T_3 = \pm 1/2$  and the right-handed form chiral states are composed of isospin singlets ( $\chi_R$ ) with  $T_3 = 0$ . For a particle,  $T_3$  is the third component of the  $\vec{T}$ , which is related to the electric charge ( $Q$ ) and the  $U(1)$  hypercharge by Gell-Mann-Nishijima relation:

$$Q = T_3 + \frac{1}{2}Y \quad (1.14)$$

With this expression, the electromagnetic coupling and the electroweak couplings are connected. Having  $\chi_L$  with  $T_3 = \pm 1/2$  and  $\chi_R$  with  $T_3 = 0$  implies that a  $SU(2)$  weak interaction can rotate left-handed particles (i.e. convert a left-handed  $e^-$  into a left-handed  $\nu_e$  emitting a  $W^-$ ) but cannot do the same with right-handed.

Using the gauge invariance principle it is possible to find the QED and QCD Lagrangians, as it is described in Sections 1.1.2 and 1.1.4 respectively.

The free Lagrangian, as in the case of QED and QCD is:

$$\begin{aligned} \mathcal{L} &= i \sum_{j=1}^3 \bar{\Psi}(x) \gamma^\mu \partial_\mu \Psi(x) \\ &= i \sum_{j=1}^3 \bar{\chi}_L(x) \gamma^\mu \partial_\mu \chi_L(x) + i \sum_{k=1}^3 \bar{\chi}_R(x) \gamma^\mu \partial_\mu \chi_R(x) \end{aligned} \quad (1.15)$$

where the wave function  $\Psi$  has been spited into the left isospin doublets  $\chi_L$  and and right isospin singlets  $\chi_R$ . The indices  $j$  and  $k$  run over the three generations of the SM. This Lagrangian should be invariant when a gauge transformation under the  $SU(2)_L \times U(1)_Y$  symmetry group in the flavour space is applied:

$$\chi_L(x) \xrightarrow{SU(2)_L \times U(1)_Y} \chi'_L(x) = \exp\{i\alpha^n \tau_n\} \exp\{i\beta y\} \chi_L(x) \quad (1.16)$$

$$\chi_R(x) \xrightarrow{SU(2)_L \times U(1)_Y} \chi'_R(x) = \exp\{i\beta y\} \chi_R(x) \quad (1.17)$$

with  $\alpha, \beta \in \mathbb{R}$  and  $n \in \{1, 2, 3\}$ . This transformation is given by the generators of  $SU(2)_L \times U(1)_Y$ , i.e. the Pauli matrices  $(\tau_n)$  and the weak hypercharge  $y$ . Note that  $SU(2)_L$  transformation,  $\exp\{i\alpha^n \tau_{nu}\}$ , only acts on the doublet fields. This term containing the Pauli matrices is non-abelian like in QCD and, like in QCD, this leads to self-interacting terms.

To ensure invariance under  $SU(2)_L \times U(1)_Y$ , four different gauge fields have to be added (three from  $SU(2)$  and one from  $U(1)$ ). Four is also the correct number of gauge bosons needed to describe EW interactions:  $W^+$ ,  $W^-$ ,  $Z$  and  $\gamma$ . While the three week isospin currents couple to the triplet of vector bosons  $W_\mu^n$  with  $n \in \{1, 2, 3\}$ , the weak hypercharge couples to an isosinglet  $B_\mu$ . The fields  $W_\mu^1$  and  $W_\mu^2$  are electrically charged whereas  $W_\mu^3$  and  $B_\mu$  are neutral fields. The EW covariant derivative is defined as:

$$D^\mu \chi_{L_j}(x) = [\partial_\mu - ig \frac{\tau_i}{2} W_\mu^i(x) - ig' \frac{y_j}{2} B_\mu(x)] \chi_{L_j}(x) \quad i \in [1, 2, 3] \quad (1.18)$$

$$D^\mu \chi_{R_j}(x) = [\partial_\mu - ig' \frac{y_j}{2} B_\mu(x)] \chi_{R_j}(x), \quad (1.19)$$

where  $g$  and  $g'$  are the interaction couplings to  $W_\mu^i$  isotriplet and the  $B_\mu$  isosinglet.

Using the derivatives in Equations 1.18 and 1.19, the Lagrangian in 1.20 is already invariant under local  $SU(2)_L \times U(1)_Y$  transformations:

$$\mathcal{L} = i \sum_{j=1}^3 \bar{\chi}_L^j(x) \gamma^\mu D_\mu \chi_L^j(x) + i \sum_{k=1}^3 \bar{\chi}_R^k(x) \gamma^\mu D_\mu \chi_R^k(x) \quad (1.20)$$

Finally, if kinetic terms for the gauge bosons are included in 1.20, the EW SM Lagrangian is obtained:

$$\begin{aligned} \mathcal{L}_{EW} = & i \sum_{j=1}^3 \bar{\chi}_L^j(x) \gamma^\mu D_\mu \chi_L^j(x) + i \sum_{k=1}^3 \bar{\chi}_R^k(x) \gamma^\mu D_\mu \chi_R^k(x) \\ & - \frac{1}{4} W_{\mu\nu}^n(x) W_n^{\mu\nu}(x) - \frac{1}{4} B_{\mu\nu}(x) B^{\mu\nu}(x) \end{aligned} \quad (1.21)$$

Where the addition of kinetic terms gives rise to cubic and quadratic self-interactions among the gauge fields. Note that the mass terms of the fields are forbidden in order to ensure local gauge invariance and since the observed  $W^+$ ,  $W^-$  and  $Z$  bosons have masses different from zero, for the moment let's assume that something breaks the symmetry generating the observed masses.

The in  $\mathcal{L}_{EW}$  in 1.21 can be divided in two different parts according to the charge of the bosons: charged currents and neutral currents. Relating the charged currents ( $W_\mu^1$  and  $W_\mu^2$ ) to the  $W^+$  and  $W^-$  bosons of the SM and the neutral ( $W_\mu^3$  and  $B_\mu$ ) ones with the  $Z$  and  $\gamma$ , it is possible to build linear combinations fo the original gauge fields that define the SM bosons.

Therefore, from the charged-current interactions, the  $W^+$  and  $W^-$  bosons are:

$$W^\pm \equiv \frac{1}{\sqrt{2}}(W_\mu^1 \mp i W_\mu^2) \quad (1.22)$$

While for the neutral-current these combinations can be defined as a rotation of the so called Weinberg (or weak mixing) angle  $\theta_W$ :

$$\begin{pmatrix} W_\mu^3 \\ B_\mu \end{pmatrix} \equiv \begin{pmatrix} \cos \theta_W & \sin \theta_W \\ -\sin \theta_W & \cos \theta_W \end{pmatrix} \begin{pmatrix} Z_\mu \\ A_\mu \end{pmatrix}$$

Rewriting this equation, the photon and  $Z$ -boson fields are

$$A_\mu = B_\mu \cos \theta_W + W_\mu^3 \sin \theta_W \quad Z_\mu = -B_\mu \cos \theta_W + W_\mu^3 \sin \theta_W \quad (1.23)$$

In order to ensure that this  $A_\mu$  is the one of QED, apart from the Gell-Mann-Nishijima relation (Equation 1.14), it is requiered that the couplings of the  $\gamma$ ,  $W^\pm$  and  $Z$  satisfy the relation:

$$g \sin \theta_W = g' \cos \theta_W = e \quad (1.24)$$

Within the unified EW model, once  $\theta_W$  is known, the mass of  $Z$  is specified. Current measurements of  $\theta_W$  give a value of  $\sin^2 \theta_W = 0.2310 \pm 0.0005$  [28].

There is no mass term for the bosons in the EW Lagrangian that has been obtained in 1.21 by demanding the  $SU(2)_L \times U(1)_Y$  local invariance, which enters in contradiction with the experimental observations for the  $W$  and  $Z$  bosons ( $m_{Z,W} \sim 80$  GeV). The introduction of such a mass term would break the symmetry, however, the it is possible to add the mass for the  $W$  and  $Z$  bosons without loosing the properties of the symmetry. The method to do so is known as Englert–Brout–Higgs–Guralnik–Hagen–Kibble mechanism or, more commonly, just as Higgs mechanism. This mechanism is described in Section 1.1.5.



(a) Quark colours combine to be colourless. (b) Antiquark colours also combine to be colourless.

**Figure 1.3:** Colour charge combinations for quarks and antiquarks. Due to the confinement, the hadrons are colourless.

## 1.1.4 Quantum chromodynamics

### 1.1.4.1 Quarks and colour

QCD is QFT-based theory for describing the strong interactions between quarks and gluons (partons). This type of interaction is the responsible of the nuclear force, the one that acts between the protons and neutrons of atoms binding them together. Without the strong force, the protons inside the nucleus would push each other apart due to the electromagnetic repulsion. It also holds the quarks within a hadron together.

QCD is based in the  $SU(3)$  symmetry group and its name derives from the “colour” charge, an analogous to the electric charge of QED but for strong interactions. The colour charge was introduced in 1964 [29] to explain how quarks could coexist within some hadrons apparently having the same quantum state without violating the Pauli exclusion principle. To satisfy the Fermi-Dirac statistics it is necessary to add an additional quantum number, the colour, to the theory. Each species of quark ( $q$ ) may have three different colours ( $q^\alpha$ ,  $\alpha = 1, 2, 3$ ): red, green, blue. Baryons and mesons are described then by the colour singlet combinations:

$$B = \frac{1}{\sqrt{6}} \epsilon^{\alpha\beta\gamma} |q_\alpha q_\beta q_\gamma\rangle \quad M = \frac{1}{\sqrt{3}} \epsilon^{\alpha\beta} |q_\alpha \bar{q}_\beta\rangle$$

Additionally, it is postulated that all hadrons must have a global neutral colour charge, i.e. the hadrons must be “colourless”. This assumption is known as confinement hypothesis and it is made to avoid the existence of non-observed extra states with non-zero colour. It is called colour confinement because it implies that it is not possible to observe free quarks since they carry colour charge and, hence, they have to be confined within colour-singlet combinations. Figure 1.3 depicts how different colours and anticolours combine to create the “colourless” state.

### 1.1.4.2 Gauge invariance for $SU(3)$

The dynamics of the quarks and gluons are controlled by the QCD Lagrangian. Using the power of the gauge invariance principle it is possible to deduce  $\mathcal{L}_{QCD}$  similarly to the reasoning developed in Section 1.1.2. Firstly, let's denote a quark field of colour  $\alpha$  and flavour  $f$  by  $q_f^\alpha$ . The vector  $q_f^T \equiv (q_f^1, q_f^2, q_f^3)$  is defined under the  $SU(3)$  colour space, meaning that each dimension corresponds to a colour. The Lagrangian

$$\mathcal{L}_0 = \sum_f \bar{q}_f (i\gamma^\mu \partial_\mu - m_f) q_f \quad (1.25)$$

is invariant under global  $SU(3)$  transformation in the colour space,

$$q_f^\alpha \rightarrow (q_f^\alpha)' = U_\beta^\alpha q_\beta^\beta, \quad UU^\dagger = U^\dagger U = 1, \quad \det U = 1. \quad (1.26)$$

In the  $SU(N)$  algebra,  $SU(N)$  is the group of  $N \times N$  unitary matrices ( $U$ ) which can be written in the form  $U = \exp\{i(\lambda^a/2)\theta_a\}$  with  $a = 1, 2, \dots, N^2 - 1$ . Therefore, the  $SU(3)$  matrices can be written as

$$U = \exp\left\{i\frac{\lambda^a}{2}\theta_a\right\} \quad (1.27)$$

where the index  $a$  goes from 1 to 8 for the arbitrary parameter  $\theta_a$  and  $\frac{\lambda^a}{2}$ , which denotes the fundamental representation of the  $SU(3)$  algebra. The Einstein notation for summation over repeated indices is implied. The matrices  $\lambda^a$  are traceless and satisfy the commutation relations [18]:

$$\left[\frac{\lambda^a}{2}, \frac{\lambda^b}{2}\right] = if^{abc}\frac{\lambda^c}{2} \quad (1.28)$$

, being  $f^{abc}$  the  $SU(3)_C$  structure constants, which are real and totally antisymmetric.

To satisfy the gauge invariance requirement, the Lagrangian has to be invariant under  $SU(3)$  local transformations, i.e, transformations in which the phase is dependent of the space-time location,  $\theta_a = \theta_a(x)$ . To fulfil the condition, the quark derivatives in the Lagrangian in 1.25 have to be substituted by covariant objects. Since there are eight independent gauge parameters, eight different gauge bosons  $G_a^\mu(x)$  are needed<sup>6</sup>. This bosons are the eight gluons and the new covariant objects are:

$$D^\mu q_f \equiv \left[ \partial_\mu + ig_s \frac{\lambda^a}{2} G_a^\mu(x) \right] q_f \equiv [\partial_\mu + ig_s G^\mu(x)] q_f$$

---

<sup>6</sup>The eightfold multiplicity of gluons is labeled by a combination of color and anticolor charge (e.g. red–antigreen)

The compact matrix notation is used  $[G^\mu(x)]_{\alpha\beta} \equiv \left(\frac{\lambda^a}{2}\right)_{\alpha\beta} G_a^\mu(x)$ .

To ensure that the covariant derivative  $(D^\mu q_f)$  transforms like the  $q_f$ , the transformation of the gauge fields are:

$$D^\mu \rightarrow (D^\mu)' = UD^\mu U^\dagger \quad G^\mu \rightarrow (G^\mu)' = UG^\mu U^\dagger + \frac{i}{g_s}(\partial_\mu U)U^\dagger \quad (1.29)$$

. The quark and gluon fields transform under an infinitesimal local transformation, i.e.  $\theta_a(x) = \delta\theta_a(x) \approx 0$ , the  $SU(3)_C$  unitary matrices (eq. 1.27) can be expressed as their first order expansion:

$$U = \exp\left\{i\frac{\lambda^a}{2}\theta_a(x)\right\} \approx 1 + i\left(\frac{\lambda^a}{2}\right)\delta\theta_a(x)$$

and, consequently, the transformations for the colour-vector field (eq. 1.26) and gluon field (eq. 1.29) become:

$$\begin{aligned} q_f^\alpha \rightarrow (q_f^\alpha)' &= q_f^\alpha + \left(\frac{\lambda^a}{2}\right)_{\alpha\beta}\delta\theta_a q_f^\beta \\ G_a^\mu \rightarrow (G_a^\mu)' &= G_a^\mu - i\frac{i}{g_s}\partial_\mu(\delta\theta_a) - f^{abc}\delta\theta_b G_c^\mu. \end{aligned}$$

In contrast to the transformation for the photon field in QED (Equation 1.5), the non-commutativity<sup>7</sup> of the  $SU(3)_C$  matrices give rise to an additional term involving the gluon fields themselves ( $-f^{abc}\delta\theta_b G_c^\mu$ ), as the relation 1.28 expresses. For constant  $\delta\theta_a$ , the transformation rule for the gauge fields is expressed in terms of the structure constants  $f^{abc}$ ; thus, the gluon fields belong to the adjoint representation for the colour group. There is a unique coupling at  $SU(3)_C$ ,  $g_s$ . All the colour-triplet flavours couple to the gluon fields with exactly the same interaction strength.

It is necessary to introduce the corresponding fields strengths to build a gauge-invariant kinetic terms for the gluon fields.

$$\begin{aligned} G^{\mu\nu} &\equiv -i\frac{-i}{g_s}[D^\mu, D^\nu] = \partial_\mu G^\nu - \partial_\nu G^\mu + ig_s[G^\mu, G^\nu] \equiv \frac{\lambda^a}{2}G_a^{\mu\nu}(x) \\ G_a^{\mu\nu} &\equiv \partial_\mu G_a^\nu - \partial_\nu G_a^\mu - g_s f^{abc}G_b^\mu G_c^\nu \end{aligned}$$

Under a  $SU(3)_C$  transformation,

$$G^{\mu\nu} \rightarrow (G^{\mu\nu})' = UG^{\mu\nu}U^\dagger \quad (1.30)$$

---

<sup>7</sup>Because the generators of  $SU(3)$  do not commute, QCD is known as non-Abelian gauge theory.

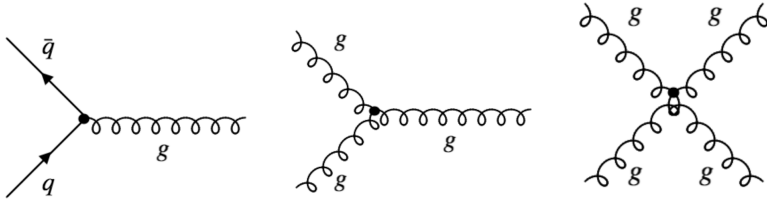


**Figure 1.4:** The predicted QCD interaction vertices arising from the requirement of  $SU(3)_C$  local gauge invariance. The presence of the triples and quadruple gluon vertices is possible to the Non-Abelian nature of  $SU(3)_C$ .

and the colour trace  $\text{Tr}(G^{\mu\nu}G_{\mu\nu}) = \frac{1}{2}G^{\mu\nu}G_{\mu\nu}$  remains invariant. Normalising the gluon kinetic term, the  $SU(3)_C$  invariant QCD Lagrangian is obtained:

$$\mathcal{L}_{QCD} \equiv -\frac{1}{4}G_a^{\mu\nu}G_{\mu\nu}^a + \sum_f \bar{q}_f(i\gamma^\mu D_\mu - m_f)q_f \quad (1.31)$$

Note how the gluon-gluon vertex is found by demanding the gauge invariance under local  $SU(3)_C$  transformation. A mass term is forbidden for the gluon fields by the  $SU(3)_C$  gauge symmetry because something of the form  $\frac{1}{2}m_G^2 G_a^\mu G_\mu^a$  would not be invariant under the transformation in 1.29. The gluons are, then, predicted by the theory to be spin-1 massless particles.

Thanks to the colour symmetry properties, this Lagrangian looks very simple and all its interactions depend on the strong coupling constant,  $g_s$ . In contrast to the Lagrangian derived for QED (eq 1.7), in  $\mathcal{L}_{QCD}$  the boson field have a self-interacting term. This gluon self-interactions give rise to the triple and quadratic gluon vertex (center and right diagrams in Figure 1.4). This self-interactions among the gluon fields can explain features the asymptotic freedom and confinement, properties that were not present in QED. The asymptotic freedom causes interactions between particles to become asymptotically weaker as the energy scale increases and the corresponding length scale decreases. The confinement implies that the strong forces increase with the distance, therefore, as two colour charges are separated, at some point it becomes energetically favorable for a new quark-antiquark pair to appear rather than keep getting further. This new quarks bond with the previous two, preventing single quarks to be isolated. This mechanism, depicted in Figure 1.5, explains why the strong interaction is responsible for keeping the quarks together forming hadrons.

### 1.1.5 Particle masses

For the QED Lagrangian,  $\mathcal{L}_{QED}$  (eq. 1.9), it is clear how the mass of the photon must be zero in order to satisfy the  $U(1)$  local gauge symmetry



**Figure 1.5:** The QCD colour confinement explains the inseparability of quarks inside a hadron in spite of investing ever more energy. In this example, the mechanism is shown for a meson.

because, if a mass term for the vector gauge field  $A_\mu$  is included, the  $\mathcal{L}_{QED}$  would be:

$$\mathcal{L}_{QED} = \bar{\Psi}(x)(i\gamma^\mu \partial_\mu - m)\Psi(x) - eQ\bar{\Psi}(x)\gamma^\mu A_\mu\Psi(x) - \frac{1}{4}F_{\mu\nu}(x)F^{\mu\nu}(x) + \frac{1}{2}m_\gamma^2 A_\mu A^\mu$$

and, with the  $U(1)$  transformation in Equation 1.5, the new mass term becomes:

$$\frac{1}{2}m_\gamma^2 A_\mu A^\mu \rightarrow \frac{1}{2}m_\gamma^2 (A_\mu + \frac{1}{e}\partial_\mu \theta)(A^\mu + \frac{1}{e}\partial^\mu \theta) \neq \frac{1}{2}m_\gamma^2 A_\mu A^\mu$$

Confirming that the photon mass term is not invariant under local  $U(1)$  and, consequently, that the photon must be massless to satisfy the gauge invariance. Experimental efforts to measure the mass of the photon have set an upper limit of  $m_\gamma \leq 1 \times 10^{-18}$  eV [30].

With the Lagrangian of QCD in Equation 1.31 happens the same, the mass term for the gluon fields are forbidden by the  $SU(3)_C$  gauge symmetry. Therefore, the mediating bosons for the strong interactions are massless as well (experimentally, a mass as large as upper limits of a few MeV have been set, see [31]).

While the prohibition of mass terms for the bosons of QED and QCD is not a problem, this requirement also applies to the  $SU(2)_L$ . This condition enters into open contradiction with the measurements of large masses for the  $W$  and  $Z$  bosons of weak interactions.

For weak interactions, the problem of massless particles do not only affect the bosons. Since under the  $SU(2)_L$  transformations left-handed particles transform as weak isospin doubles and right-handed particles as isospin singlets, the mass term of a spinor field  $\Psi$  written as chiral states also breaks the required gauge invariance:  $-m\bar{\Psi}(x)\Psi(x) = -m\bar{\Psi}(x)(P_R + P_L)\Psi(x) = -m(\bar{\Psi}_R(x)\Psi_L(x) + \bar{\Psi}_L(x)\Psi_R(x))$

The Higgs mechanism describes how both the  $W$  and  $Z$  bosons and the fermions acquire mass without breaking the local gauge symmetry of the SM.

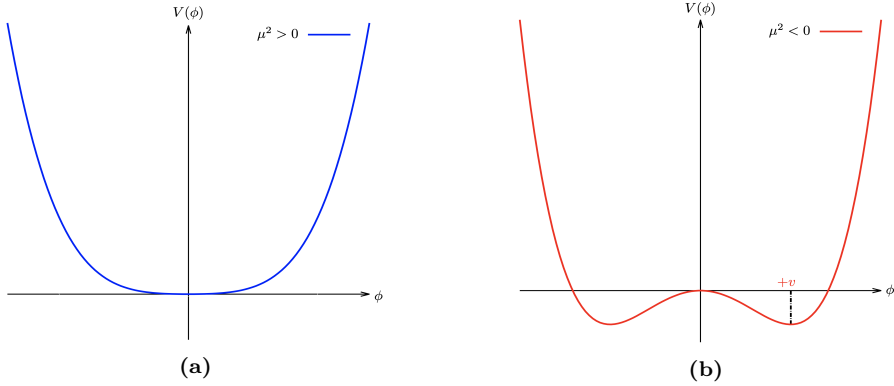


**Figure 1.6:** The potential  $V(\phi)$  of Lagrangian 1.32 for (a)  $\mu^2$  positive and (b) negative.

### 1.1.5.1 The Higgs mechanism

#### Goldstone theorem and spontaneous symmetry breaking

For a scalar field  $\phi$  with a Lagrangian of the form:

$$\mathcal{L} = \frac{1}{2} \partial_\mu \phi_i \partial^\mu \phi_i - V(\phi) \text{ where } V(\phi) = \frac{1}{2} \mu^2 \phi_i \phi_i + \frac{1}{4} \lambda (\phi_i \phi_i)^2 \quad (1.32)$$

This Lagrangian is invariant under  $\phi_i \rightarrow \phi'_i = R_{ij} \phi_j$ , where  $R_{ij}$  are rotational matrices in 4-dimensions. The mass term is the one with  $\phi_i \phi_i$  and the parameter  $\lambda$  has to be positive for  $\mathcal{L}$  to describe a physical system, if  $\lambda < 0$  the potential is unbounded from below. Contrary, the parameter  $\mu^2$  can be either positive or negative. As depicted in Figure 1.6a, if  $\mu^2 > 0$ , the vacuum expectation value (i.e. minimum of potential) is located at the origin  $\phi_0$  and this  $\mathcal{L}$  would describe a spin-0 particle of mass  $\mu$ . However, if  $\mu^2 < 0$ , the potential  $V(\phi)$  has the form of Figure 1.6a and  $\mathcal{L}$  would not represent anymore the Lagrangian of a particle of mass  $\mu$ . The vacuum expectation value is now multivalued:

$$\phi_0 = \pm \sqrt{-\frac{\mu^2}{\lambda}} \equiv \pm v$$

Expanding the field around the minima at  $\phi_i = (0, 0, 0, v)$ , the  $\mathcal{L}$  becomes:

$$\begin{aligned} \mathcal{L} = & \frac{1}{2} \partial_\mu \sigma \partial^\mu \sigma + \mu^2 \sigma^2 - \sqrt{\mu^2 \lambda} \sigma^3 - \frac{1}{4} \lambda^4 \\ & + \frac{1}{2} \partial_\mu \pi_i \partial^\mu \pi_i - \frac{1}{4} \lambda (\pi_i \pi_i)^4 - \lambda v \pi_i \pi_i \sigma - \frac{1}{2} \pi_i \pi_i \sigma^2 \end{aligned} \quad (1.33)$$

where  $i$  runs from 1 to 3. Here  $\sigma = \phi_4 - v$  and  $\pi_i = \phi_i$  are new boson fields, being the latter massless and the former with a mass of  $m_\sigma^2 = -2\mu^2$ . The

new terms break the original symmetry because the symmetry of the Lagrangian is not longer a symmetry of the vacuum, it has been spontaneously broken. One massive  $\sigma$  boson and three massless  $\pi_i$  bosons with a residual  $O(3)$  symmetry have appeared. This is a consequence of the Goldstone theorem which states that “for a continuous symmetry group  $\mathcal{G}$  spontaneously broken down to a subgroup  $\mathcal{H}$ , the number of broken generators is equal to the number of massless scalars that appear in the theory” [32]. Therefore, since the  $O(N)$  group has  $N(N - 1)/2$  generators, the  $O(N - 1)$  has  $(N - 1)(N - 2)/2$  and, hence,  $N - 1$  Goldstone bosons appear. The example shown is for  $N = 4$ .

### The Higgs mechanism in the SM - Bosons

To apply this mechanism to the SM, it is necessary to generate mass for the  $W^+$ ,  $W^-$  and  $Z$  bosons while keeping the photon massless. In order to do so, the EW symmetry group  $SU(2)_L \times U(1)_Y$  has to be broken into a  $U(1)$  subgroup describing electromagnetism. A gauge-invariant interaction that gives masses to fermions without mixing chiral components is introduced by defining a  $SU(2)$  isospin doublet of complex scalar field with hypercharge  $Y = 1$ :

$$\Phi = \begin{pmatrix} \phi^+ \\ \phi_0 \end{pmatrix}$$

Being  $\phi^+$  positively charged and  $\phi^0$  neutral. The Lagrangian  $\mathcal{L}_{Higgs}$  has to be added to the  $\mathcal{L}_{EW}$  in 1.21.

$$\mathcal{L}_{Higgs} = (D_\mu \Phi)^\dagger (D^\mu \Phi) - V(\Phi) \text{ where } V(\Phi) = \mu^2 \Phi^\dagger \Phi + \lambda (\Phi^\dagger \Phi)^2$$

with  $\lambda > 0$  required for vacuum stability. When  $\mu^2 > 0$ , the minimum of the potential occurs when both fields ( $\phi^+$  and  $\phi^0$ ) are at zero. If  $\mu^2 < 0$ , the minimum of the potential has an infinite number of degenerate states that satisfy  $\Phi^\dagger \Phi = \mu^2/2\lambda$  and the physical vacuum state will correspond to any particular point on the circle of Figure 1.7. Having to chose a particular point breaks the global  $U(1)$  symmetry of the Lagrangian. Without loss of generality, in this scenario, the ground state  $\Phi_0$  can be chosen to be:

$$\Phi_0 = \frac{1}{\sqrt{2}} \begin{pmatrix} 0 \\ v \end{pmatrix} \text{ where } v = 2\sqrt{\frac{\mu^2}{\lambda}}$$

being  $v$  the vacuum expectation value. This defines the already mentioned circle in the minimum of  $V(\Phi)$  in the  $\mu^2 < 0$  scenario.

The Lagrangian density must be formulated in terms of deviations from one of these ground states. This can be done by introducing an excitation,  $h(x)$ , that can be understood as a small deviation of the field from the

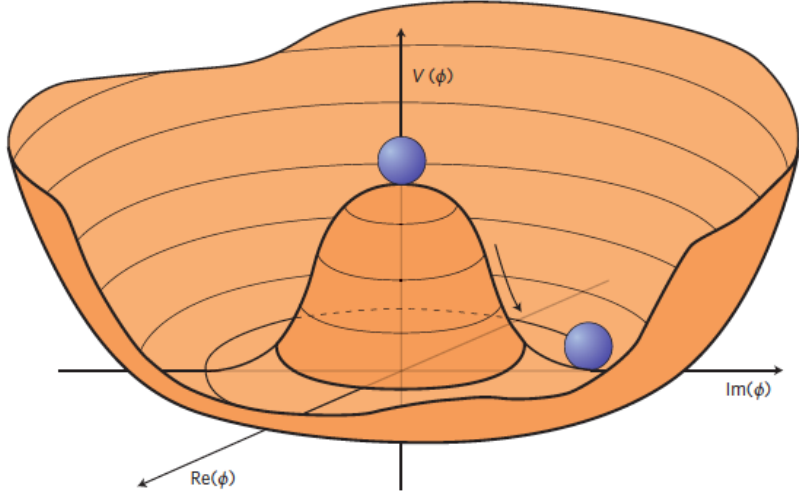


**Figure 1.7:** An illustration of the Higgs potential  $V(\Phi)$  in the case of  $\mu^2 < 0$ . Choosing any particular point in the circle defined by  $v$  spontaneously breaks the  $U(1)$  rotational symmetry. This type of potential is frequently called “Mexican hat”.

ground state. Accordingly, the fields can be expanded around the minimum as:

$$\Phi = \frac{1}{\sqrt{2}} \begin{pmatrix} 0 \\ v + h(x) \end{pmatrix} \exp\{i\chi(x)\}$$

The new field  $\chi(x)$  can be set to zero in the so called “unitary gauge”.

$$\Phi = \frac{1}{\sqrt{2}} \begin{pmatrix} 0 \\ v + h(x) \end{pmatrix} \quad (1.34)$$

Expanding the covariant derivative of the  $\mathcal{L}_{Higgs}$ :

$$\begin{aligned} (D_\mu \Phi)^\dagger (D^\mu \Phi) &= \left| \left( \partial_\mu + ig \frac{\tau^k}{2} W_\mu^k(x) + ig' \frac{y}{2} B_\mu \right) \right|^2 \\ &= \frac{1}{2} \left| \begin{pmatrix} \partial_\mu + i\frac{1}{2}(gW_\mu^3 + g'\frac{y}{2}B_\mu) & i\frac{g}{2}(W_\mu^1 - iW_\mu^2) \\ i\frac{g}{2}(W_\mu^1 - iW_\mu^2) & \partial_\mu - i\frac{1}{2}(gW_\mu^3 - g'\frac{y}{2}B_\mu) \end{pmatrix} \begin{pmatrix} 0 \\ v + h \end{pmatrix} \right|^2 \\ &= \frac{1}{2} (\partial_\mu h)^2 + \frac{1}{8} (v + h)^2 |W_\mu^1 - iW_\mu^2|^2 \\ &\quad + \frac{1}{8} (v + h)^2 |gW_\mu^3 - g'B_\mu| + (\text{interaction terms}) \end{aligned}$$

Where the  $\tau_k$  with  $k = 1, 2, 3$  are the Pauli Matrices. In this equation there are terms mixing the  $W^3$  and the  $B_\mu$  fields that, by using the physical fields defined in Equation 1.1.3.2, should disappear since the physical bosons do not mix. Applying the Relation 1.1.3.2 into the covariant derivative,

$$(D_\mu \Phi)^\dagger (D^\mu \Phi) = \frac{1}{2} + \frac{g^2 v^2}{4} W_\mu^+ W^{-\mu} + \frac{g^2 v^2}{8 \cos^2 \theta_W} Z_\mu Z^\mu + 0 A_\mu A^\mu$$

, the  $W^+$ ,  $W^-$  and  $Z$  bosons have finally acquired mass. Through the Higgs mechanism, their masses within the SM are:

$$M_W = \frac{1}{2}gv \quad M_Z = \frac{1}{2} \frac{gv}{\cos \theta_W}$$

Additionally, a new scalar field  $h(x)$  has appeared with its correspondent mass term, the Higgs field. Note that the  $h(x)$  was introduced as a perturbation from the ground state of the Higgs potential  $V(\Phi)$ , so the Higgs boson can be understood as an excitation of the Higgs potential. Apart from couplings to the electroweak gauge fields, the Higgs field has also self-interaction vertices. The mass of this boson is  $m_H = \sqrt{2}\mu$ .

With this covariant term, the Higgs Lagrangian density of the system is obtained:

$$\begin{aligned} \mathcal{L}_{Higgs} = & \frac{1}{2}(\partial_\mu h)(\partial^\mu h) + \frac{g}{4}(v+h)^4 W_\mu W^\mu + \frac{g^2}{8\cos^2 \theta_W}(v+h)^2 Z_\mu Z^\mu \\ & + \frac{\mu^2}{2}(v+h)^2 - \frac{\lambda}{16}(v+h)^4 \end{aligned}$$

and expressing it in terms of the boson masses and coupling parameters, it can be written as:

$$\begin{aligned} \mathcal{L}_{Higgs} = & \frac{1}{2}(\partial_\mu h)(\partial^\mu h) - \frac{1}{2}m_H^2 h^2 + \frac{1}{2}m_W W_\mu W^\mu + \frac{1}{2}m_Z Z_\mu Z^\mu + g m_W h W_\mu W^\mu \\ & + \frac{g^2}{4} W_\mu W^\mu + g \frac{m_Z}{2\cos \theta_W} h Z_\mu Z^\mu - g^2 \frac{1}{4\cos^2 \theta_W} h^2 Z_\mu Z^\mu - g \frac{m_H^2}{4m_W} h^3 \\ & - g^2 \frac{m_H^2}{32m_W^2} h^4 + \text{const.} \end{aligned} \tag{1.35}$$

As can be seen in the Lagrangian 1.35, the coupling strengths of the  $W$  and  $Z$  fields to the Higgs are proportional to  $m_W$  and  $m_Z$  respectively.

### The Higgs mechanism in the SM - Fermions

The Higgs mechanism for spontaneous symmetry breaking of the  $SU(2)_L \times U(1)_Y$  gauge group of the SM generates the masses of the  $W^\pm$  and  $Z$  bosons. For originating the mass of the fermions without violating the EW gauge symmetry a similar procedure is carried but taking into account that the left-handed particles transform different than the right-handed. To do so, additional terms including the Yukawa couplings are added into the Lagrangian. These terms are of the form:

$$-y_f (\bar{\chi}_L^f \Phi \chi_R^f + \bar{\chi}_R^f \Phi^\dagger \chi_L^f)$$

where the  $f$  superindex runs over all quarks and charged leptons. It is usual to express the second part of the sum just as “plus hermitic conjugate” (“+ h.c.”). Note that the hermitic conjugate part is necessary to ensure that expression fulfils the requirement for a hermitian operator to be self-adjoint in a complex Hilbert space. The different  $y_f$  constants are known as Yukawa couplings of the particle  $f$  to the Higgs field. The Higgs doublet is denoted by  $\Phi$ . For the electron  $SU(2)$  doublet, the element with this coupling can be written as:

$$\mathcal{L}_e = -y_e \left[ (\bar{\nu}_e \bar{e})_L \begin{pmatrix} \phi^+ \\ \phi^0 \end{pmatrix} e_R + \bar{e}_R (\phi^{+*} \phi^{0*}) \begin{pmatrix} \nu_e \\ e \end{pmatrix}_L \right] \quad (1.36)$$

Here,  $y_e$  is the Yukawa coupling of the electron to the Higgs boson. After spontaneously breaking the symmetry as it is done in eq. 1.34, the Lagrangian in 1.36 becomes:

$$\mathcal{L}_e = \frac{-y_e}{\sqrt{2}} v (\bar{e}_L e_R + \bar{e}_R e_L) + \frac{-y_e}{\sqrt{2}} h (\bar{e}_L e_R + \bar{e}_R e_L) \quad (1.37)$$

The  $y_e$  is not predicted by the Higgs mechanism, but can be chosen to be consistent with the observed electron mass ( $m_e$ ) so that  $y_e = \sqrt{2} m_e / v$ . Using this relation, the Lagrangian in 1.37 becomes:

$$\mathcal{L}_e = -m_e \bar{e} e - \frac{m_e}{v} \bar{e} e h \quad (1.38)$$

The first element of the Lagrangian in 1.38 gives mass to the electron and gives rise to the coupling of the electron to the Higgs fields in its non-zero vacuum expectation. The second term represents the coupling of the electron and the Higgs boson itself.

The non-zero vacuum expectation value occurs only in the neutral part of the Higgs doublet (the lower in  $\Phi = \begin{pmatrix} \phi^+ \\ \phi^0 \end{pmatrix}$ ) due to the form in the ground state in 1.34. This implies that the combination  $\bar{\chi}_L^f \Phi \chi_R^f + \bar{\chi}_R^f \Phi^\dagger \chi_L^f$  can only generate masses for the fermions in the lower component of an  $SU(2)$  doublet, i.e. the charged leptons and the down type quarks. Putting aside the procedure to give mass to the up-type quarks, this explains why the neutrinos do not get mass through the Higgs mechanism.

For the up-type quarks, a gauge invariant term can be constructed from  $\bar{\chi}_L^f \Phi_c \chi_R^f + \bar{\chi}_R^f \Phi_c^\dagger \chi_L^f$ :

$$\mathcal{L}_u = y_u (\bar{u} \bar{d})_L \begin{pmatrix} -\phi^{0*} \\ \phi^- \end{pmatrix} u_R + \text{h.c.}$$

Applying the symmetry breaking:

$$\mathcal{L}_u = \frac{-y_u}{\sqrt{2}} v (\bar{u}_L u_R + \bar{u}_R u_L) + \frac{-y_u}{\sqrt{2}} h (\bar{u}_L u_R + \bar{u}_R u_L)$$

with a Yukawa coupling between the up quark and the boson  $y_u = \sqrt{2} m_u/v$ , resulting in:

$$\mathcal{L}_u = -m_u \bar{u} u - \frac{m_u}{v} \bar{u} u h.$$

Therefore, for Dirac fermions, mass terms that let the Lagrangian invariant under local gauge transformations can be constructed from

$$\mathcal{L} = -y_f [\bar{\chi}_L^f \Phi \chi_R^f + (\bar{\chi}_R^f \Phi \chi_L^f)^\dagger] \quad \text{or} \quad \mathcal{L} = y_f [\bar{\chi}_L^f \Phi_c \chi_R^f + (\bar{\chi}_R^f \Phi_c \chi_L^f)^\dagger].$$

The left Lagrangian is used for the leptons and down-type quarks, while the right one is used for the up-type quarks. These elements give rise not only to the mass of the fermions but also to the interaction strengths between these fermions and the Higgs boson. The Yukawa coupling of the fermions to the Higgs field is given by:

$$y_f = \sqrt{2} \frac{m_f}{v} \tag{1.39}$$

where the Higgs vacuum expectation value is fixed by the Fermi coupling  $G_F$  and is measured to be  $v = \sqrt{2} G_F \approx 246.22 \text{ GeV}$ . The  $G_F$  is measured from the  $\mu^+$  lifetime [33]. The  $G_F$  is also used to determine the magnitude of the elements in the CKM matrix.

The value of fermionic masses is not predicted by the SM but obtained through experimental observations. Given the  $m_{top} = 172.76 \pm 0.30 \text{ GeV}$ , it is of particular interest the Yukawa coupling of the top quark to the Higgs field,  $y_t$ , which is almost exactly equal to one. It is important to verify this because deviation of the measured  $y_t$  from the SM prediction would be a proof of new physics.

### 1.1.6 Wrap up

Perhaps the ultimate and definitive (if talking about definitive makes any sense) theory of particle physics is a simple equation with a small number of free parameters. Meanwhile, the SM is here, and while it is not the ultimate theory, it is unquestionably one of modern physics' greatest successes. Despite its achievements, many questions remain unsolved.

#### 1.1.6.1 The parameters of the Standard Model

The SM contains 25 free parameters that must be determined through observation and experimentation. These are the masses of the twelve fermions (assuming color variations and antiparticles are not viewed as separate

fermions) or, more precisely, the twelve Yukawa couplings to the Higgs field ( $m_{\nu_1}, m_{\nu_2}, m_{\nu_3}, m_e, m_\mu, m_\tau, m_u, m_d, m_c, m_s, m_t$  and  $m_b$ ):

The three coupling constants of describing the strength of the gauge interactions ( $g, g'$  and  $g_s$ ). and the two parameters describing the Higgs potential ( $\mu$  and  $\lambda$ ) or, equivalently, its vacuum expectation value  $v$  and the Higgs mass  $m_h$ . The three mixing angles and the complex phase of the CKM matrix and the four of the PMNS matrix ( $\theta_{12}, \theta_{13}, \theta_{23}, \rho_{13}, \theta'_a, \theta'_b, \theta'_c$  and  $\theta'_d$ ), which mixing of neutrino-mass eigenstates with neutrino-flavour eigenstates):

From the 25 free parameters of the SM, 14 are associated to the Higgs field, eight with the flavour sector and only three with the gauge interactions.

### 1.1.6.2 Problems with the Standard Model

While the SM is very good theory that has passed rigorous testing, this is not the ending of the story, there are several limitations of the SM and a variety phenomena that it does not explain. The SM does not cover all questions in the universe and, hence, physicist continue looking for better theories to explain more. There is a long list of small and minor issues with the SM in the following pages only the most relevant ones are described.

#### Gravity

Gravity is the first force that any person learns about and the one known by the humankind for the most time. The SM describes all the other fundamental interactions but this one. In the Table 1.1, the four forces are presented along with the theories to describe them. While QCD, QED and EW interactions are part of the SM, the GR is not. GR is a geometric theory that currently describes the gravitation in modern physics. Some of the suggested solutions to integrate gravitational interactions in the SM consist in postulating a new force carrier particle, the “graviton”, that mediates this interaction in a similar way to how the gauge bosons were proposed. Other explanations state that the gravity can only be described by a deeper theory in which the time-space structure is not flat like it is in the SM but dynamic.

#### Neutrino masses

According to the SM the neutrinos are massless, nevertheless, many experiments confirm that this is not true [34]. This is due to a property of neutrinos that allows them to change their flavour while traveling through

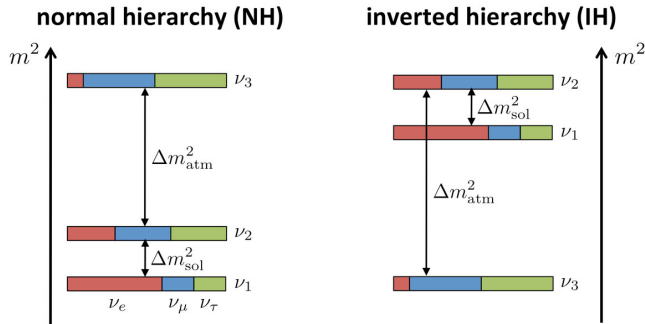


**Figure 1.8:** Two potential mass orderings of neutrinos are the normal ordering (normal hierarchy) and the inverted ordering (inverted hierarchy).

the space, this feature is known as “neutrino oscillations”. Each of the three neutrino flavours ( $\nu_e$ ,  $\nu_\mu$ ,  $\nu_\tau$ ) is a linear combination of three discrete neutrino-mass eigenstates ( $\nu_i$  with  $i \in \{1, 2, 3\}$ ) with mass eigenvalues ( $m_i$ ). While the neutrino oscillation experiments could probe the squared neutrino-mass eigenvalues ( $\Delta m_{ij}^2$ ), both the total scale of the masses and the sign of  $\Delta m_{ij}$  remains as some the most relevant open questions in particle physics. Regarding to the sign of  $\Delta m_{ij}$ , it is known that the mass of  $\nu_2$  is slightly higher than  $\nu_1$  ( $\Delta m_{21}^2 \equiv m_2^2 - m_1^2 \sim 10^{-4}$  eV) but for the third mass eigenstate it has not been measured yet whether it is greater (normal ordering) or lower (inverted ordering) than the other two, as it is depicted in Figure 1.8. Nevertheless, the absolute square difference is known ( $\Delta m_{31}^2 \equiv |m_3^2 - m_1^2| \sim 10^{-3}$  eV).

Non-zero neutrino masses opened an interesting portal on beyond SM physics and, even though neutrinos are very elusive when it comes to detect them, some next-generation experiments such as Dune are very promising when it comes to set competitive and model independent limits on neutrino masses.

Regarding to the nature of this mass, one could add mass terms to the SM as it is done in Section 1.1.5.1 for the up-type quarks but the origin of the neutrino masses is still not known. Also, if neutrinos gained mass through Yukawa interaction, it would imply the presence of right-handed neutrinos, which has not been observed.

### Matter-antimatter asymmetry

In principle, the Big Bang should have produced an equal amount of matter and antimatter which would all have then annihilated, leaving behind an empty Universe filled with EM radiation. However, everything we see now is essentially totally constituted of matter, from the tiniest life forms on

Earth to the greatest celestial objects. In comparison, there isn't a lot of antimatter around.

By looking at the CMB radiation, which contain the residual photons of the Big Bang, researchers have determined that there was a symmetry between the matter and antimatter content in the early universe. For every  $3 \times 10^9$  antimatter particles, there were  $3 \times 10^9$  and 1 matter particles. The matter and antimatter annihilate and produced the CMB and the remaining 1 part turned into all the stars and galaxies that are seen. The field of cosmology that studies the processes that produced an asymmetry between leptons and antileptons in the very early universe is called leptogenesis.

Researches carried during the last few decades have revealed that the laws of nature do not equally apply to matter and antimatter. So far, the only non-trivial difference between matter and antimatter found is the  $\mathcal{CP}$  asymmetry (or  $\mathcal{CP}$  violation, which has been introduced in Section 1.1.3). Alas, the quantity of  $\mathcal{CP}$  asymmetry included in the SM is insufficient to explain the composition of the observable universe and, hence, extensive searches of new sources of  $\mathcal{CP}$  violation are being carried.

In this context, the studies described in this thesis are part of the seek of new  $\mathcal{CP}$ -violation sources. As Section 2.3.2 details, the observation of a cross-section greater than the one predicted by the SM would imply that Higgs-single-top-quark associated production does not conserve  $\mathcal{CP}$ .

## **Dark energy**

According to cosmological observations, the matter described by the SM only makes up around 5% of the universe. It turns out that roughly 68% of the universe is dark energy, which is not considered by the SM.

Dark energy is an unknown type of energy postulated to explain the observed accelerated expansion of the universe as Figure 1.9. This expansion is dominated by a spatially smooth component with negative pressure called dark energy. Modern cosmological measurements are based in supernovae, cosmic microwave background fluctuations, galaxy clustering and weak gravitational lensing, and methods agree with a spatially flat universe with about 30% matter (visible and dark) and 70% dark energy [35].

## **Dark matter**

The rest of the energy content in the universe is the matter. Dark matter (DM) adds up for approximately 85% of all matter and 27% of all energy. This matter is called dark because it does not interact with the electromagnetic field, so maybe a name such us invisible matter would have been more appropriate since rather than being dark it just does not emit or reflect

light. The only way to interact with DM is via gravitational interaction, which is about 25 orders of magnitude weaker than the weak force (as Table 1.1 shows). This is why DM is so difficult to detect. The SM does not provide a proper explanation but searches are being carried and candidates such as weakly interacting massive particles (WIMPs) or axions<sup>8</sup> have been proposed.

The existence of DM has been inferred through gravitational effects in astrophysical and cosmological observations. The rotational speed of the galaxies [38], the gravitational lensing [39] and the CMB angular spectrum [40] are some examples of phenomena that cannot be explained with general relativity unless there is more present matter than what is seen.

Although the vast majority of scientific community accepts dark matter existence, alternative explanations for the observed phenomena have suggested. Most of these models consist in modifications of GR. The search of DM at particle colliders, which is focused on large missing transverse energy signatures, have not resulted in any observation. Nevertheless, the existence of a particle is never discarded, only its presence within the detector sensitivity limits.

## Others

(quizás, esto es lo "others" sobra ya) The different problems mentioned hitherto are just some of the most relevant open questions that fundamental physics has not been able to answer yet. Nonetheless, there are many other issues whose discussion would need many pages and are outside the scope of this work. Even so, it won't harm to list a few of them:

- Hierarchy problem: It is caused by the enormous distance between two fundamental physics scales: the EW scale ( $\sim 10^2$  GeV) and the Planck scale ( $\sim 10^{19}$  GeV).

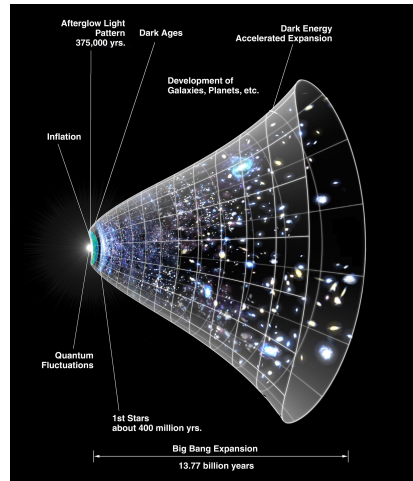


**Figure 1.9:** The universe's expansion over time. The dark-energy existence has been suggested to explain this expansion.

<sup>8</sup>An axion is a hypothetical elementary particle postulated to resolve the strong CP problem [36] [37].

- Strong  $\mathcal{CP}$  problem: It refers to the fact that, while QCD does not explicitly prohibit  $\mathcal{CP}$  violation in strong interactions, it has yet to be observed in experiments.
- Naturalness: It is the property that the dimensionless ratios between free parameters or physical constants appearing in a physical theory should take values of order unity. By looking at the parameters of the SM described in Section 1.1.6.1, it can be seen that the naturalness principle is not satisfied. For instance, the masses of the first generation of fermions are in the range of 1 MeV while the top quark has a mass of 172-173 GeV. Though this is not a flaw in the theory itself, it is frequently seen as a sign of undiscovered principles hidden behind a more comprehensive theory.
- Composite Higgs models:
- Majorana neutrinos: It is not clear yet if neutrinos are Majorana particles, i.e. they are their own antiparticles ( $\nu = \bar{\nu} = \nu_M$ ). Current experiments trying to solve this question are focused on neutrino-less double- $\beta$  decay, which can occur only if neutrinos are Majorana particles.

Most of theoretical concepts of the SM were in place by the end of the 1960s. With the discovery of the  $W$  [41] and  $Z$  [42] bosons at CERN in the mid 1980s and the Higgs boson in 2012, the SM has established itself as one of the major pillars of modern physics. The understanding of the universe at the most fundamental level is based in this theory, which has been tried to be summarised through the entire Section 1.1.

Despite its brilliance and success, the SM is not the ending of the story. As exposed above, there are far too many unanswered questions and loose ends. The HL-LHC [43] and the next generation of experiments will look for evidence of physics outside the SM in the next years.

Among the open questions, unresolved concerns and measurements to be completed, this research is focused on the top quark<sup>9</sup>. On one hand, contributions to the measurement of the polarisation of this quark are presented and, on the other hand, the study of the associated production of a single-top quark with a Higgs boson is present as well. Now that the basics of the SM have been settled, in the sections to come, the context of these two topics is being discussed.

---

<sup>9</sup>Here and in the following, the usage of the term top quark includes the top antiquark.

# Chapter 2

## Top quark and Higgs boson physics

### 2.1 Top quark

The top quark ( $t$ ) or, for simplicity, just top is the up-type quark of the third generation of fermions. Its most distinctive feature is its huge mass, which is the largest among all fundamental particle particles. The left-handed top is the  $Q = 2/3$  and  $T_3 = +1/2$  member of the weak isospin doublet that also contains the bottom quark. The right-handed top quark is the  $SU(2)_L$  weak isospin singlet ( $Q = 2/3$  and  $T_3 = 0$ ). Its phenomenology is driven by its large mass. The top quark is often regarded as a window for new physics since it provides a unique laboratory where to test the understanding of the SM.

Due to being so massive, its life time is very short ( $\tau_t = 5 \times 10^{-25}$  s [39]). Actually, it is shorter than the hadronisation time ([cite](#)), this represents a unique opportunity to study quarks in free state, something that is very rare due to colour confinement, as explained in Section 1.1.4. In fact, the top quark is the only quark that can be investigated in unbounded. Some of its properties, such as the spin information, can be accessed through its decay products and, consequently, be measured.

Another consequence of its large mass is that the top quark is the only quark with a Yukawa coupling ( $y_t$ ) to the Higgs boson of the order of one; hence, a thorough understanding of its properties (mass, couplings, decay branching ratios, production cross section, etc.) can reveal crucial information on basic interactions at the electroweak symmetry-breaking scale and beyond. The main objective of this thesis is, precisely, the study of the top quark and Higgs boson interplay to, ultimately, help to determine it the

$y_t$  is that predicted by the SM or there is some  $\mathcal{CP}$ -violating phase that would affect the sign of the Higgs-top Yukawa coupling. The theoretical base for the understanding the associated production of a top quark and a Higgs boson given in Section 2.3 and the analysis investigating this matter is presented in Chapter 6.

### 2.1.1 Top-quark discovery

In 1973, Kobayashi and Maskawa postulated the possibility of a third generation of quarks to explain  $\mathcal{CP}$  violations in kaon decays [44]. To match the names of the up and down quarks, the new generation's quarks were given the names top and bottom. The GIM mechanism, which predicted the existence of the yet-to-be-discovered charm quark, was used to make this prediction. When the charm was observed [45], the GIM was integrated into the SM and the postulation of the third family, and thus the top quark, gained acceptance. Shortly after the charm, the bottom quark was discovered in the E288 experiment at Fermilab [46], reinforcing the idea of the existence of the top quark. However, due to its large mass, it took 18 years to confirm the existence of the top.

The top quark was observed for the first time at Tevatron with the CDF [47] and D $\emptyset$  [48] detectors via flavour-conservating strong interaction in 1995. Back then and until the start of LHC Run-1, Tevatron was the only accelerator powerful enough to produce top quarks.

#### Top quark mass

-> Latest results (june 2022) <https://cds.cern.ch/record/2811385> [49]

-> Top quark mass defines the stability of the EW vacuum. It is a key factor to test the internal consistency of the SM.

As discussed in Section 1.1.6.1,  $m_{top}$  is a free parameter of the SM. The theory does not predict its value, hence it must be determined experimentally. To derive the  $m_{top}$  from hadron collision data, two approaches are explored:

- Direct measurements (also known as template methods) [50]: The  $m_{top}$  is determined by reconstructing (fully or partially) the decay products of one or more top quarks in a  $t\bar{t}$  or single-top event<sup>1</sup>. A comparison of the detector-level distribution with templates created

---

<sup>1</sup>In particle physics, an event is the result of a collision, as recorded by the experiment.

with a MC generator is used to determine the mass. Analysing  $t\bar{t}$  events with lepton-plus-jets and dilepton topologies provides the most precise results.

- Indirect measurements[50]: Performed from measurements of cross-section. These methods rely on the dependence on the value of the  $m_{top}$  for the total or differential production cross sections for processes involving top quarks.

Among the top quark's properties, its mass is the one that has received the most attention so far. The most recent studies for the top quark mass measurements result in  $m_{top} = 172.76 \pm 0.30$  GeV [51]. This number is an average of the measurements at LHC with ATLAS ( $172.69 \pm 66$  GeV [52]) and CMS ( $172.6 \pm 3.5$  GeV at CMS [53]) and at Tevatron with CDF and D $\emptyset$  (combined result:  $174.30 \pm 0.89$  GeV [54]). These values are measured from the kinematics of  $t\bar{t}$  events<sup>2</sup>.

Figure 2.1 summarises the measurements of ATLAS and CMS for  $m_{top}$  from direct-top-quark decay.

### 2.1.2 Top quark production at LHC

The LHC is sometimes referred as a top quark factory due to its ability to produce such particles. In this collider, at  $pp$  collisions, the top quark is mainly produced via two mechanisms: through QCD in top and anti-top pairs ( $t\bar{t}$ ), and by means of the  $Wtb$  vertex of EW in single-top quarks associated with other particles. Apart from the  $t\bar{t}$  (Section 2.1.2.1) and single-top (Section 2.1.2.2) productions, the associated  $t\bar{t} + X$  and four-top-quark productions (Sections 2.1.2.3 and 2.1.2.4 respectively) are presented as well.

Since the top quarks often constitute a main background in other physics analysis, a better understanding of this particle's properties will directly translate into improvements in those searches.

#### 2.1.2.1 Top pairs

The production top and anti-top pair of quarks is the largest source of production of top quarks in hadron collisions. This process is one of the most important at LHC because it allows to precisely study the properties

---

<sup>2</sup>This  $m_{top}$  results are sensitive to the top quark mass used in the MC generator that is usually interpreted as the pole mass.

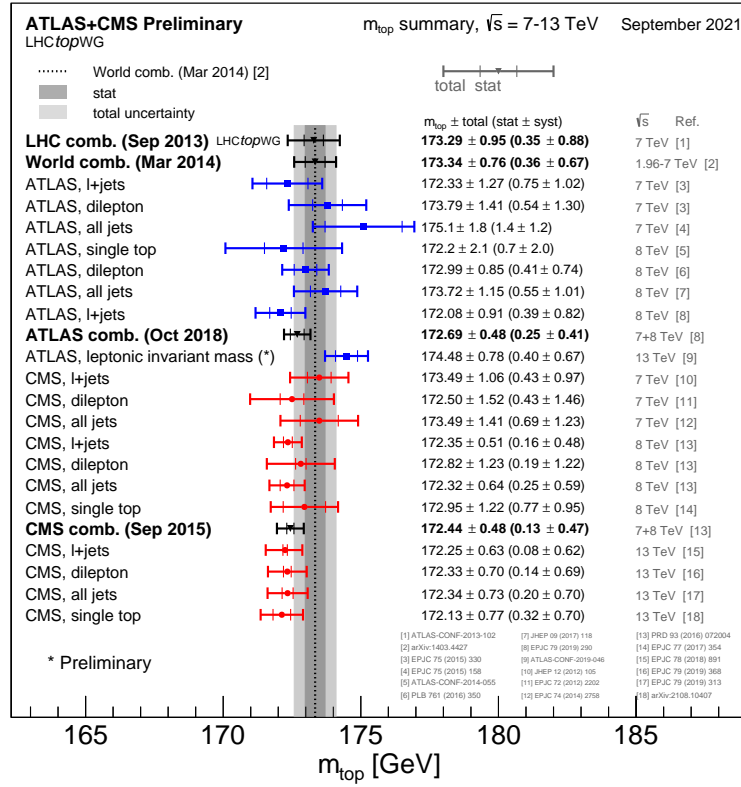


**Figure 2.1:** Summary of the ATLAS and CMS measurements from top-quark decay. Results compared to LHC  $m_{top}$  combination [49]. **Can be updated with the June 2022 plot (+ Ref). Maybe there will be even a new one after TOP2022.**

of the top quark. Additionally, due to the dominance of this production mode, the top-quark-pair production is also a major background in many searches for rare processes. Including the one carried in this thesis, where  $t\bar{t}$  is the main background in the both of the analysed decay channels (see Section 6.5).

For the  $p\bar{p}$  collisions at Tevatron or  $pp$  at LHC, the  $t\bar{t}$  production is described by perturbative QCD. In this approach, a hard scattering process between the two hadrons is the result of an interaction between the quarks and gluons that constitute these hadrons. This model is described with detail in Section 3.2.7.

At LHC, the gluon fusion (Figure 2.2) dominates with a 90% of the  $t\bar{t}$  production. It is followed by the quark and antiquark annihilation (Figure 2.3), which accounts for a 10% of the the total top-quark-pair production. The theoretical calculations for the  $t\bar{t}$  production are done to an accuracy of next-to-next-to-leading order (NNLO) in QCD [55] and measured by ATLAS and CMS. Figure 2.4 shows the measurements for the  $t\bar{t}$  pro-

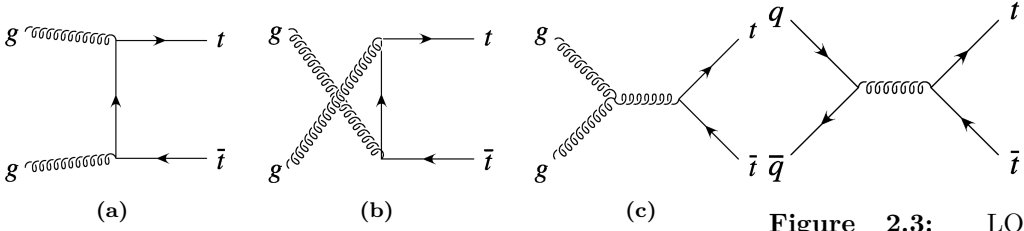


**Figure 2.2:** Representative Feynman diagrams of the LO processes contributing to the  $t\bar{t}$  production through gluon fusion at LHC.

**Figure 2.3:** LO Feynman diagram for  $t\bar{t}$  production via quark and anti-quark annihilation.

duction cross section ( $\sigma_{t\bar{t}}$ ) at a center-of-mass energy ( $\sqrt{s}$ ) of 13 TeV. The measurements and the theory calculations are quoted at  $m_{top} = 172.5$  GeV.

### 2.1.2.2 Single top

In addition to the top-quark-antiquark-pair production, the single-top-quark processes are of great importance to the study of the top quark properties at the LHC. This mechanism has a cross section three times smaller than that of  $t\bar{t}$  and are almost exclusively produced through the EW  $Wtb$  vertex. This is precisely the reason why single-top-quark production is essential to gather information the  $Wtb$  interaction and to directly measure  $|V_{tb}|$  at hadron colliders. The reason to both decay to a  $b$ -quark and be produced from a  $b$ -quark and not from strange or down quarks is because the CKM elements  $V_{ts}$  and  $V_{td}$  are much more smaller than  $V_{tb}$  by several orders of magnitude as Table 1.3 shows.

At LO, there are three production modes for single top, being the  $t$ -channel the dominant mechanism at the LHC with, approximately 70% of the single top quark cross section at a  $\sqrt{s} = 13$  TeV. The other processes are the  $s$ -channel and the associated production  $tW$  production. Only  $t$ -channel and  $tW$  productions are relevant to the EW single-top production at LHC.

#### **$t$ -channel**

This production mode involves the scattering of a light quark and a gluon from the proton sea as shown in Figure 2.5. Note that additional diagrams to those in Figure 2.5 are obtained by either replacing the  $u$  and  $d$  by a  $c$  and  $s$  quarks or by switching the light quarks in the fermion line. The diagrams for antitop production are the charge conjugate of the ones presented.

The measurements cross sections at 13 TeV for single-top ( $\sigma_{t-channel,t}$ ) and single-anti-top ( $\sigma_{t-channel,\bar{t}}$ ) quarks in the  $t$ -channel production are

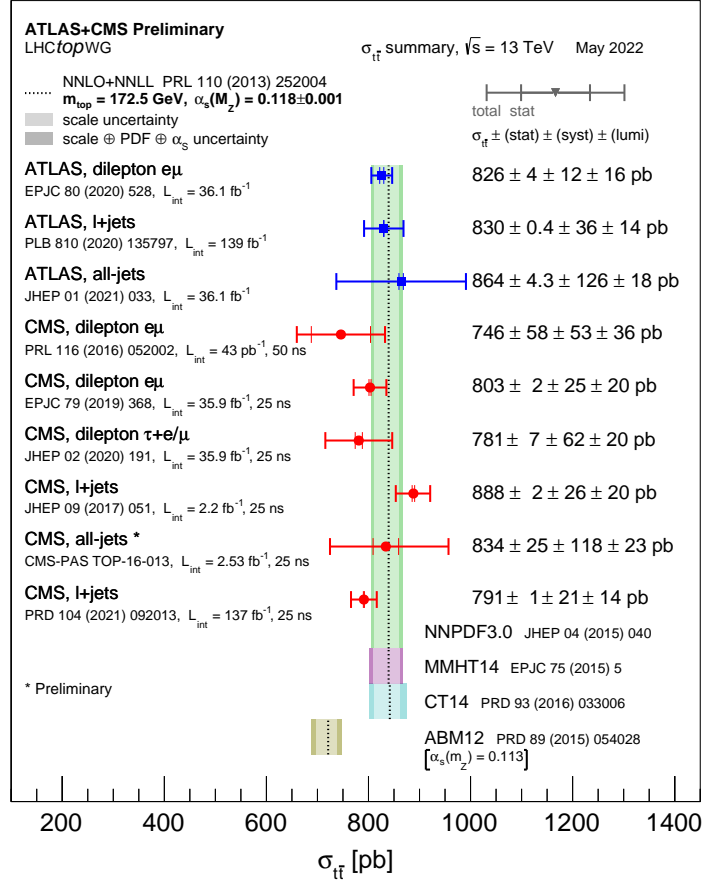


**Figure 2.4:** Summary of measurements  $\sigma_{t\bar{t}}$  at 13 TeV compared to the exact NNLO QCD calculation complemented with NNLL resummation.

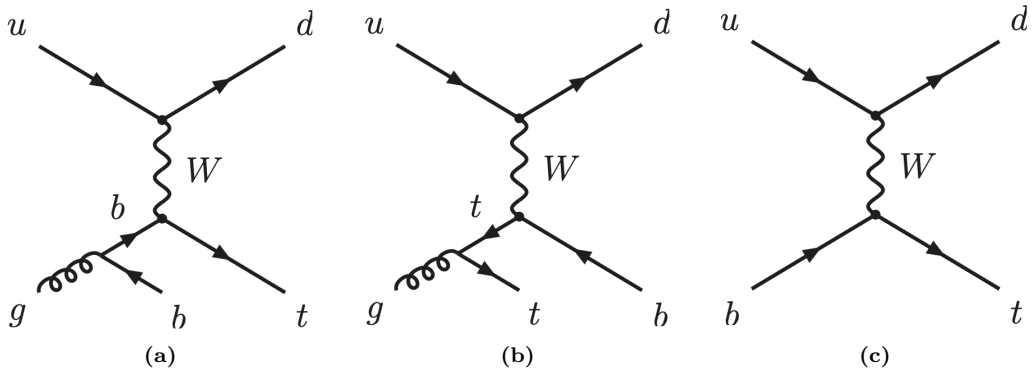


**Figure 2.5:** Representative Feynman diagrams for the single-top-quark production in the  $t$ -channel process.

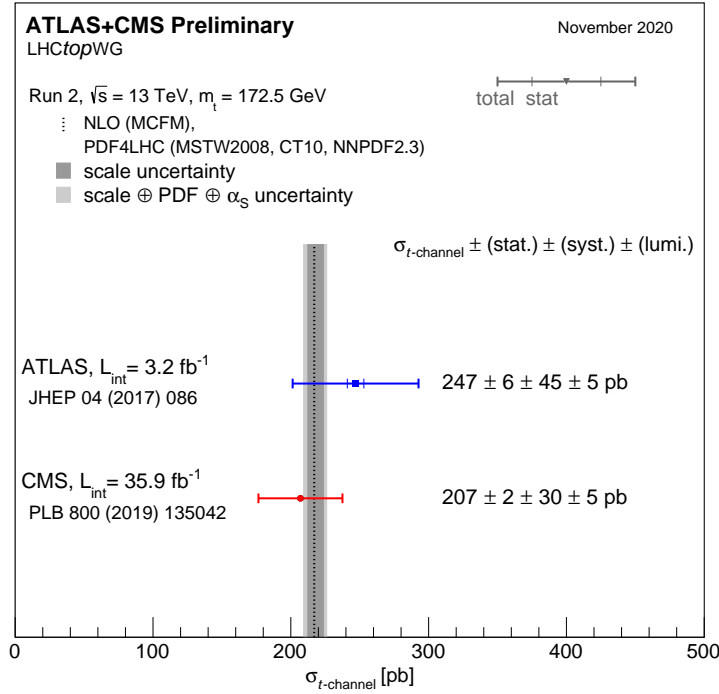


**Figure 2.6:** Summary of the ATLAS and CMS measurements of the single top production cross-sections in the  $t$ -channel at 13 TeV.

shown in Figure 2.6. The theoretical calculations at NLO for  $\sigma_{t\text{-channel}, t+t\bar{t}}$  at 13 TeV are:

$$\begin{aligned}\sigma_{t\text{-channel}, t} &= 136^{+4.1}_{-2.9}(\text{scale}) \pm 3.5(\text{PDF} + \alpha_s) \text{ pb}, \\ \sigma_{t\text{-channel}, t\bar{t}} &= 81.0^{+2.5}_{-1.7}(\text{scale}) \pm 3.2(\text{PDF} + \alpha_s) \text{ pb}, \\ \sigma_{t\text{-channel}, t+t\bar{t}} &= 217^{+6.6}_{-4.6}(\text{scale}) \pm 6.5(\text{PDF} + \alpha_s) \text{ pb}.\end{aligned}$$

These numbers have been obtained using HATHOR 2.1 [56][57].

The dominant process in the SM is the one in diagram 2.5a, while the one in 2.5b is included in order to form a gauge invariant set but its contribution is not very significative since for the gluon is easier to decay to  $b\bar{b}$  pair than to a  $t\bar{t}$  pair. These two  $3 \rightarrow 2$  production modes are known as 4 Flavour Scheme (FS) because the proton is considered to be composed by five quark flavours ( $u, d, c$  and  $s$ ) and is characterised by having a  $b$  quark in the final state. This final state  $b$  quark is sometimes referred as second  $b$  and it has a transverse momentum ( $p_T$ ) distribution peaking around 2 or 3 GeV as can be seen in Figure 2.7. This is the reason why the final  $b$  quark from the gluon splitting frequently goes undetected, because it does not pass the  $p_T$  threshold of the detector. This is why, at detector level, whenever only jet is identified as originated from a  $b$  quark, it is assumed to be the  $b$  from the

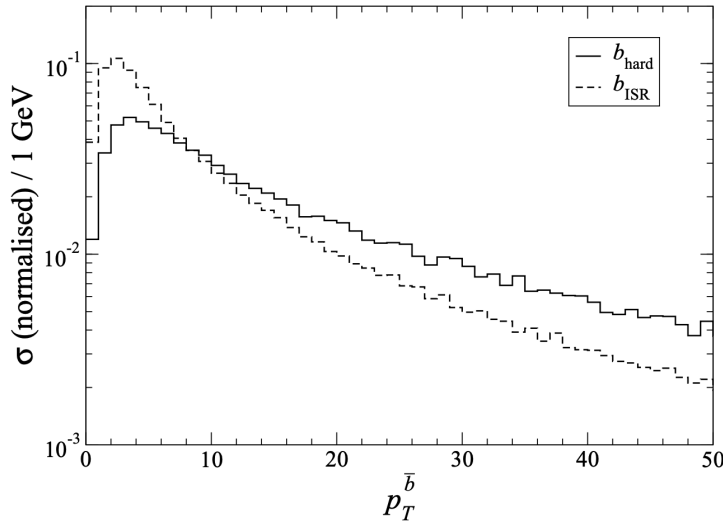


**Figure 2.7:** Normalised  $p_T$  distribution of the second  $b$  quark in the  $t$ -channel process, generated by Monte Carlo (MC) simulation [58].

the top-quark decay. This particularity becomes more important in Chapter 6.

The  $2 \rightarrow 2$  process in 2.5c is known as 5FS because the proton is considered to be composed by five flavours of quarks ( $u, d, c$  and  $s$ ) and it is characterised by having a  $b$  quark in the initial state. The simulations for the 4FS and 5FS diagrams are produced separately and merged afterwards. When adding the two contributions, some double-counting may appear due to the overlap in the phase space so one has to be careful. The naming 4FS and 5FS is later used again for the associated  $tHq$  production.

### s-channel

The  $s$ -channel process for single-top is the one with less impact among single-top production channels. It is depicted in Figure 2.8. This production mode is also referred as the quark-antiquark annihilation or  $W^*$  process and it is very similar to the Drell-Yann.

According to the LHC cross section group, at 13 TeV of center-of-mass energy, the cross sections for the single top and single anti-top production in the  $s$ -channel ( $\sigma_{s\text{-channel}}$ ) are:

$$\begin{aligned}\sigma_{s\text{-channel},t} &= 6.35^{+0.18}_{-0.15}(\text{scale}) \pm 0.9(\text{PDF} + \alpha_s) \text{ pb}, \\ \sigma_{s\text{-channel},\bar{t}} &= 3.97^{+0.11}_{-0.09}(\text{scale}) \pm 0.15(\text{PDF} + \alpha_s) \text{ pb}, \\ \sigma_{s\text{-channel},t+\bar{t}} &= 10.32^{+0.29}_{-0.34}(\text{scale}) \pm 0.27(\text{PDF} + \alpha_s) \text{ pb}.\end{aligned}$$

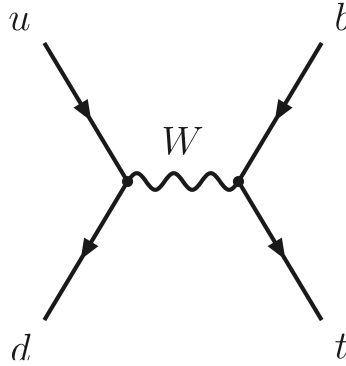


**Figure 2.8:** Representative Feynman diagram for the single-top-quark production in the  $s$ -channel.

Note that while at LHC the  $s$ -channel production has not been observed at LHC, for Tevatron it was a significant part of the total single-top cross-section.

### Associated $tW$

Finally, the associated production of a single top quark with a  $W$  boson (sometimes referred as  $tW$ -channel) is represented by two the Feynman diagrams in Figure 2.10. To these two diagrams, the charge conjugate processes could be added to complete the  $tW$  mechanisms. The predicted cross section for the associated  $tW$  is:

$$\sigma_{tW,t+\bar{t}} = 71.7 \pm 1.80(\text{scale}) \pm 3.40(\text{PDF} + \alpha_s) \text{ pb.}$$

This and all  $\sigma$  in the section are calculated for a top mass of  $m_{top} = 172.5 \text{ GeV}$  and NLO in QCD with HATHOR v.2.1. The PDF and  $\alpha_s$  uncertainties are calculated using the PDF4LHC prescription [59] with the MSTW2008 68% CL NLO [60][61], CT10 NLO [62] and NNPDF2.3 [63] PDF sets, added in quadrature to the scale uncertainty.

#### 2.1.2.3 Associated $t\bar{t} + X$ production

#### 2.1.2.4 Four tops

Figure 2.14

### 2.1.3 Top-quark decay

As advanced in the Section 2.1.2.2, due to the large  $V_{tb}$  element of the CKM matrix, the top quark decays almost entirely ( $\sim 99.8\%$ ) thorough the

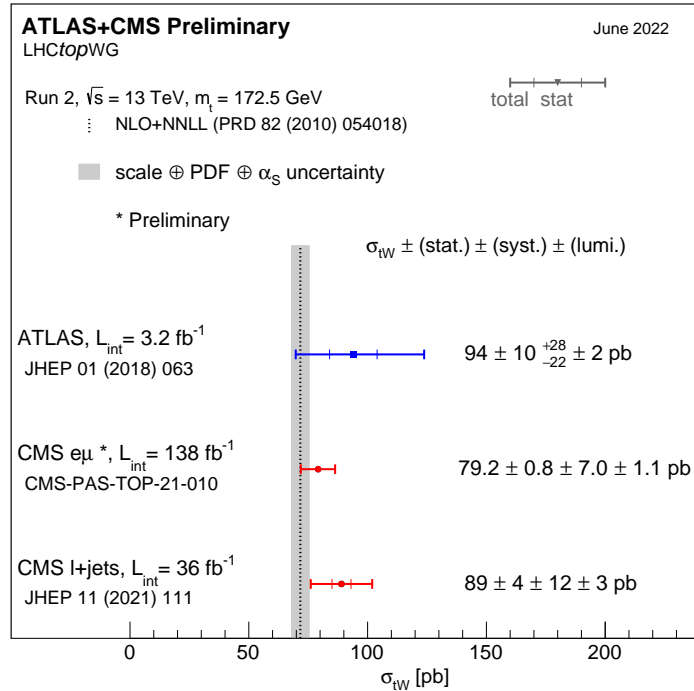


**Figure 2.9:** Cross-section measurements for the associated  $tW$  production boson performed by ATLAS and CMS at 13 TeV, and combined result compared with the NLO+NNLL prediction.

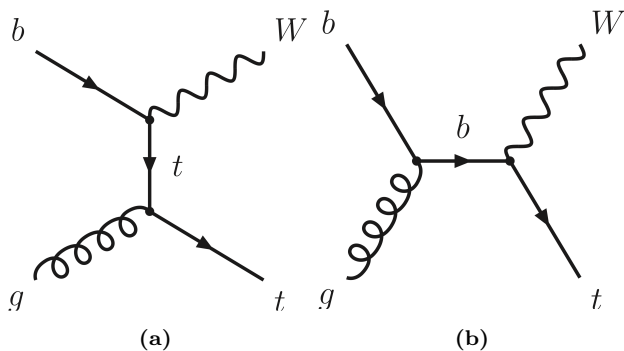


**Figure 2.10:** Representative Feynman diagrams for the single-top-quark production in association with a  $W$  boson.

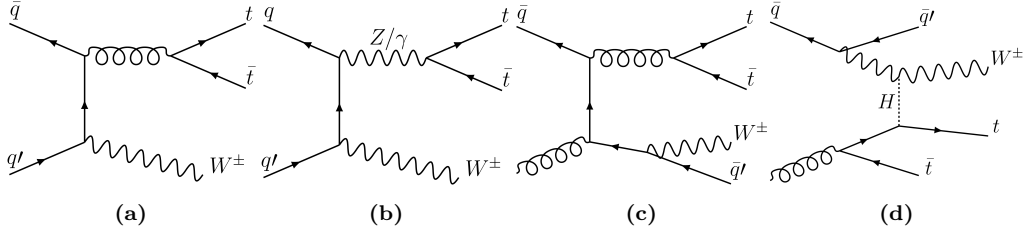


**Figure 2.11:** Representative Feynman diagrams for  $t\bar{t}W$  production. Left diagrams show the  $\bar{q}q' \rightarrow t\bar{t}W$  processes and right ones the  $\bar{q}g \rightarrow t\bar{t}Wq'$  production.

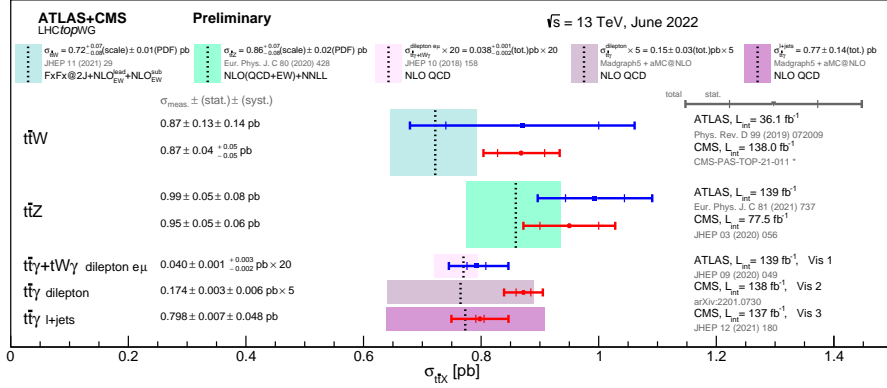


**Figure 2.12:** Summary of the ATLAS and CMS measurements of the  $t\bar{t} + X$  production cross-sections at 13 TeV. Here  $X = W, Z$  and  $\gamma$ .

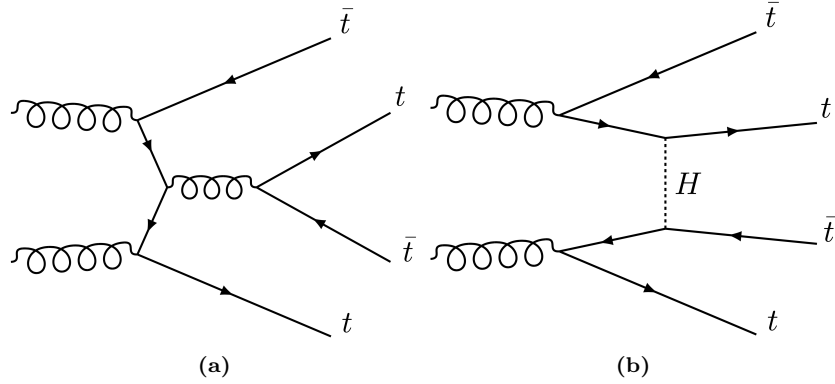


**Figure 2.13:** Representative Feynman diagrams for the  $gg \rightarrow t\bar{t}t\bar{t}$  production.

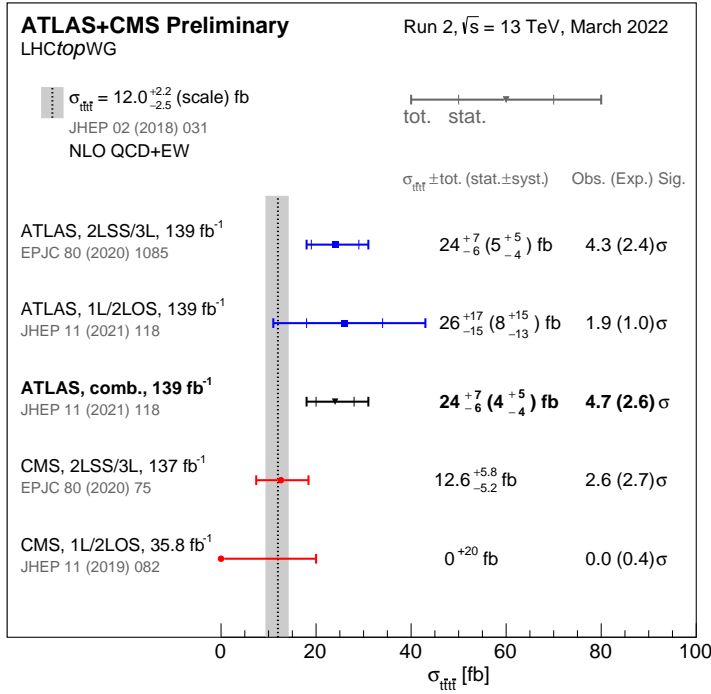


**Figure 2.14:** Summary of the ATLAS and CMS measurements of the  $t\bar{t}t\bar{t}$  production cross-sections at 13 TeV in various channels

medium of the  $Wtb$  vertex to a  $b$  quark and a  $W$  boson. The final state decay is classified according to the subsequent decay of the  $W$  boson. As  $W$  are massive vector bosons, its lifetime is very short ( $\tau_W \approx 3 \times 10^{-25}$  s). For the  $W^+$ , the decay modes are:

$$\begin{aligned}
 W^+ &\rightarrow e^+ \nu_e & (10.71 \pm 0.16)\% \\
 W^+ &\rightarrow \mu^+ \nu_\mu & (10.63 \pm 0.15)\% \\
 W^+ &\rightarrow \tau^+ \nu_\tau & (11.38 \pm 0.21)\% \\
 W^+ &\rightarrow q\bar{q} \text{ (hadrons)} & (67.41 \pm 0.27)\% \\
 W^+ &\rightarrow \text{invisible} & (1.4 \pm 2.9)\%
 \end{aligned}$$

For the conjugate processes involving the  $W^-$ , the branching ratios (BR) are the same. Therefore, the  $W$  decay and consequently the  $t$  decay can be classified either as leptonic or hadronic. The decay chain of the top quark is represented in Figure 2.15. Due to its large mass, the  $W$  can decay to any quark except the top quark. For a certain decay mode, the BR is defined as the fraction times that the particle decays in that particular mode with respect to total possible decays.

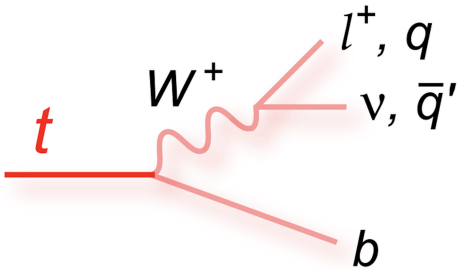


**Figure 2.15:** Decay of a top quark to a  $b$  quark and a  $W$  boson. The  $W$  boson can decay either leptonically to a neutrino and a lepton or hadronically to a pair of light-flavour quarks. In the hadronic  $W$  decay, a jet triplet is formed along with the  $b$  quark.

## 2.2 Higgs boson

Following the top quark, the Englert-Brout-Higgs-Guralnik-Hagen-Kibble-Higgs boson or, for simplicity, Higgs boson ( $H$ ) or just Higgs is the most massive particle in the SM with a mass of  $m_H = 125.25 \pm 0.17$  GeV [64]. The value provided by [64] is an average of the ATLAS combined measurement ( $m_H = 124.86 \pm 0.27$  GeV [65]) and the CMS results ( $m_H = 125.46 \pm 0.16$  [66]).

The Higgs boson existence was theorised in 1964 by three independent groups: Englert-Brout [67], Higgs [68] and Guralnik-Hagen-Kibble [69], and its discovery meant one of the greatest successes of the SM. This theory was not only able to calculate with great precision the physics but also predicted the existence of a particle that was found later (see 2.2.1).

### 2.2.1 Higgs-boson discovery

Any particle physicist enthusiast remembers July 4th of 2012 pretty well, it was LHC experiments ATLAS [1] and CMS [2] who announced the discovery of a massive state  $H$  with the properties expected for the Higgs boson.

Both the ATLAS and CMS Collaborations reported excesses of events for 2011 ( $\sqrt{s} = 7$  TeV and  $\mathcal{L} = 4.8 \text{ fb}^{-1}$ ) and 2012 ( $\sqrt{s} = 8$  TeV and  $\mathcal{L} = 458 \text{ fb}^{-1}$ ) datasets of proton-proton ( $pp$ ) collisions. This surplus of events was compatible in its production and decay with the SM Higgs boson in the mass region  $m_H \in [124, 135] \text{ GeV}$  with significances of  $2.9\sigma$  for ATLAS and  $3.1\sigma$  for CMS. At Tevatron (circular proton-antiproton collider at Fermilab), the experiments CDF [70] and D $\emptyset$  [71] also reported an excess in the mass region  $m_H \in [120, 135] \text{ GeV}$ .

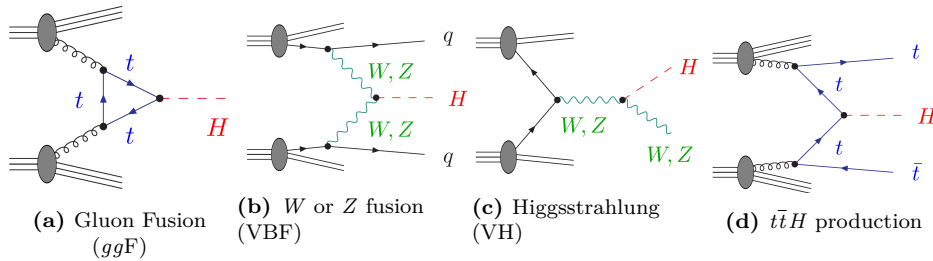


**Figure 2.16:** Lowest-order Feynman diagrams for the dominant production mechanisms of a Higgs boson at hadron colliders.

## 2.2.2 Higgs boson production at LHC

One of the reasons why the Higgs boson was found the latest among SM fundamental particles is because it is a fairly heavy particle and, hence, it was necessary a lot of energy to produce it. Even though that colliders such us SLAC or LEP had enough energy, they were colliding electrons and positrons and, since the coupling of the Higgs to fermions is proportional to the fermions mass, the process  $e^- e^+ \rightarrow H$  processes is highly suppressed<sup>3</sup> and, for this reason, there were not enough statistics of events with a Higgs boson. The most favoured way of producing a Higgs boson is trough the mediation of the heaviest fundamental particles in the SM because these have the strongest couplings with the Higgs and, consequently, the greater cross section.

The four most dominant processes for Higgs boson production at LHC are summarised in Figure 2.16:

- **Gluon-gluon Fusion (ggF):** This channel is depicted in Figure 2.16a and, as the diagram shows, the process  $gg \rightarrow H$  has to be mediated by a massive fermion loop. This due to the fact that there is no direct gluon-Higgs coupling within the SM. Although in principle all quarks should be included in the loop, in practise it is the top quark the one doing so because its coupling to the Higgs boson is 35 times stronger than the next-heaviest fermion, the bottom quark.

Due to the abundance of gluons in  $pp$  collisions, the ggF is very favoured at LHC.

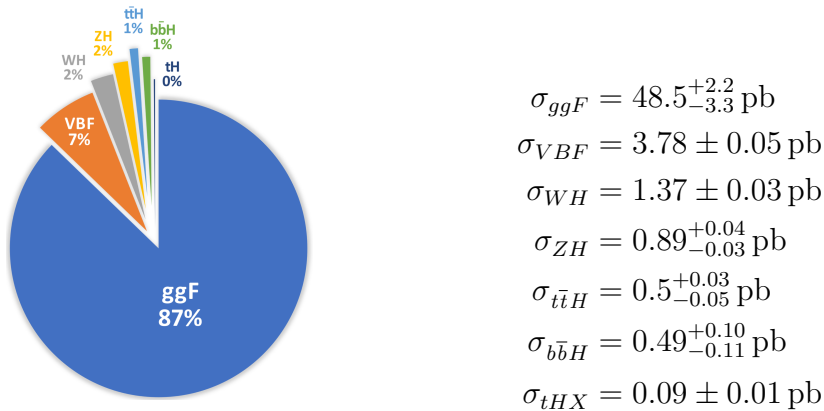
- **Vector Boson Fusion (VBF):** The second most important is the radiation by the incoming quarks of a  $W$  or  $Z$  vector bosons that fuse to from a Higgs as Figure 2.16b illustrates. The vector bosons of

<sup>3</sup>The dominant Higgs production in  $e^- e^+$  annihilation is the so called Higgsstrahlung, an  $s$ -channel process in which the  $H$  is produced in association to a  $Z$  boson similarly to Figure 2.16c.

the process  $V\bar{V} \rightarrow H$  are originated from initial state quarks which scatter thorough the final state (changing its flavours in the case of  $W$  fusion) producing two forward jets.

- **Higgsstrahlung (VH):** There is another significant contribution involving the  $W$  or  $Z$  bosons, the Higgsstrahlung or associated  $WH$  or  $ZH$  production. Here, a, off-shell  $W$  or  $Z$  (formed from the annihilation of two quarks) radiate a Higgs boson via  $V^* \rightarrow VH$ . Figure 2.16c depicts the VH associated production.
- **Quark-pair associated production ( $q\bar{q}H$ ):** In this mode, the Higgs is produced from a  $q\bar{q}$  pair via  $q\bar{q} \rightarrow H$  with a  $q\bar{q}H$  final state. Typically, the involved quark pair is either a  $b\bar{b}$  or  $t\bar{t}$ . In the case of  $t\bar{t}$  (Figure 2.16d), the top quarks decay before hadronising, leading to final states with a high number of physics objects.
- **Associated Higgs boson and single-top quark ( $tHX$ ):** This sub-dominant contribution can be either a  $tHq$  or a  $tWH$ . The former constitutes the central topic developed in this thesis, where this process is searched. Details about this production modes are further discussed in Section 2.3.2 .

The cross section of the different procedures for Higgs boson production at  $\sqrt{s} = 13$  TeV are shown in Figure 2.17 as a function of  $m_H$ . For Figure 2.17a, the  $\sigma_{tH}$  accounts for the  $t$ -channel and  $s$ -channel but not the  $tW$ -channel. Assuming a  $m_H = 125.2$  GeV, the cross-sections for Higgs production are [4]:



### 2.2.3 Higgs-boson decay

The Higgs boson has a very short lifetime ( $\tau_H = 1.6 \times 10^{-22}$  s [4]) and, hence, is always detected through its decay products. Figure 2.18 shows

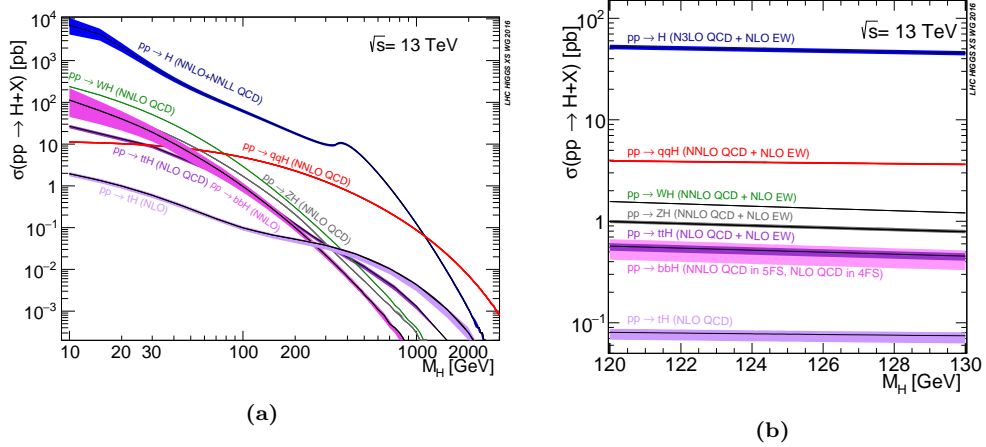


**Figure 2.17:** Higgs boson production cross sections as function of  $m_H$  at  $\sqrt{s} = 13$  TeV [4].

the branching ratio<sup>4</sup> (BR) for the Higgs boson. Looking at Figure 2.18a it can be seen that if the Higgs weighted just about 50 GeV more there would have been only two relevant decay modes,  $H \rightarrow WW$  and  $H \rightarrow ZZ$ .

Despite the expected large Yukawa coupling between the Higgs boson and the top quark, the  $H \rightarrow t\bar{t}$  is forbidden because the  $m_H < 2m_{top}$ . Consequently, the most prominent decay mode is the  $H \rightarrow b\bar{b}$  followed by the  $H \rightarrow W^+W^-$ . For the rest fermionic decays, the decay rates are ordered by the fermion masses. Regardless of the expected large coupling between the weak force bosons and the Higgs, the  $H \rightarrow VV^*$  is suppressed due to the requirement that one vector boson has to be produced off-shell<sup>5</sup>.

**Higgs to tau tau is the most relevant higgs to fermions decay that can be observed Add some diagrams of the Higgs decay modes**

For the analysis carried in this thesis, are of particular the decays  $H \rightarrow W^+W^-$ ,  $H \rightarrow ZZ$  and  $H \rightarrow \tau^-\tau^+$ . Sorted by its importance and assuming a  $m_H = 125.2$  GeV, the BR for the Higgs are [72]:

<sup>4</sup>The fraction of particles which decay by an individual decay mode with respect to the total number of particles which decay.

<sup>5</sup>Off-shell means that the particle is produced virtually and it does not satisfy the energy-momentum relation.

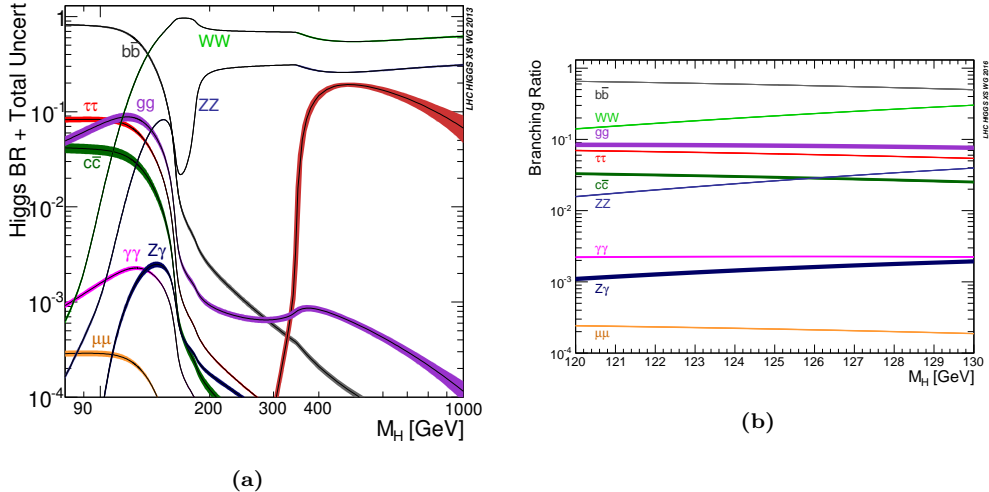
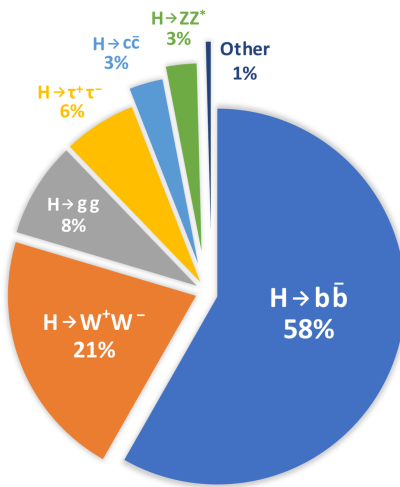


**Figure 2.18:** Standard Model Higgs-boson-decay branching ratios as function of  $m_H$  at  $\sqrt{s} = 13$  TeV citeLHCIGGSSWG2013.



$H \rightarrow b\bar{b}$	$(57.92 \pm 0.29)\%$
$H \rightarrow W^+ W^-$	$(21.70 \pm 0.11)\%$
$H \rightarrow gg$	$(8.17 \pm 0.26)\%$
$H \rightarrow \tau^+ \tau^-$	$(6.24 \pm 0.03)\%$
$H \rightarrow c\bar{c}$	$(2.888 \pm 0.014)\%$
$H \rightarrow ZZ$	$(2.667 \pm 0.013)\%$
$H \rightarrow \gamma\gamma$	$(2.270 \pm 0.023)\%$
$H \rightarrow \mu^+ \mu^-$	$(2.165 \pm 0.011)\%$
$H \rightarrow Z\gamma$	$(0.155 \pm 0.008)\%$
$H \rightarrow Others$	$< 0.2\%$

Just a small comment about that so far it has been studied the single Higgs production at LHC but during Run 3 the interest in double higgs production is increasing.

## 2.3 Top quark and Higgs boson interplay

So far, the couplings of the Higgs boson to the SM particles have been found to be proportional to the masses of these particles. Since the top quark is the most massive particle and the coupling of Higgs to SM particles is uniquely determined by the mass of these particles, the Yukawa coupling

between the top quark and the Higgs boson ( $y_t$ ) is expected to be the strongest among all fermions and, hence, its study is of crucial importance, as it is discussed in references [73][74] and developed in the succeeding sections.

The production of a pair or top quarks along with a Higgs boson ( $t\bar{t}H$ ) it is possible to measure the absolute value of  $y_t$ . This process has the advantage of being the leading mechanism to produce the Higgs together with the quark top. At  $\sqrt{s} = 13$  TeV it has a cross section of **poner cálculos del SM para  $\sigma_{t\bar{t}H}$**  (the definition of cross section can be found in Section 3.2.5).

Despite having a very much lower cross section than  $t\bar{t}H$  (**poner números**), the Higgs boson production alongside a single top quark ( $tHq$  or  $tH$ ) brings valuable information, specially regarding the sign of the Yukawa coupling. Note that the sign of  $y_t$  is not a well-defined physical property by itself but the relative sign compared to the coupling of the Higgs to weak<sup>6</sup> boson is indeed physical [73]. This is explored with more detail in 2.3.2.

A change in the Yukawa sign and/or absolute value with respect to its SM value would signal an origin of the fermion masses different from the described by the EWSB because the relative sign of the Higgs coupling to fermions and gauge vector bosons is crucial for recovering the unitarity and renormalizability of the theory s[75].

### All section 2.3 is work in progress

$\rightarrow \mathcal{CP}$  Properties of Higgs Boson Interactions with Top Quarks in the  $tH$  and  $t\bar{t}H$  processes at ATLAS: <https://inspirehep.net/literature/1790698>

Since only 1% of all Higgs bosons are produced in association with top quarks, the observation of such processes is very challenging. Notably, it is a immensely ambitious task to measure the associated production of a Higgs with a single top which has an extremely low cross section as can be seen in Figure 2.17b.

### 2.3.1 $t\bar{t}H$

The first associated production of a Higgs boson with a pair of top quarks was observed in 2008 by ATLAS [76] and CMS [77]. This process marked a significant milestone for the field of high-energy physics because it helped establishing the first direct measurement of the tree-level coupling

---

<sup>6</sup>The coupling of the Higgs to the gauge bosons is taken as positive.

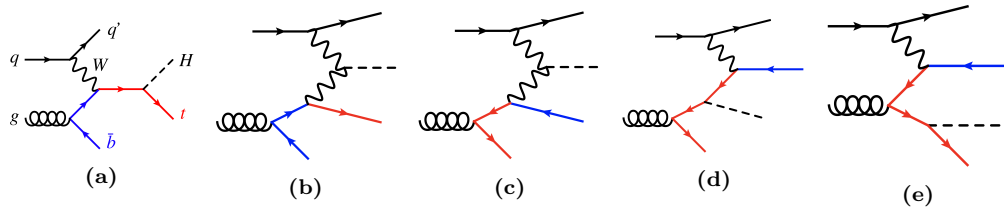


**Figure 2.19:** LO Feynman diagrams for  $t$ -channel  $tH$  production in the 4FS.

of the Higgs boson to the top quark, which was in agreement with the SM expectation.

The associated production of  $H$  with top quark pair has been studied by ATLAS and CMS previously during Run-1 at  $\sqrt{s} = 7$  TeV and 8 TeV [78] [79] and Run-2 [buscar  $t\bar{t}H$  en Run-2]

### 2.3.1.1 $t\bar{t}H$ Standard Model

### 2.3.1.2 $t\bar{t}H$ Charge-Parity

## 2.3.2 $tHq$

The  $tH$  production is divided in  $tHq$  and  $tWH$ .

### $tHq$ production modes

At LO, the production of a Higgs boson in association with a single top quark and additional parton ( $tHq$ ) in  $pp$  collisions is classified in three groups according to the virtuality of the  $W$  boson. These groups are:  $t$ -channel production,  $s$ -channel production and associated production with an on-shell  $W$  boson. This categorisation is the same as for the single-top-quark (Section 2.1.2.2), which makes sense since the  $tHq$  production is, basically, a single-top-quark process in which a Higgs boson is radiated either from the  $W$  or the top.

In the  $t$ -channel production modes are classified in 4FS and 5FS as it is done for the single-top case. The 4FS and the 5FS modes are shown in Figures 2.19 and 2.19 respectively. For the 4FS modes, the diagrams in which the gluon decays to a top pair (2.19c, 2.19d and 2.19e) contribute less than the ones in which it does to a  $b\bar{b}$  (2.19a and 2.19b).

Poner las tablas para las cross section de Demartin [3] para  $t$ -channel y  $s$ -channel

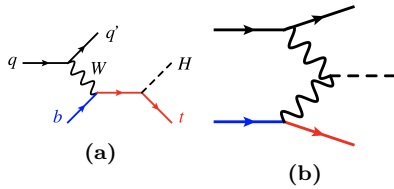


**Figure 2.20:** LO Feynman diagrams for  $t$ -channel  $tH$  production in the 5FS.

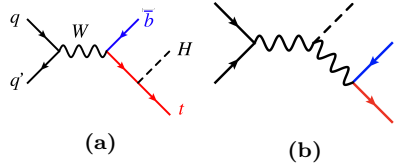


**Figure 2.21:** LO Feynman diagrams for  $s$ -channel  $tH$  production in the 5FS.

Since the  $s$ -channel contribution is so small to the total cross section of the  $tHq$  process,

For  $tH$  and single-top-quark production at colliders, the 5FS calculations are easier than the 4FS due to the lesser final state-multiplicity and smaller phase space. This is why in the 5FS the single-top production is known at NNLO while the 4FS this is done only for NLO. Another advantage of the 5FS is that the  $t$ -channel,  $s$ -channel and associated  $tWH$  production do not interfere until NNLO. Contrary, the in 4FS, the  $t$ -channel at NLO and  $s$ -channel at NNLO can interfere. Nevertheless, this interferences are very small and can be neglected [3].

**Poner algo en información del  $tWH$  production mode para  $tH$**   
**y** The  $tWH$  production is a background in the  $tHq$  analysis.

In reference 2.22 is shown that the shapes of the distributions of most observables in the  $s$ -channel differ significantly from those of the  $t$ -channel. So, even though the total cross section of the  $tHq$  production with the  $s$ -channel is much more smaller than the one for  $t$ -channel, one could think that including the  $s$ -channel in the analysis would increase the precision. This is not the case because the LHC is not sensible for to the  $tHq$  production via the  $s$ -channel. In fact, not even the  $s$ -channel-single-top production (without any associated Higgs boson) has been found at LHC.

**Summarise production modes described in [3]**

### **$tHq$ sensibility to $y_t$**

As already commented in the introduction of the Section 2.3, the main interest of the  $tHq$  process is that it is among the few processes in the LHC that are sensible to the relative size and phase between the couplings of the

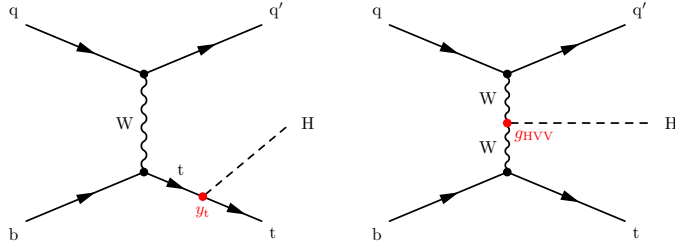


**Figure 2.22:** Representative LO Feynman diagrams for the  $t$ -channel  $tHq$  associated production, where the Higgs boson couples either to the top quark (left) or the  $W$  boson (right)

Higgs top and the Higgs to the gauge bosons. The other mechanisms to determine this relative sign are  $H \rightarrow \gamma\gamma$  and  $gg \rightarrow ZZ$ . This is due to the fact that in the SM the  $tHq$  production where the  $H$  couples to the  $W$  (Figure 2.22 right) interfere destructively with those in which the  $H$  is radiated from the top (Figure 2.22 left). As it is later explained in Section 3.2.5, the cross section is proportional to the square of the matrix element,  $\mathcal{M}$  and if there are several diagrams for a same process, the matrix elements have to be summed before squaring leading to interference terms. For the  $tHq$  production

$$\sigma_{tHq} \propto |\mathcal{M}_{qq \rightarrow tHq}|^2 = |\mathcal{M}_{qq \rightarrow tHq_{WH}} + \mathcal{M}_{qq \rightarrow tHq_{tH}}|^2 \quad (2.1)$$

When squaring the scattering amplitude, the destructive interference<sup>7</sup> term decreases the  $\sigma_{tHq}$ . This behaviour makes the  $tHq$  cross section exceptionally sensible to the departures of  $y_t$  from the SM predictions. Typically, the destructive interference yields a reduction in the rate as compared to the contribution from each individual diagram by about an order of magnitude [80]. Therefore, in the presence of non-SM new physics, a positive relative sign between the  $tH$  and the  $WH$  couplings would imply that the amount of  $tHq$  events recorded should increase a factor of  $\sim 13$  over the SM expectations, surpassing the number of events from  $t\bar{t}H$  production [81].

The  $tHq$  production has been studied at LHC Run-1 by CMS [82]

**Usar los papers the  $tHq$  de CMS la sección 5 de Demartin [3]**

<sup>7</sup>By destructive interference is meant that the relative sign between  $\mathcal{M}_{qq \rightarrow tHq_{WH}}$  and  $\mathcal{M}_{qq \rightarrow tHq_{tH}}$  is negative.

**2.3.2.1  $tH$  Standard Model****2.3.2.2  $tH$  Charge-Parity****2.3.2.3 ATLAS and CMS results**

In order to gather the necessary information, the widest campaign of measurements has to be undertaken, including as many possible decay modes. In this context, the scope of this thesis is the study of the production  $tH$  with a final state characterised by two light leptons ( $\ell$ ), i.e. electrons ( $e^\pm$ ) or muons ( $\mu^\pm$ ), and one hadronically decaying tau lepton ( $\tau_{\text{had}}$ ). This signature is usually referred as dileptau or lep-had channel and is denoted by  $2\ell + 1\tau_{\text{had}}$ .

# Chapter 3

## The ATLAS experiment at the Large Hadron Collider of CERN laboratory

The work developed in this thesis is framed in the context of the ATLAS detector [83], a general-purpose particle physics detector registering the events originated from the collisions produced by the largest and most powerful particle accelerator built up to this date, the LHC. This experimental setup is located in one of the largest and most renowned centres for scientific research in the world, the CERN.

This chapter is devoted to the introduction of the CERN laboratory and a description of the technical design of LHC and ATLAS. The CERN organisation is presented through an overview of its history, its achievements and some of the most relevant research projects carried out currently. The essential technical aspects of the LHC machine design are covered. The distribution and functioning of the accelerator complex and the main experiments conducted at LHC are summarised as well. Finally, a full overview of the different components of the ATLAS detector is exposed, presenting the specific features of each of its parts.

### 3.1 CERN

The European Organization for Nuclear Research, known as CERN, is the largest particle physics laboratory in the world. The convention establishing CERN was ratified in 1954. Its name is derived from the French acronym *Conseil Européen pour la Recherche Nucléaire*, which was the provisional body designated in 1952 to foster the fundamental physics research

in Europe, and the acronym has been maintained until CERN's foundation. Initially formed by 12 member states, now it has 23 member states and many non-European countries involved in different ways such as associate members, partners and observers [84].

The main site of the laboratory is located at Meyrin, a municipality of the Canton of Geneva (Switzerland), at the Franco-Swiss border. There are other sites in the vicinity of the Meyrin site, being the most relevant the Prévessin Site, the CERN's second-largest site, straddling the communes of Prévessin-Moën (France).

Since its beginning, CERN's objective has been helping to uncover what the universe is made of and how it works. CERN started its first accelerator, the Synchrocyclotron, on 1957 and rapidly observed the electron decay of the pion for the very first time [85]. Thereafter, the laboratory has continued contributing to not only particle and nuclear physics but also more technical fields. For instance, one of the most important achievements made through CERN experiments is the discovery in 1973 of neutral currents in the Gargamelle bubble chamber installed in the Proton Synchrotron (PS) [86]. This observation was an indirect evidence for the existence of the  $Z$  boson and ten years later, in 1983, CERN announced the discovery of the  $Z$  and  $W$  bosons [87]. This finding was done at the UA1 and UA2 experiments, located within the Super Proton Synchrotron (SPS), and it was awarded with the laboratory first Nobel Prize in 1984. Other major successes of CERN were the determination of the number of light neutrino families at the Large Electron-Positron Collider (LEP) on 1995 [88] and the creation for the very first time of antihydrogen atoms in 1995 at the PS210 experiment [89]. More crucial accomplishment followed such as the discovery during the 1990's of  $\mathcal{CP}$  violation by NA31 [90] and NA48 experiments [91]. And, in 2012, the Higgs boson discovery by ATLAS and CMS[1] [2], a fundamental test for the robustness of the SM as described in Section 2.2.1. More recently, in 2015, a state consistent with a pentaquark was observed at LHCb [92].

Currently, a wide diversity of projects are carried at CERN being the most renowned of them the LHC and its experiments which are described in more detail in Section 3.2. In addition, fixed-target experiments, antimatter experiments and experimental facilities make use of the LHC injector chain. The main fixed-target experiments at CERN are the Antiproton Decelerator (AD) [93] for slowing antiprotons for the antimatter factory [94] and the On-Line Isotope Mass Separator (ISOLDE) facility for short-lived ions [95]. The world's first proton-driven plasma wakefield acceleration experiment is also at CERN, the Advanced Proton Driven Plasma Wakefield Acceleration Experiment (AWAKE) [96]. In the International Space Station (ISS), the

Parameter	Design	Run-1	Run-2	Run-3	HL-LHC
Beam energy	7	3.5 - 4	6.5	7	7
Center-of-mass energy ( $\sqrt{s}$ ) [TeV]	14	7 - 8	13	13.6	14
Bunch spacing [ns]	25	50	25	25	25
Bunch Intensity [ $10^{11}$ ppb]	1.15	1.6	1.2	up to 1.8	2.2
Number of bunches ( $n_b$ )	2800	1400	2500	2800	2800
Transverse emittance ( $\epsilon$ ) [ $\mu\text{m}$ ]	3.5	2.2	2.2	2.5	2.5
Amplitude function at the interaction point ( $\beta^*$ )[cm]	55	80	30→25	30→25	down to 15
Crossing angle [ $\mu\text{rad}$ ]	285	-	300→260	300→260	TBD
Peak Luminosity [ $10^{34} \text{ cm}^2 \text{ s}^{-1}$ ]	1.0	0.8	2.0	2.0	5.0
Peak pileup	25	45	60	55	150
Nominal magnetic field ( $B$ ) [T]	8.73	4.16 - 7.76	7.73	8.73	8.73
Injection energy [GeV]				450	
Circumference length [km]				26.7	
Radius [km]				4.24	
Number of dipole magnets				1232	
Length of dipole magnets [m]				14.3	
Number of quadrupole magnets				395	
Total mass [tons]				27.5	

**Table 3.1:** Summary of main accelerator parameters for the LHC, showing the design values, and those used during Run-1 and Run-2, as well as the expected parameters for Run-3 and the HL-LHC.

Alpha Magnetic Spectrometer (AMS) tries to observe dark matter [97]. The research programme at CERN covers topics from the basic structure of matter to cosmic rays, and from the SM to supersymmetry.

## 3.2 Large Hadron Collider

In the mid of the decade of 1980, the plans for building the Large Hadron Collider (LHC) were started. At several high-energy physics workshops and conferences, the idea of assembling a machine able to reach multi-TeV energies was discussed. This instrument would allow physicists to search for the Higgs boson at all possible masses. In 1991 the Long-Range Planning Committee of CERN proposed the construction of the LHC as the best step forward in CERN’s future [98]. The approval of the LHC project arrived in 1994 and in 1995 the Conceptual Design Report was published [99]. Finally, on 10 September 2008, a beam of protons was successfully directed into the LHC pipes for the first time.

A summary of the main parameters of LHC for  $pp$  collisions is presented in Table 3.1. These parameters are shown for how the machine was designed, for Run-1 (2011-2012) and Run-2 (2015-2018) as well as the expected parameters for Run-3 (2025-2027). The forecasted values for the High Luminosity (HL) LHC upgrade (after 2027) are exposed too.

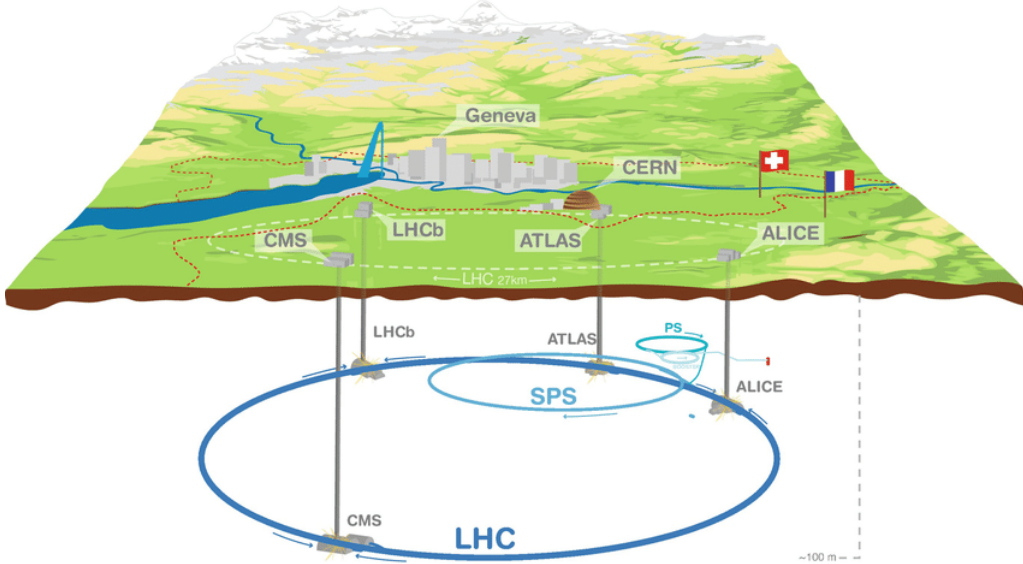


**Figure 3.1:** Overall view of the LHC including the ATLAS, CMS, ALICE and LHCb experiments. [This image duplicates the information of Figure 3.4](#)

### 3.2.1 Machine design

The LHC is a circular hadron accelerator with a circumference of 27 km. Located where once was the LEP collider, the accelerator used by CERN from 1999 to 2000 [100], the LHC tunnels are almost entirely outside the main site, being mainly on french territory. An overall schematic view of the LHC is shown in Figure 3.1.

The LHC has two rings with ultra-high vacuum (to prevent collisions with gas molecules while moving through the accelerator) inside of which particle beams travel in opposite directions. It was designed to accelerate and collide proton beams with a center-of-mass energy ( $\sqrt{s}$ ) up to 14 TeV at a luminosity ( $\mathcal{L}$ ) of  $10^{34} \text{ cm}^2 \text{ s}^{-1}$  (see Section 3.2.5 for details about luminosity). As well as protons, it can collide heavy ions, in particular lead nuclei, at  $\sqrt{s} = 2.3 \text{ TeV}$  per nucleon and a peak luminosity of  $\mathcal{L} = 10^{27} \text{ cm}^2 \text{ s}^{-1}$  [101]. These specifications make the LHC the accelerator with higher collision energy [102].

The beams in the LHC are made up of bunches of protons that are spaced 7 m apart and collide every 25 ns. Each bunch contains around  $1.1 \times 10^{11}$  hadrons, being 2556 the maximum possible number of bunches that can be reached with the beam preparation method currently used [103]. The size of each bunch is approximately 25 cm [104].

The LEP tunnel lies between 45 m and 170 m below the surface on a plane sloping towards the Léman lake. The underground

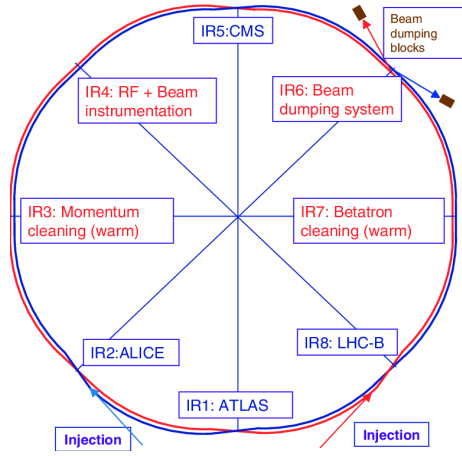


**Figure 3.2:** Schematic layout of the LHC (Beam 1clockwise, Beam 2 anti-clockwise).

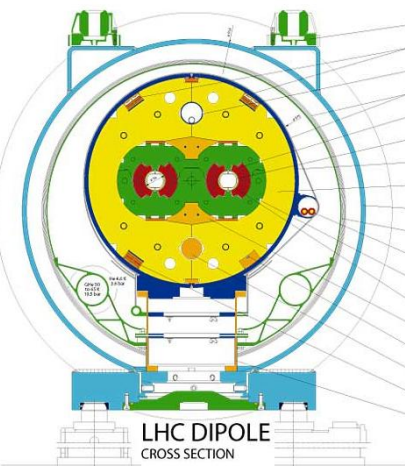


**Figure 3.3:** LHC dipole cross section.

construction adds some shielding from outside interferences that could interact with the detectors and cause anomalous readings. Even 100 m underground, the cosmic rays can reach the detectors, so these are used to help to calibrate them. The tunnel has an internal diameter of 3.7 m, which makes it extremely difficult to install two completely separate proton rings [105] as in the Superconducting Super Collider (SSC). Therefore, the counter-rotating rings are built under the *two-in-one* twin-bore superconducting magnet design. These twin bore configurations have the disadvantage of having the rings magnetically coupled, which adversely affects flexibility [106]. Figure 3.3 shows an example of the LHC twin-bore dipole magnet.

The LHC is not a perfect circle. Approximately 22 km of the LHC ring consists of 8 curved sections. The remaining 5 km of the tunnel are made of 8 straight sections, denominated insertion regions (IR), that provide space for the experiments. Figure 3.2 shows the distribution of IR and crossing points for the LHC. This layout follows that of the LEP tunnel. The number of crossing points where the beams pass from one ring to the other for colliding was decreased from the original eight at LEP to four in the LHC in order to reduce costs and optimise the utility insertions containing Radio Frequency (RF), the collimation and the beam dump systems [99].

The arcs contain the dipole bending magnets, which are shown in Section 3.3. The 1232 twin-bore magnets curve the trajectory of the particle beam that would, otherwise, follow a straight line. Dipoles are also equipped with additional multipole lattice magnets (sextupole, octupole and decapole), which correct for small imperfections in the magnetic field at the extremities of the dipoles.

Each of the eight straight sections is approximately 528 m long. The RF cavities delivering 2 MV (an accelerating field of 5 MV/m) at 400 MHz are located in the IR4. The 16 RF cavities compensate the synchrotron radiation losses (the electromagnetic radiation emitted when charged particles travel in curved paths) that take place at the arcs of LHC. The energy radiated per particle by synchrotron radiation is proportional to the inverse of the mass of the particle:  $\Delta E \propto 1/m^4$ . This radiation is, thus, smaller for protons than for electrons. That is why the LHC machine has much less synchrotron radiation losses than the LEP and its design would ideally have longer arcs and shorter straight sections for the same circumference. But using the tunnel as built for LEP was the cost-effective solution. During the 20 minutes that are needed to reach the beams maximum energy, the bunches have passed the RF cavities more than 10 million times [99].

The RF cavities (also known as resonators) are metallic chambers spaced at intervals along the accelerator shaped to resonate at specific frequencies, allowing radio waves to interact with passing particle bunches. The main role of the RF cavities is to keep the proton bunches tightly packed to ensure the required luminosity at the interaction point. They also transfer RF power to the beam to accelerate it to the top energy [107].

At the insertion of the arc and straight sections, quadrupole magnets are installed to suppress the dispersion of particles. Acting as focal lenses, quadrupole magnets gather the particles together. This system not only cancels the horizontal dispersion arising in the arc but also adapts the LHC reference orbit to the geometry of the LEP tunnel. Before entering the detectors, the inner triplets (which are made mostly from quadrupoles) tighten the beam, from  $0.2 \times 10^{-3}$  m down to  $16 \times 10^{-6}$  m. These are known as insertion magnets.

In total there are more than 9000 magnets all over the LHC and more than 50 types of magnets are needed to make the particles circulate in their path without losing speed. The coils are made of niobium-titanium (NbTi) which is cooled to less than 2 K with superfluid helium to reach superconductivity.

### 3.2.2 Accelerator complex

To accelerate the proton beams, the existing CERN accelerator complex is used. These accelerators were, back in the day, the state of the art colliders and now they serve as injection system for the LHC. The path followed by the particle beams is presented in Figure 3.4. The accelerator complex consists in several machines interconnected with higher and higher capabilities, i.e. the beams are injected from one accelerator to the next in

sequence, boosting the particles to higher energies in each step until they enter into the LHC.

The proton bunches are produced ionising a gas of hydrogen atoms and then they are accelerated to a momentum of 50 MeV by the linear accelerator (LINAC2). Starting from Run-3, the LINAC2 is being replaced by the LINAC4. After being produced, the beams enter into the first circular accelerator, the Proton Synchrotron Booster (PSB) which has 630 m radius and increases the energy of the protons until 1.4 GeV.

The main advantage of circular accelerators compared to linear ones is that they can speed up particles with much less physical space. Circular accelerators ramp up two different beams with opposite charges at the same time with a single magnetic field. The maximum energy transferred to the beams in a circular accelerator is given by  $p_T$  [GeV] =  $0.3qB[T]r[m]$ , being  $p_T$  the transverse momentum of the particles,  $q$  the charge of the particles ( $q = 1$  for protons),  $B$  the magnetic field applied and  $r$  the radius of the circular accelerator.

Right after the PSB, the Proton Synchrotron brings the particles 25 GeV. The next step in the chain raises the energy to 450 GeV. This is done by the SPS, which is 6.9 km long. Once the protons have 450 GeV, the minimum energy at which the LHC can maintain a stable beam, they are injected into the LHC by two different 2 km-long Transfer Injection (TI) lines [108]. Protons will circulate in the LHC for 20 minutes until reaching the maximum speed and energy (650 GeV per beam) [106].

Heavy-ion collisions were included in the conceptual design of the LHC from an early stage. Lead ions for the LHC are extracted from a source of vaporised lead and enter LINAC3 before being collected and accelerated in the Low Energy Ion Ring (LEIR). They, then, follow the same route to maximum acceleration as the protons [106].

### 3.2.3 LHC Experiments

In the LHC four major experiments are carried, each of them with its own detector (Figure 3.5). These particle detectors measure particles produced as debris from the  $pp$  collisions through the interaction with the material of the sub-detectors. Distributed along the collider as is shown in Figures 3.1, 3.2 and 3.4, these highly sophisticated experiments are:

- **A Toroidal LHC ApparatuS (ATLAS)** [109]: Located in the IR1, it is a generic multi-purpose experiment for high luminosity (up to  $\mathcal{L} = 10^{34} \text{ cm}^2 \text{ s}^{-1}$ ). It studies  $pp$  collisions and investigates a wide range

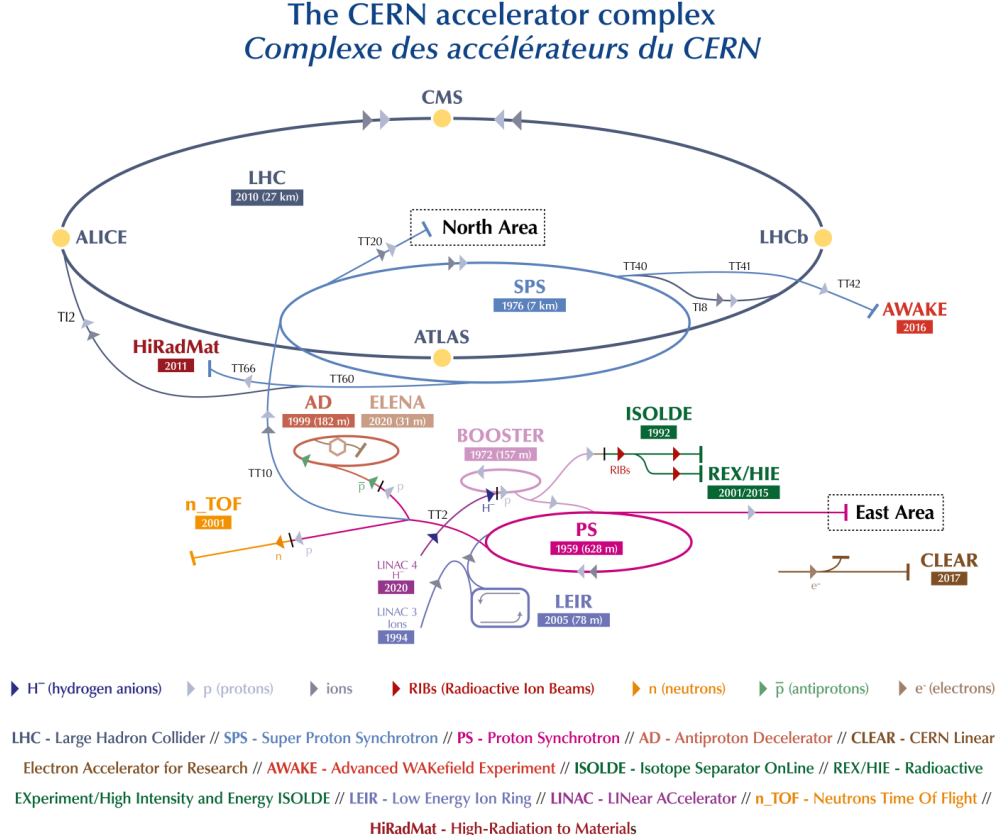


**Figure 3.4:** Scheme of CERN accelerator complex. Protons are injected from the LINAC2 into the PS Booster, then the PS, followed by the SPS, before finally reaching the LHC.

of physics, from the SM to the search for extra dimensions or dark matter. It has the dimensions of a cylinder, 46 m long, 25 m in diameter. The ATLAS detector weighs  $7 \times 10^3$  tonnes. The design of the ATLAS detector features excellent jet and  $E_T^{\text{miss}}$  resolution, particle identification and flavour tagging and standalone muon measurements. A scheme of this detector is shown in Figure 3.5a. ATLAS will be covered in detail in Section 3.3.

- **Compact Muon Solenoid (CMS)** [110]: Built inside the IR5, it's the other general-purpose experiment for high luminosity (same  $\mathcal{L}$  as ATLAS). CMS has the same objectives and goals as ATLAS but both its hardware and software designs are different. Even though CMS is smaller than ATLAS (21 m long, 15 m in diameter) it is much heavier, weighting  $14 \times 10^3$  tonnes. The bulk of its weight is the steel yoke that confines the 4 T magnetic field of its superconducting solenoid.

The design of CMS emphasises magnificent electron/photon energy and momentum resolution. Figure ?? illustrates this device. The role of coexistence of CMS and ATLAS is fundamental so that one can verify and confirm the experiments of the other independently.

- **Large Hadron Collider beauty (LHCb)** [111]: Hosted at IR2, it is a lower luminosity experiment designed to study the small asymmetries between matter and antimatter through  $\mathcal{CP}$  violation using rare decays of  $b$ -quark based hadrons. The detector is arranged as a succession of planar sub-detectors (as can be seen in Figure 3.5c) since most of the  $b$ -flavoured mesons follow the beam pipe direction when created in the  $pp$  collision. LHCb delivers remarkable low-momentum track reconstruction and particle identification.
- **A Large Ion Collider Experiment (ALICE)** [112]: It is a low luminosity experiment in IR8 that focuses on QCD. The main feature of ALICE is a general-purpose detector that it uses heavy-ion collisions to study matter interacting at extreme densities and temperatures, thus reproducing the quark-gluon plasma. This detector is shown in Figure 3.5d and it provides highly efficient track reconstruction in an environment full of heavy ions. Besides running with Pb ions, the physics programme includes collisions with lighter ions, lower energy collisions and a dedicated proton-nucleus run.

Along the LHC machine, there are other experiments much more smaller than ATLAS, CMS, LHCb and ALICE, typically sharing the cavern with the major projects. The most relevant among the minor experiments are LHCf [113], MATHUSLA [114], MilliQan [115], MoEDAL [116], TOTEM [117] and FASER [118].

### 3.2.4 LHC Computing grid

The data collected by the different LHC experiments is stored, processed and, then, made available for all the researchers of each collaboration<sup>1</sup>. This is possible thanks to the last piece of the LHC, its computing model and infrastructure: the LHC Computing Grid (LCG). It consists of several computing farms distributed around the world and interconnected. Figure 3.6 shows the geographical distribution of the different facilities that comprise the LCG. Just as the WWW enables access to information, the Grid enables access to computer resources. Employing a grid certificate, is possible for any user to run jobs on the grid and to access the data stored. The

---

<sup>1</sup>Within the grid context, each collaboration is known as Virtual Organisation (VO).

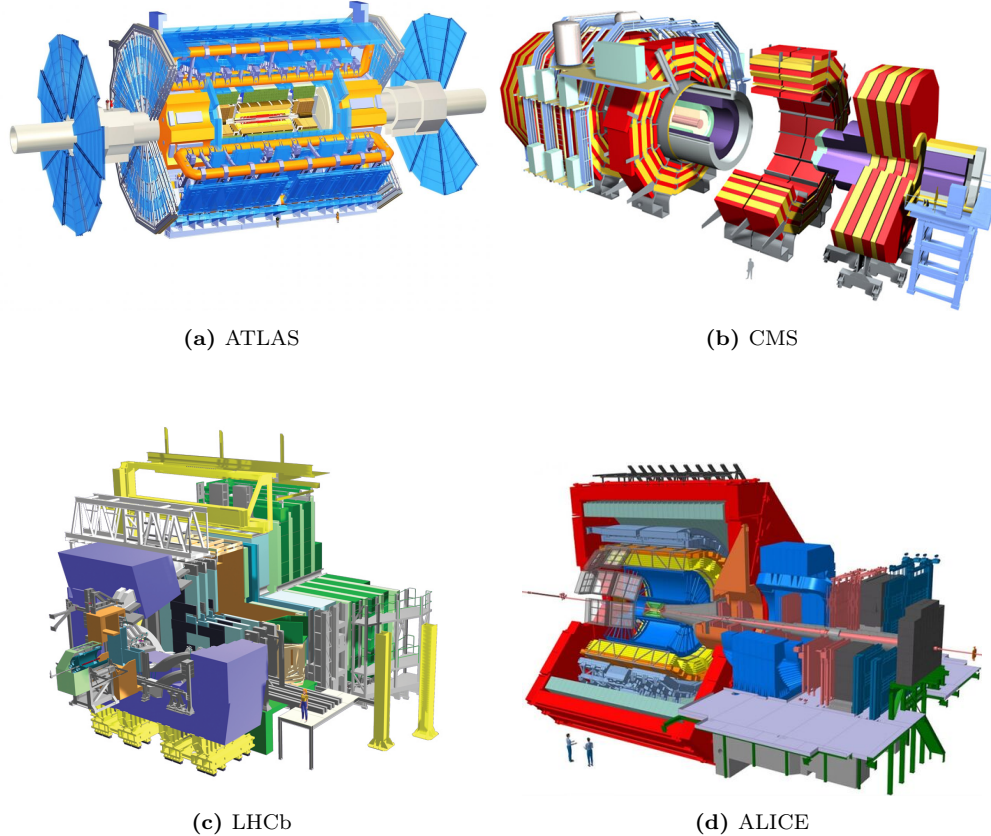


**Figure 3.5:** Scheme of LHC main experiments. Note that the images are not equally scaled.

implementation of the grid model implies an effective coordination among all LHC collaboration centres [119].

Different types of computing centres have been defined and classified in Tiers [121]:

- **Tier-0:** This facility is located at CERN and it is responsible for archiving (first copy) and distributing the raw data received from the Event Filter, i.e., the data emerging from the Data Acquisition systems (DAQ) after the trigger. It provides prompt reconstruction and distributes a copy of the raw data to the Tier-1 centres.
- **Tier-1:** These facilities archive the raw data permanently and provide the computational capacity for reprocessing and for physical analysis. It also stores the simulated and reprocessed data. Currently, there are thirteen large computer centres serving as Tier-1 (see Figure 3.7). These make data available to their Tier-2 centres [122].



**Figure 3.6:** Worldwide LHC Computing Grid geolocalisation of sites [120].

- **Tier-2:** Typically located at universities and other scientific institutes, there are more than 150 Tier-2 sites. The derived datasets produced by the physics groups are copied to the Tier-2 facilities for further analysis. The MC simulations for event production are executed at this level.
- **Tier-3:** The local computing resources, from local clusters to even just an individual PC are referred to as Tier-3. There is no formal engagement between worldwide LCG and the Tier-3.

This system provides near real-time access to LHC data. The LCG collaboration spreads out over 42 countries with 170 computing centres and 1 million computer cores, being the world's largest computer grid. It deals with over two million tasks daily. These specifications make the LCG the most sophisticated system for data taking and analysis ever built for science.

### 3.2.5 Energy, Luminosity and Cross-section

#### Energy

Another name to refer to the field of Particle Physics is “high energy physics”. Particles such as the Higgs boson or the top quark are more than 100 times heavier than the proton so, in order to produce them, huge energies are required. The center-of-mass energy,  $\sqrt{s}$ , allows the production of physical effects. The greater the energy is, the bigger is the range of the different processes that can be produced by the accelerator.

The four-vector,  $\mathbf{p} = (E, \vec{p})$ , of a particle of mass  $m$  describes its kinematics with its energy  $E$  and  $\vec{p}$ . The square of the four-vector,  $\mathbf{p}^2$ , cor-

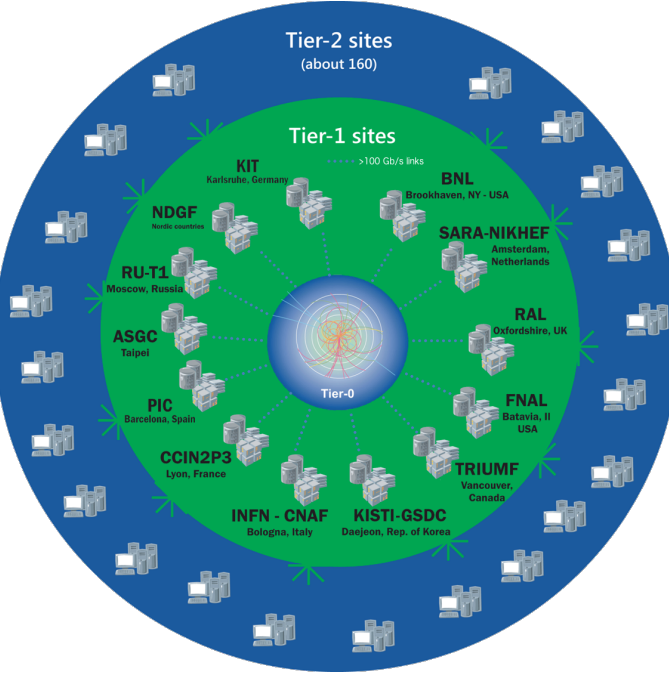


**Figure 3.7:** Distribution by Tiers of the LCG [122]. This project provides global computing resources to store, distribute and analyse the data recorded at the LHC.

responds to the particle mass:

$$p^2 = E^2 - \vec{p}^2 = m^2 \quad (3.1)$$

When two particles of mass  $m_1$  and  $m_2$  and momenta  $\vec{p}_1$  and  $\vec{p}_2$  respectively collide, the center of mass energy,  $\sqrt{s}$ , can be expressed as:

$$s = E_{CM}^2 = (p_1 + p_2)^2 = (E_1 + E_2)^2 - (\vec{p}_1 + \vec{p}_2)^2 \quad (3.2)$$

For symmetric colliding beams, such those of LHC, the collision point is at rest in the laboratory frame ( $\vec{p}_1 = -\vec{p}_2$ ) and, hence, the energy is

$$s = E_{CM}^2 = (E_1 + E_2)^2 \quad (3.3)$$

Since the energy of each beam is 650 GeV during Run-2, the center of mass energy of LHC collisions is

$$\sqrt{s} = E_{CM} = (E_{beam1} + E_{beam2}) = 650 \text{ GeV} + 650 \text{ GeV} = 13 \text{ TeV} \quad (3.4)$$

### Luminosity

Besides  $\sqrt{s}$ , the luminosity is the most relevant parameter in an experiment,

especially in searches for events with small cross-section. It measures the ability of the particle accelerator to produce enough events of the desired type.

The luminosity,  $\mathcal{L}$ , is the ratio of events detected in a certain period of time for a given cross-section ( $\sigma$ ):

$$\mathcal{L} = \frac{1}{\sigma} \frac{dN}{dt} = \frac{1}{\sigma} R \quad (3.5)$$

where  $N$  is the number of the events and  $t$  the time.  $R = \frac{dN}{dt}$  is known as reaction rate. It can be understood as number of particle collision per unit area (typically expressed in  $\text{cm}^2$ ) and per second, therefore it is measured in  $\text{cm}^2 \text{s}^{-1}$  [123]. For instance, for LEP was  $\mathcal{L}_{LEP} = 1.0 \times 10^{32} \text{ cm}^2 \text{s}^{-1}$  and the LHC is designed to achieve  $\mathcal{L}_{LHC_{pp}} = 2.1 \times 10^{34} \text{ cm}^2 \text{s}^{-1}$  in  $pp$  collisions and  $\mathcal{L}_{LHC_{PbPb}} = 6.1 \times 10^{27} \text{ cm}^2 \text{s}^{-1}$  for heavy ion collisions.

For two beams colliding, the instantaneous luminosity is proportional to the number of bunches per beam ( $n_1$  and  $n_2$ ), the revolution frequency ( $f$ ) with which the bunches are crossing and the number of proton bunches in the machine ( $n_b$ ), and it is and inversely proportional to the beams effective transverse area in which the collision takes places (Area =  $4\pi\sigma_x\sigma_y$ )

$$\mathcal{L} = f \cdot \frac{n_1 n_2 n_b}{4\pi\sigma_x\sigma_y} \cdot F(\theta_c, \sigma_x, \sigma_z) \quad (3.6)$$

where  $F(\theta_c, \sigma_x, \sigma_z)$  is a factor accounting for the luminosity reduction due to the beam crossing angle ( $\theta_c$ ). At the LHC, assuming that the particles travel at the speed of light, for its 27 km, the bunch crossing frequency is  $f = 11245.5 \text{ Hz}$ . The maximum number of proton bunches in the machine with 25 ns slots is<sup>2</sup>  $n_b = 2808$ . In each bunch there are  $n_1 \approx n_2 \approx 1.15 \times 10^{11}$  particles. Finally, characterising the optics of the collision at the interaction point (IP), the RMS transverse beam width in the horizontal and vertical directions are  $\sigma_x \approx \sigma_y \approx 12, \dots, 50 \mu\text{m}$ . The expression 3.6 assumes that the particles in the beam are Gaussian distributed. According to equation 3.6 the instantaneous luminosity only depends on the machine and its beam parameters [124][125].

The integrated luminosity over time is given by

$$L = \int \mathcal{L} dt \quad (3.7)$$

and it is used to determine the number of events,  $N$ , that have taken place during that time:  $N = \sigma \times L$ . The ability to observe low cross-section

---

<sup>2</sup>The theoretical maximum of 3564 bunches cannot be reached due to space needed between bunch trains and for the beam dump kicker magnets.

events is

$$N_{events}^{obs} = \sigma_{process} \times \text{efficiency} \times L \quad (3.8)$$

, where the efficiency of the detection is to be optimised by the experimental physicist, the integrated luminosity ( $L$ ) is delivered by LHC and the cross-section of the process ( $\sigma_{process}$ ) is given by nature.

On one hand, several factors can limit the maximum luminosity that can be achieved at LHC [123]:

- **Beam-beam effect:** The bunches of two beams or the particles in the same bunch can interact electromagnetically, this leads to distortions from the orbit and results in an increase of the emittance,  $\epsilon$ .
- **Crossing angle:** Often used to avoid unwanted collisions in machines with many bunches, due to the crossing angle  $\theta_c$ , the luminosity is reduced by a factor  $F(\theta_c, \sigma_x, \sigma_z) = \sqrt{1 + (\theta_c \sigma_z / 2\sigma x)^2}$ .
- **Beam offset:** Originated from the beam-beam effects or misalignments in the quadrupole magnets, the beams can collide with small transverse offset. Such beams' offsets induce a loss of  $\mathcal{L}$  at the interaction point.
- **Hourglass effect:** Appears when beams collide in a point away from the IP.

On the other hand, there are diverse strategies to maximise the luminosity delivered by a machine [124]:

- **Maximise the total beam current:** Improvements in beam collimation, cryogenics vacuum and background protection could extend the limit on the maximum beam current.
- **Compensate reduction factor:** The hourglass effect may be reduced by shorter bunches at the expense of a higher longitudinal pileup density (see Section 3.2.6).

The cumulative luminosity delivered by LHC to ATLAS during the Run-2 per year is shown in Figure 3.8. In Figure 3.9, the total Run-2 cumulative luminosity is presented differentiating between the delivered and recorded luminosity and showing that almost all delivered events are considered to be good data quality. The delivered luminosity accounts for the luminosity given from the start of stable beams until the LHC requests ATLAS to put the detector in a safe standby mode to allow a beam dump or beam studies. The recorded luminosity reflects the DAQ inefficiency, as well as

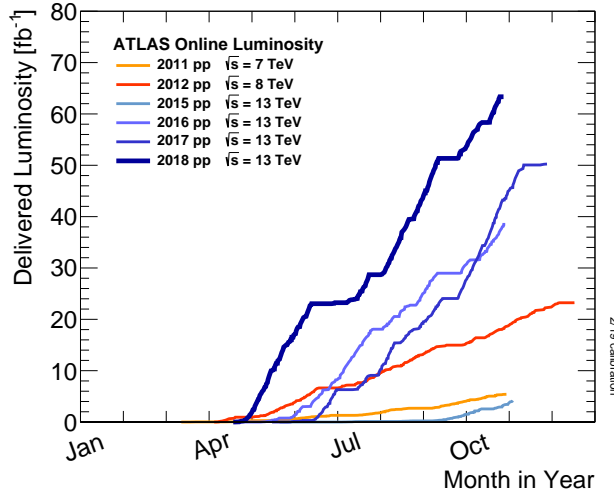


**Figure 3.8:** Cumulative luminosity versus day delivered to ATLAS during stable beams and for high energy  $pp$  collisions **Maybe it is not a good idea to put an ATLAS plot before introducing ATLAS. Move figure to section 4.2.1.5.**

Year	2015	2016	2017	2018
Peak instantaneous luminosity ( $\times 10^{33} \text{ cm}^2 \text{ s}^{-1}$ )	5	13	16	19
Total delivered integrated luminosity ( $\text{fb}^{-1}$ )	4.0	38.5	50.2	63.4

**Table 3.2:** Peak luminosity and total integrated luminosity delivered by the LHC at  $\sqrt{s} = 13 \text{ TeV}$  in Run-2 per year [127].

the inefficiency of the so-called “warm start”: when the stable beam flag is raised, the tracking detectors undergo a ramp of the high-voltage and, for the pixel system, turning on the preamplifiers. The All Good Data Quality criteria require all reconstructed physics objects to be of good data quality [126].

### Cross-section

The cross-section is a metric of the likely is a particular reaction to occur. The higher the cross section is for a process, the more probable is for it to take place. Denoted by  $\sigma$ , it is measured in units of area named barns: 1 barn = b =  $10^{-24} \text{ cm}^2$ . For instance, for the LHC energy:

- $\sigma(pp \rightarrow X) \approx 0.1 \text{ b}$
- $\sigma(pp \rightarrow X + H) \approx 1 \times 10^{-11} \text{ b}$
- $\sigma(pp \rightarrow X + H; H \rightarrow \gamma\gamma) \approx 50 \times 10^{-15} \text{ b}$

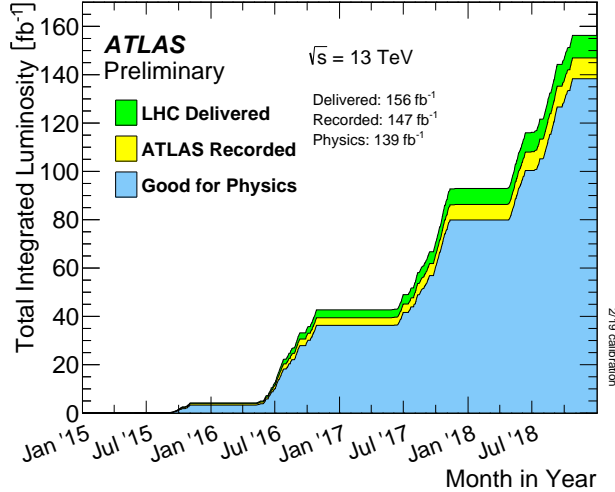
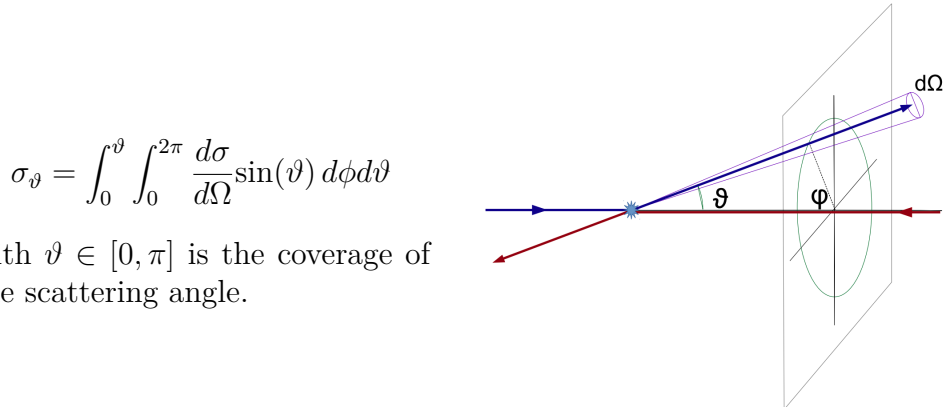


**Figure 3.9:** Total cumulative luminosity versus time delivered to ATLAS (green), recorded by ATLAS (yellow) and certified to be good quality data (blue) during stable beams for  $pp$  collisions at  $\sqrt{s} = 13$  TeV.

In experiments with rotational symmetry, such as ATLAS, it is usual to define the differential cross-section ( $\frac{d\sigma}{d\Omega}$ ) as the cross-section per solid angle. If the differential cross-section is integrated over corresponding the angular range, the cross-section for a specific region ( $\sigma_\vartheta$ ) is obtained:



The total cross-section is determined by the amplitude of the scattering matrix  $\mathcal{M}$ , which is independent of the experimental setup. The  $\mathcal{M}$ , also known as scattering amplitude, relates the initial state and the final state of a physical system undergoing a scattering process. Using  $\mathcal{M}$ , the total cross-section for a process is determined by:

$$\sigma_{tot} = \int \frac{d\sigma}{d\Omega} d\Omega = \int \frac{1}{\Phi} |\mathcal{M}|^2 dQ$$

being  $\Phi$  the incident particle flux in the process and the parameter  $dQ$  describes the kinematic phase space.

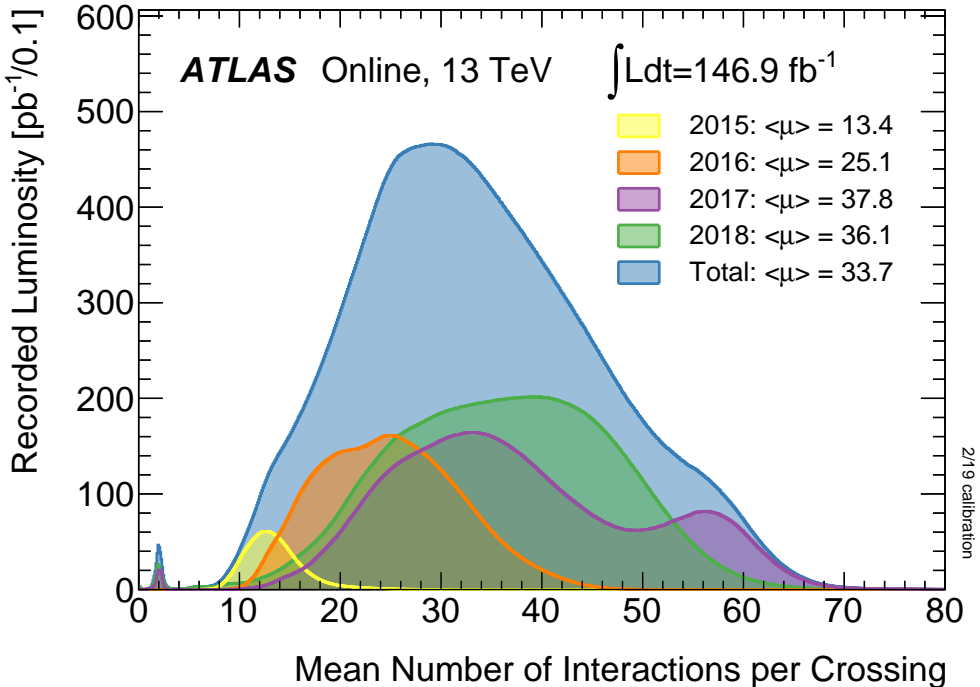


**Figure 3.10:** Luminosity-weighted distribution of the mean number of interactions per crossing  $\langle \mu \rangle$  for Run-2 with  $pp$  collisions data.

### 3.2.6 The Pile-up effect

Pile-up is a challenging matter among detectors and for the acquisition and analysis of the data. In particle physics, pile-up is called to the situation where the detector is being affected by several events at the same time.

Even though the bunches are composed by  $\sim 10^{11}$  protons, there are only around 30 collisions per crossing with nominal beam currents. The mean number of interactions per bunch crossing is presented in Figure 3.10 for each year of Run-2. The data shown in Figure 3.10 is recorded by ATLAS during stable beams at  $\sqrt{s} = 13$  TeV. The mean number of interactions per crossing corresponds to the mean of the poisson distribution of the number of interactions per crossing calculated for each bunch. It is calculated from the instantaneous per bunch luminosity as  $\langle \mu \rangle = \mathcal{L}_{\text{bunch}} \times \sigma_{\text{inel}} / f_r$  where  $\mathcal{L}_{\text{bunch}}$  is the instantaneous luminosity per bunch,  $\sigma_{\text{inel}} = 80$  mb is the inelastic cross section of  $pp$  collisions at 13 TeV and  $f_r = 11.245$  kHz is the LHC revolution frequency.

**Work in progress**

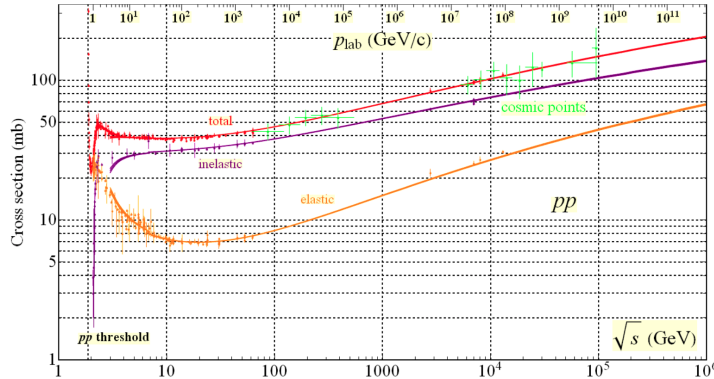


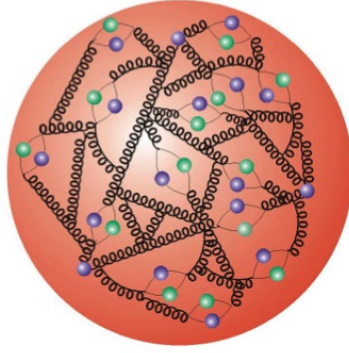
**Figure 3.11:** Total and elastic cross-section for  $pp$  collisions as a function of the laboratory momentum and the  $\sqrt{s}$  [129].

### 3.2.7 Phenomenology of proton-proton collisions

During LHC Run-2 data taking period, the protons were colliding at  $\sqrt{s} = 13$  TeV. The  $pp$  total cross-section at this energy is measured to be  $\sigma_{tot} = (110.6 \pm 3.4)$  mb [128]. The luminosity-independent method used to measure  $\sigma_{tot}$  allows to split the cross-section into elastic and inelastic cross-sections,  $\sigma_{el} = (31.9 \pm 1.7)$  mb and  $\sigma_{inel} = (79.5 \pm 1.8)$  mb respectively. However, only inelastic scattering generates particles with an sufficient angle with respect to the beam axis so that these particles enter into the geometrical acceptance of the detector. Figure 3.11 shows the cross-section (elastic, inelastic and total) for  $pp$  collisions depending on  $\sqrt{s}$  (**Why the values of the Figure 3.11 do not match the:  $\sigma_{tot} = (110.6 \pm 3.4)$ ,  $\sigma_{el} = (31.9 \pm 1.7)$  and  $\sigma_{inel} = (79.5 \pm 1.8)$** ). The shown cross-section can be computed as the convolution of parton density functions (PDFs) with the parton scattering matrix element  $\mathcal{M}$ .

Unlike leptons, protons are composite objects since they are made of quarks and gluons. Therefore and specially at LHC energy regime, the  $pp$  collisions cannot be described as a point-like interactions, here is where the PDFs come into play. The PDFs are functions containing the long distance structure of the hadron in terms of valence and sea quarks and gluons. This description is known as “parton model”.

### 3.2.7.1 Proton structure and parton model for collisions



The parton model for hadrons describes these non-fundamental particles as a composite of a number of point-like constituents named partons. The proton is not only simply made of three quarks ( $uud$ , the so called “valence” quarks) but also, there is a “sea” of gluons and short-lived quark and anti-quark pairs. The partons in the sea are continuously interacting with each other and can have any flavour.

The PDFs describe the distribution of the hadron’s momentum among its constituents. The PDFs are essential to describe the  $p\bar{p}$  interactions because these collisions cannot be understood as point-like particles crashing. Instead, all the constituents of the protons are taken into account [59].

Due to the fact that inside of hadrons the quarks are continuously interacting with each other via the exchange of gluons, it is not possible to calculate PDFs using non-perturbative QCD. Instead, the momentum distribution function of the partons within the proton is obtained by a fit on a large number of cross-section data points over a grid of  $x$  and  $Q^2$  values obtained from many experiments (deep inelastic scattering, Drell-Yan and jet measurements). There are various global fitting collaborations (ABM, CT, MMHT, NNPDF, MSTW, CTEQ), each taking different approaches to this fitting procedure. These fits are later extrapolated to new energy scales.

Formally, the PDF  $f_{a/A}(x, Q^2)$  is defined as the probability of finding a parton  $a$  within the hadron  $A$  carrying a fraction  $x = p_a/p_A$  of its momentum at  $Q^2$  energy scale. The energy scale  $Q$  characterises the hard scattering and typically corresponds to the momentum transfer in the given process. As an example, several PDFs at two different scale energies are presented in Figure 3.12 as a function of  $x$ .

The momentum of the proton is distributed among its constituents and, while at lower energies ( $Q \sim 1$  GeV) it is shared mainly between the valence quarks, at higher energies ( $1 < Q \lesssim 1$  GeV) the emission of gluons carrying a some of the initial momentum of the quark is more probable. Within the QCD theory, these interactions can be classified in two main groups: “hard” and “soft”. The hard processes are those involving large momentum transfer. This type of processes are well understood and their cross-section can be predicted with good precision using perturbation theory. In contrast,

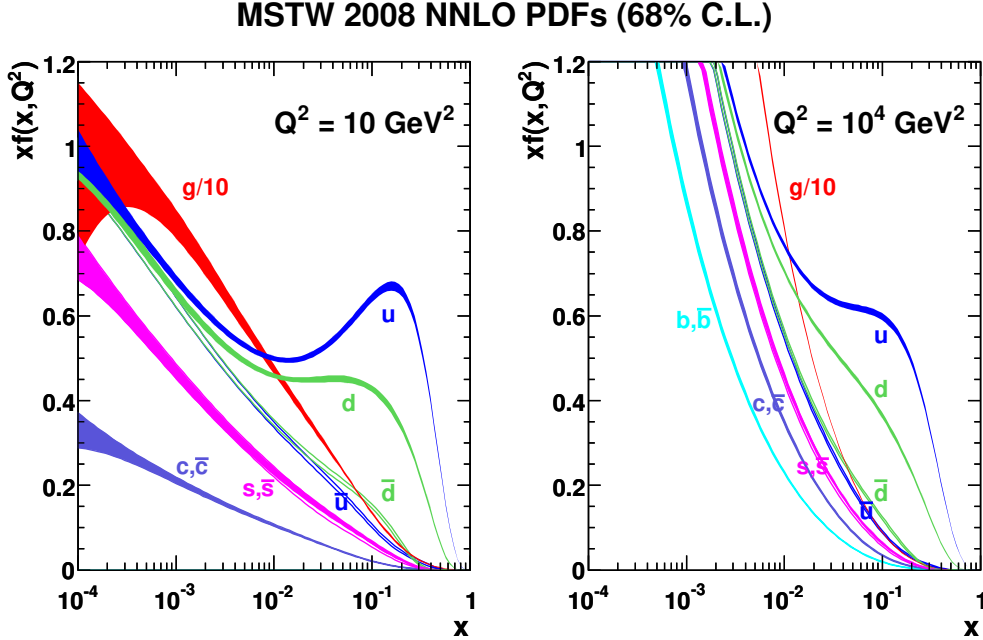


**Figure 3.12:** Parton distribution functions  $xf(x, q^2)$  plotted against  $x$  for gluons different quark flavours at  $Q^2 = 10 \text{ GeV}^2$  and  $Q^2 = 10^4 \text{ GeV}^2$  using MSTW 2008 NNLO [60].

the low momentum transfer of soft interactions leads to a much more dominant impact of non-perturbative QCD, which makes much more difficult to calculate the cross-section.

When two protons ( $A$  and  $B$ ) collide, what actually happens is that the partons of one proton can interact with partons of the other via a hard scattering process. Each of the interactions between the partons pairs (let  $a$  be a parton from  $A$  interacting with  $b$ , a parton from  $B$ ) is independent from the interactions of other partons. The remaining partons also contribute to the final state as “underlying events”.

In a  $pp$  or, more generally, in a hadron-hadron ( $A$  and  $B$ ) hard scattering process, the total cross section is given by:

$$\sigma_{AB \rightarrow X} = \sum_{a,b} \iint dx_a dx_b f_a(x_a, Q^2) f_b(x_b, Q^2) \times \hat{\sigma}_{ab \rightarrow X} \quad (3.9)$$

where  $a$  and  $b$  denote the parton constituents of the hadrons  $A$  and  $B$  respectively and  $f_i(x_i, Q^2)$  their PDF. Here, the  $Q$  is chosen to be the factorisation scale ( $\mu_F$ ). The contribution of the individual partons  $a$  and  $b$  is denoted by  $\hat{\sigma}_{ab \rightarrow X}$ . With this equation, all process in  $pp$  collisions can be computed.

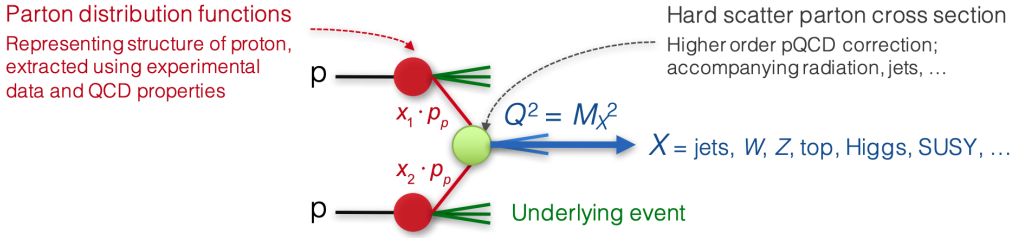


**Figure 3.13:** Simplified view of a  $pp$  collision [124].

Depending on the order achieved in perturbation theory (LO, NLO, NNLO, ...), the cross-section of the individual partons to give the final state of interest ( $ab \rightarrow X$ ) is calculated as

$$\begin{aligned}\hat{\sigma}_{ab \rightarrow X} &= \sum_{i=0}^{\infty} \alpha_s^i(\mu_R) \sigma_n(x_a, x_b, \mu_F^2) \\ &= [\sigma_{LO}(x_a, x_b, \mu_F^2) + \alpha_s(\mu_R) \sigma_{NLO}(x_a, x_b, \mu_F^2) \\ &\quad + \alpha_s(\mu_R)^2 \sigma_{NNLO}(x_a, x_b, \mu_F^2) + \dots]_{ab \rightarrow X}\end{aligned}$$

where  $\alpha_s^i(\mu_R)$  is the coupling constant derived for a specific renormalization scale ( $\mu_R$ ).

### Work in progress

#### 3.2.7.2 Underlying event

## 3.3 ATLAS

Installed in its experimental cavern at point 1, ATLAS is the largest detector ever constructed for a particle collider with its 46 m long and 25 m in diameter. It is designed to record events of high-energy colliding particles at high luminosities. The thousands of millions of interactions that take place at the centre of the ATLAS detector are recorded and processed by the different sub-detectors, which are composed by more than 100 million sensitive electronic channels. Each ATLAS sub-detector is sensible to a different type of particle and to different properties. Therefore, the layered structure allows for effective particle identification, as well as enables accurate measurements of energy and momentum. Figure 3.14 shows an overall layout of the ATLAS detector and identifies its different sub-detectors. In the picture can be appreciated that the cylindrical shape of ATLAS is divided into two parts: the “barrel” (curved parts) and the two “end-caps” (bases). In the barrel region, the sub-detectors are built as coaxial layers around the beam pipe (see memo 3.15). As one moves away from the axis,

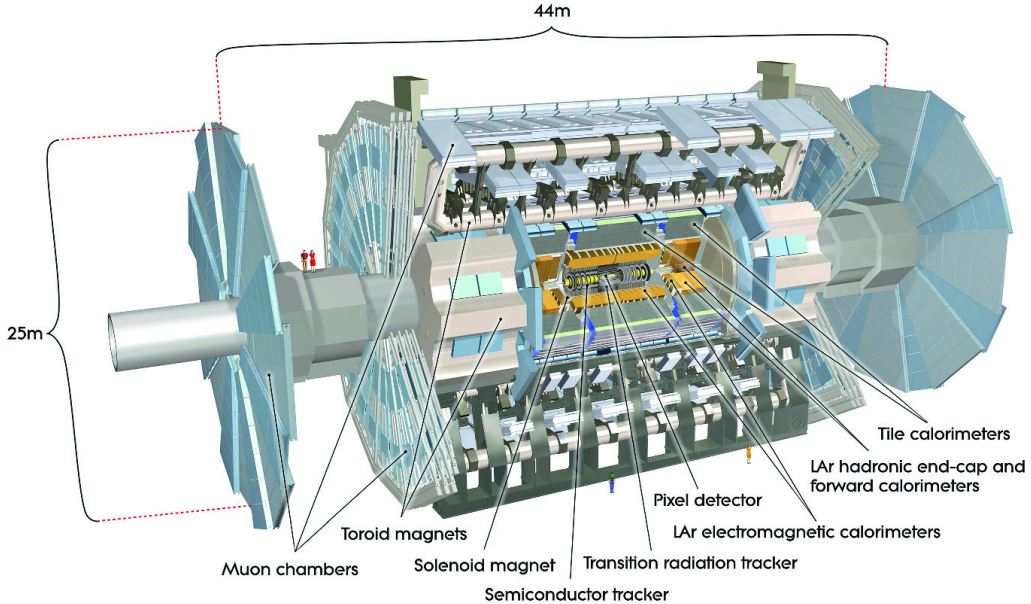


**Figure 3.14:** Simulated schematic view of the ATLAS detector.

it finds the Inner Detector (ID), the solenoid magnet, the Electromagnetic (ECAL) and Hadronic (HCAL) Calorimeters, and the Muon Spectrometer (MS) in the outermost layer. The technical details of these sub-detectors are presented in the coming sections.

ATLAS is able to explore a wide range of phenomena with high precision, including new physics events. Even though it is a general-purpose experiment, it was designed taking into account the Higgs and BSM phenomena searches that were carried out at LHC. This is why, since the mass of the Higgs was not known at that time, its performance requirements cover a large mass range for the Higgs decay products.

One of the most important milestones for ATLAS (and for all science in the last decades) was the observation of a particle consistent with the Higgs boson in July 2012 (see 2.2.1). In 2016, the combination of ATLAS and CMS measurements for Higgs boson production on decay rates with Run-1 data was published [131]. After that, the physics programme at 13 TeV allowed precision studies of the Higgs boson and other SM particles, as well as the search for new particles with other masses.

Other relevant items in ATLAS timeline are the observation and rate measurement of  $t\bar{t}$  events [132] or the evidence for rare electroweak  $W^\pm W^\pm$  production [133]. The first evidence of light-by-light scattering at high energy was also found with ATLAS [134]. The first  $t\bar{t}H$  associate production [135] and  $H \rightarrow b\bar{b}$  decays [136] were observed for first time by ATLAS too.



**Figure 3.15:** Due to its coaxial-layered structure ATLAS can be understood as cylindric onion: “*ATLAS have layers, onions have layers*” [130].

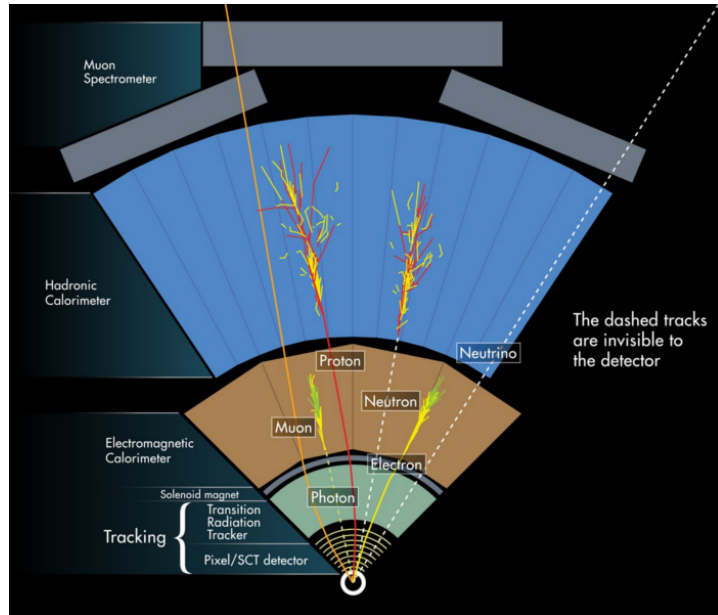


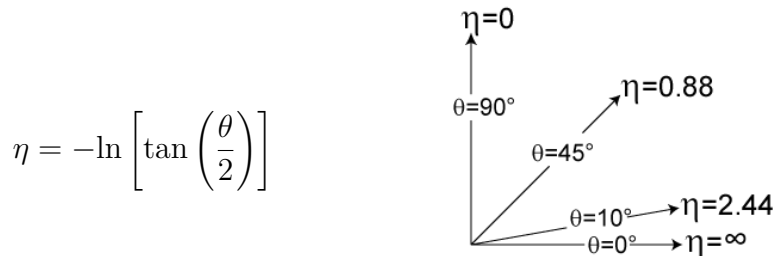
**Figure 3.16:** Fraction of the transversal plane of ATLAS. Each particle leaves a different signature in each layer. By signature is meant the particular distribution of energy deposition. This scheme is fundamental to understand the object reconstruction in the next chapter.

The physics programme of ATLAS include precise measurements of the SM [137], super-symmetry studies [138], sources of  $\mathcal{CP}$ -violation [139], large  $E_T^{\text{miss}}$  dark-matter searches [140], astroparticle physics [141], extra dimensions [142] and others.

ATLAS is not only a detector but also a collaboration of people composed of more than 5000 members including physicists, engineers, technicians, doctoral students and support staff. Working at CERN or at any of the 181 institutions that constitute ATLAS, the different teams work collaboratively to achieve success.

### 3.3.1 Coordinate system

Due to its cylindrical structure, ATLAS uses a right-handed system with its origin at the IP where the collisions take place. On one side, there are the  $(x, y, z)$  Cartesian coordinates. The  $x$ -axis is pointing towards the centre of the ring circumference, the  $y$ -axis is perpendicular to the plane defined by the LHC ring and it points to the surface, and the  $z$ -axis is defined by the direction of the beam. On the other side, it is more frequent to employ the cylindrical coordinates  $(r, \phi, z)$  or the system defined by the azimuthal angle ( $\phi$ ) and the pseudorapidity ( $\eta$ ):



where  $\theta$  is the polar angle<sup>3</sup>. As the polar angle approaches zero, pseudorapidity tends towards infinity. The change in pseudorapidity  $\Delta\eta$  is Lorentz invariant under boosts along the beam axis. The use of  $\eta$  is preferred over  $\theta$  because the distribution of events typically looks flat with respect to  $\eta$ . In terms of the momentum, the above equation can be expressed as:

$$\eta = -\ln \left( \frac{|\vec{p}| + p_z}{|\vec{p}| - p_z} \right)$$

being  $p_z$  the momentum along the beam direction. The rapidity is used when dealing with massive particles and it can be expressed as  $y = \frac{1}{2}\log[(E + p_z)(E - p_z)]$ , being  $E$  the energy projection of the momentum in the  $z$ -axis.

---

<sup>3</sup>Defined as the angle between the particle three-momentum,  $\vec{p}$  and the positive direction of the beam axis.

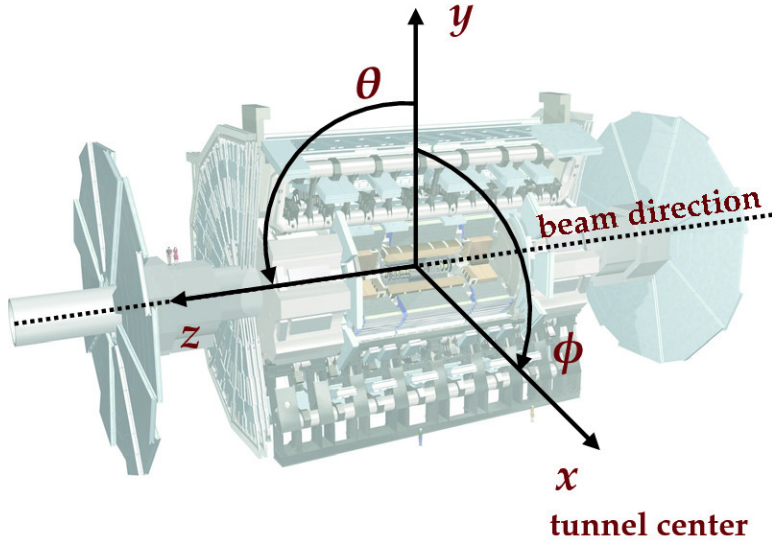


**Figure 3.17:** Coordinate system of the ATLAS detector.

Note that when the particles approach the speed of light, they are in the limit  $E \approx |\vec{p}|$  and the values for rapidity and pseudorapidity converge. The angular distance is measured in units of  $\Delta R = \sqrt{(\Delta\eta)^2 + (\Delta\phi)^2}$ , which is invariant under a boost along the  $z$ -axis<sup>4</sup>. Figure 3.17 shows the coordinate system of ATLAS for both Cartesian and cylindrical coordinates.

The transverse magnitudes such as the transverse momentum ( $p_T$ ) and transverse energy ( $E_T$ ) are defined in the  $x$ - $y$  plane. Knowing the  $p_T$ , and the  $\eta$  and  $\phi$  angles, the cartesian momentum ( $p_x, p_y, p_z$ ) can be derived from:

$$\begin{aligned} p_x &= p_T \cos(\phi) & p_y &= p_T \sin(\phi) \\ p_z &= p_T \sinh(\phi) & |\vec{p}| &= p_T \cosh(\phi) \end{aligned}$$

### 3.3.2 Inner Detector

The ATLAS ID [143][144][109] is the closest sub-detector to the beam pipe. Its layout is shown in Figures 3.18 and 3.19. The charged particles follow a curved trajectory inside the ID due to the magnetic field of the ATLAS bending magnet (see 3.3.5). The different pieces that comprise the ID can reconstruct the traces of these particles with great accuracy allowing, thus, to measure its momentum (this is done using the sagitta method described in Section 5.1.1). For particles coming from the IP, the geometric acceptance of the ID is  $|\eta| < 2.5$  for pseudorapidity and full  $\phi$  coverage in the azimuthal angle. The ID provides  $p_T$  resolution of  $\sigma_{p_T}/p_T = 0.05\%$  GeV

<sup>4</sup> $\Delta\eta = \eta_2 - \eta_1$  and  $\Delta\phi = \phi_2 - \phi_1$ .

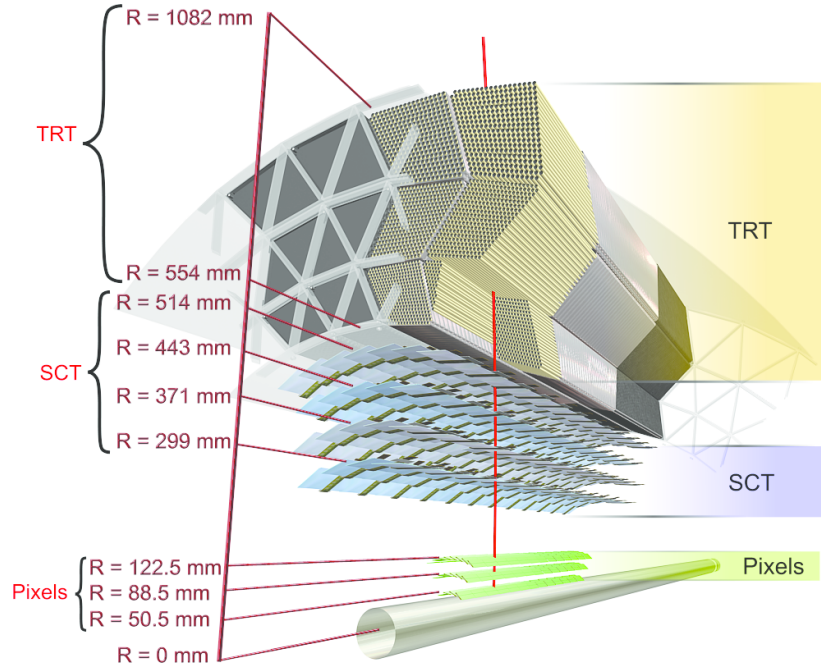


**Figure 3.18:** Barrel part of ID of the ATLAS experiment with the Pixel, SCT and TRT sub-detectors. The IBL is not shown here.

$\pm 1\%$  and a transverse impact parameter resolution<sup>5</sup> of  $10 \mu\text{m}$  for particles in the central  $\eta$  region. It is designed to provide excellent momentum resolution, pattern recognition and measurements of both primary and secondary vertex for charged particles above the  $p_T$  threshold (nominally  $0.5 \text{ GeV}$ ).

The ID is composed of four complementary sub-detectors: The Insertable B-Layer (IBL), the Pixel Detector, the Semiconductor Tracker (SCT) and the Transition Radiation Tracker (TRT). In the sections that follow, a description of each sub-system is provided.

Depending on the  $\eta$  that a particle has, it will interact with some elements of the detector. Figure 3.19 shows the end-cap elements transversed by two charged particles with  $\eta = 2.2$  and  $1.4$ . The track with  $\eta = 1.4$  traverses first the beryllium beam-pipe, then the three cylindrical silicon pixels and the four disks with double layers of the SCT. Finally, this particle travels across approximately 40 tubes in the TRT wheels. In contrast, the particle with  $\eta = 2.2$  encounter the first of the cylindrical silicon-pixel layers after leaving the beryllium pipe. Then, the two end-cap pixel disks and the four last disks of the end-cap SCT.

<sup>5</sup>The impact parameter determine the distance of a reconstructed track from a charged particle to the perigee (the closest point of the track to the global  $z$ -axis)

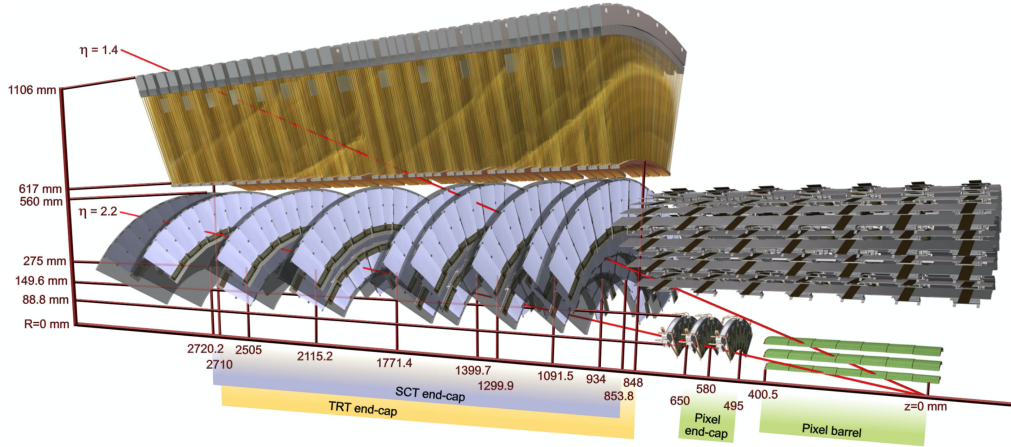


**Figure 3.19:** End-cap of the ID.

### Silicon semiconductors

When a charged particle traverses a doped silicon semiconductor, it creates a pair electron-hole by ionisation. An electric field is applied to the active part of the detector module so that the electron drifts in opposite direction of the electric field and the hole in the field direction. Then, both charges are collected by the p-n junctions. The silicon sensors can be shaped either as pixels, providing precise 2D space point, or as strips, giving a single dimension positioning. On the order of  $10^5$  electron-hole pairs are liberated when a particle crosses the silicon wafer and, with appropriate electronics, a clear signal is obtained in the pixel or strip in which the charged was collected.

#### 3.3.2.1 Insertable B-Layer

The IBL [145] is the innermost component of the ID. It is located between the beam pipe and the pixel detector. Added after Run-1, it provides the closest-to-IP measurements. This improves the robustness and performance of the ATLAS tracking system. It plays a fundamental role for *b*-tagging efficiency because this tagging relies on precise vertex reconstruction. The IBL provides redundancy in the measurements of tracks in order to control the fake rate arising from random combinations of clusters in events with a high pile-up background.

With a hit resolution of  $8\ \mu\text{m}$  in  $r\text{-}\phi$  and  $40\ \mu\text{m}$  along  $z$ , the IBL covers the  $|\eta| < 2.7$  and the entire  $\phi$  range.

The barrel structure of the IBL has a radius of 3.2 cm and is composed by 14 carbon fibre staves as it is shown in Figure 3.20. Each stave has

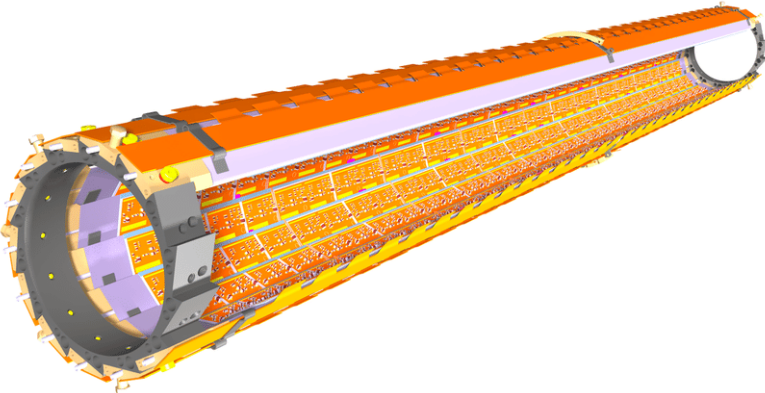


**Figure 3.20:** Schematic drawing of the ATLAS IBL Detector [145].

incorporated cooling  $\text{CO}_2$  circuits, has 32 or 16 modules and uses two types of photodetectors: ATLAS pixel planar sensors and 3D pixel sensors. The used pixels have a size of  $50 \times 400 \mu\text{m}^2$ . Due to the high luminosity of the LHC, the IBL is built with radiation-tolerant sensors.

### 3.3.2.2 Pixel Detector

The ATLAS Pixel Detector [146] consists of a strip detector in the outermost layers and a pixel detector in the region which is closer to the IBL. Along with the IBL, it aims to reconstruct the trajectories of the particles traversing it. It provides a full coverage of the azimuthal angle  $\phi$  and a pseudorapidity range of  $|\eta| < 2.5$  as well as a resolution of  $10 \mu\text{m}$  in  $r\text{-}\phi$  and  $115 \mu\text{m}$  in the  $z$ .

The Pixel Detector and the IBL combined contain  $92 \times 10^6$  pixels with its respective electronic channels, which cover an area of approximately  $1.9 \text{ m}^2$  of silicon consuming  $15 \text{ kW}$ . The barrel region consists of four concentric layers equipped with 1736 sensor modules and each of the two end-caps has three disks with 2888 modules [147]. Figure 3.22 shows the assembly view and cross section of a module of the ATLAS ID Pixel Detector. Each of these modules consists on a silicon pixel sensor bonded to the front-end electronic chips.

Hits in a pixel are read out if the signal exceeds a tunable threshold. The pulse height is measured using the Time-over-Threshold (ToT) technique.

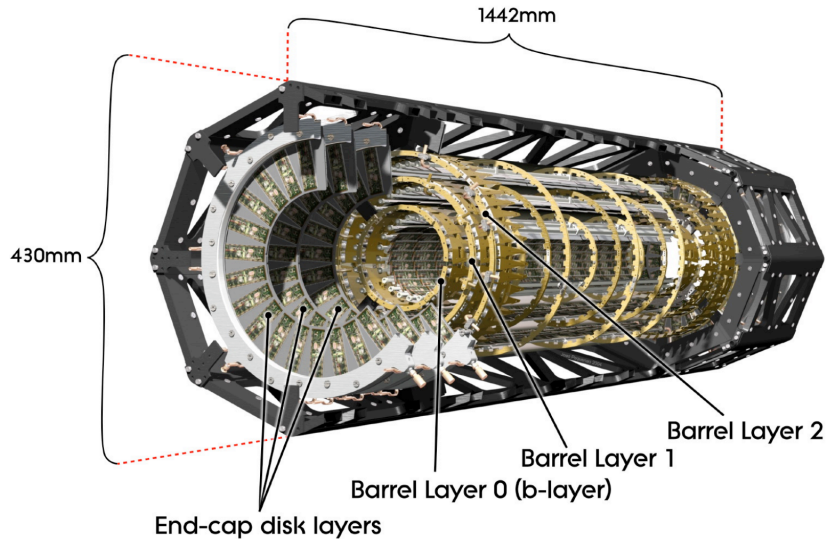


**Figure 3.21:** Schematic view of the ATLAS pixel detector consisting of individual barrel and end-cap layers [109].

### 3.3.2.3 Semiconductor Tracker

The SCT consists of 4088 modules tiling four coaxial cylindrical layers in the barrel region and two end-caps each containing nine disk layers, all of this surrounding the Pixel Detector and providing additional precision tracking. The main difference with the Pixel Detector is that the SCT uses microstrip sensor technology, which is very similar to that of a pixel but being much larger (6 cm). The reason to use microstrips instead of pixels is that the strips are more cost-effective than traditional pixels and a good spatial resolution can be obtained as well if the strips are arranged with an angular offset. Therefore, each SCT detector unit consists on two back-to-back silicon-microstrip planes with a relative angle of 40 mrad. Eight strip layers (i.e. four space points) are crossed by each track in the SCT providing valuable tracking information with resolution of  $17\text{ }\mu\text{m}$  in  $r\text{-}\phi$  and  $580\text{ }\mu\text{m}$  in the  $z$  coordinate. The SCT covers the entire  $\phi$  range and up to 2.5 in  $\eta$ .

Figure 3.23 shows an exploded view of the different components of an SCT module, including the high thermal conductivity spine, the polyimide hybrids and readout chips.

### 3.3.2.4 Transition Radiation Tracker

The TRT is used in conjunction with the Pixel Detector and silicon micro strip (SCT) to extend the  $\eta$  range in which the tracks can be reconstructed to  $|\eta| = 2$ . This part of the ID is formed by a large number of 4 mm straw tubes

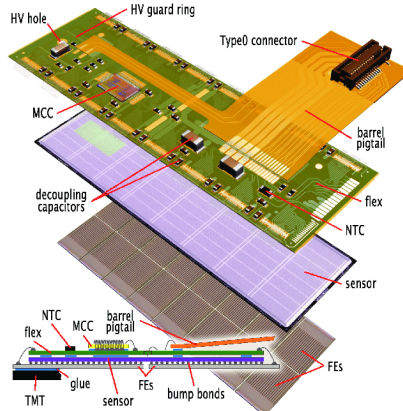


**Figure 3.22:** Pixel Detector module [146].

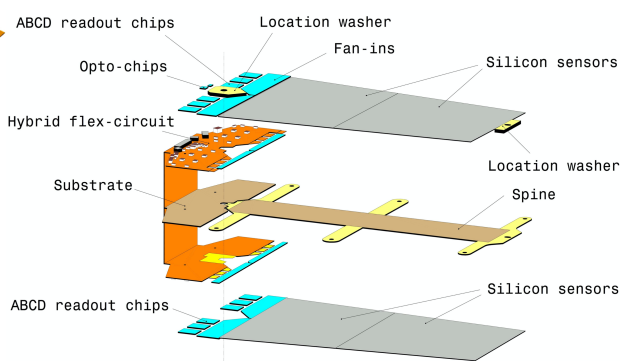


**Figure 3.23:** SCT detector module [109].

filled with gas. This part of the ID relies both on the collection of primary ionisation charge and the collection of secondary ionisation charge arising from the transition radiation to measure the track of charged particles. The tube surface functions as a cathode while the wire in the center as a cathode. When a charged particle passes through the gas in the tube, it ionises the gas and the freed electrons drift towards the anode, generating an electrical current. This detector provides a single hit resolution of  $170\ \mu\text{m}$  in  $r\text{-}\phi$  but does not have sensitivity in  $z$ . The TRT also provides discrimination between electrons and pions since the latter generate a much smaller signal than the former. When the electrons pass, they produce x-ray photons that lead to strong avalanches within the tubes and, thus, a great signal.

### 3.3.3 Calorimeters

After the ID, the next layer of detectors in ATLAS correspond to the calorimeters (Figure 3.24) [148]. Their purpose is to measure the energy of the particles (neutral or charged), as well as to help to reconstruct the path followed by them. Most particles initiate a shower (Section 3.3.3.1) when they enter into the calorimeter. Part of the energy of these particles is deposited in the device, then collected and measured by it. Most of calorimeters in particle physics are segmented transversely to provide information about the direction of the particles. Based on how the particle shower develops, the longitudinal segmentation can provide information for identifying the particle (a more detailed discussion of how particles are reconstructed within the ATLAS detector is presented in Section ??).

In general, calorimeters can be classified as sampling, when are made of two types of materials, or homogeneous, built with just one type of material.

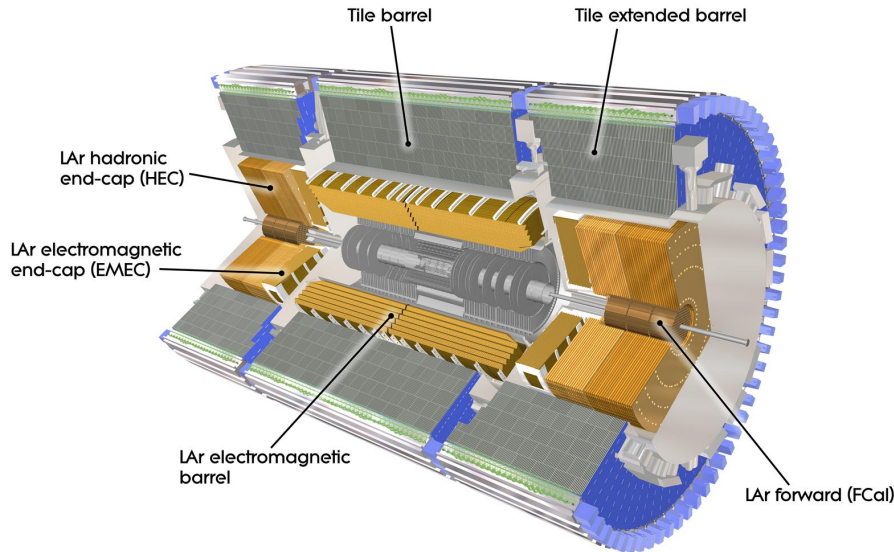


**Figure 3.24:** Computer generated image of the ATLAS calorimeter [147].

ATLAS uses sampling calorimeters, which consist of alternating layers of different materials:

- **Passive material:** Also known as absorber, it is a denser material to fully stop the traversing particles. When a particle interacts with the passive material it produces the shower (Figures 3.25 and 3.26). For the absorber layers in ATLAS, lead is used for the ECAL and steel for the HCAL.
- **Active material:** This material detects the particles from the shower originated in the absorber. The liquid Argon (LAr) is used as active material for ECAL and plastic scintillator for HCAL.

In the homogeneous calorimeters, the material used combines the features of an absorber and a detector, performing both tasks.

Since each type of particle interacts differently, there are two main types of calorimeters: the electromagnetic calorimeter (ECAL), which measures the energy of electrons/positrons and photons, and the hadronic calorimeters (HCAL), which registers the energy of the strongly-interacting particles. Both classes are covered in the next sections.

### Scintillator

The particles from the shower leave some of the molecules of the plastic

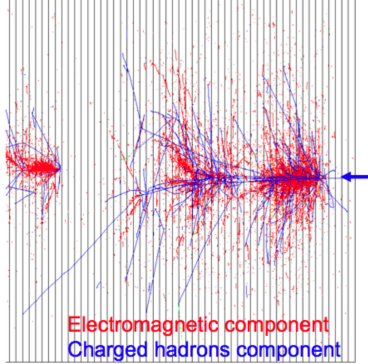


**Figure 3.25:** EM and hadronic cascades.

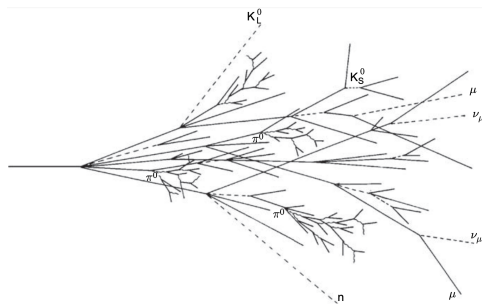


**Figure 3.26:** Sketch of a hadronic cascade [149].

scintillator in an excited state. The subsequent decay of these molecules produces the emission of photons in the ultraviolet energy region. This light is collected by photomultiplier tubes at the edge of the tiles and converted into a current pulse whose amplitude is proportional to the energy deposited by transversing particle.

### 3.3.3.1 Particle showering

A particle shower is a cascade of secondary particles produced when a high-energy particle interacts with matter. The first particle interacts with the passive material producing a secondary particle with less energy than the first one. The second particle does the same and, in each step, the particles produced are less and less energetic. For a single incoming particle, this iterative process can continue for thousands of periods [149]. An illustration of the EM and hadronic particle cascades is shown in Figure 3.25.

#### Electromagnetic shower

The electromagnetic (EM) shower is initiated by a  $e^-$ ,  $e^+$  or  $\gamma$ , these three particles are the sole components of this type of shower. At energies higher than 100 MeV, the EM showering is based on two main processes: Bremsstrahlung and pair creation. The electrons lose their energy almost exclusively by bremsstrahlung radiation, a process in which the lepton radiates thousands of soft photons because of its interaction with another charged particle. The photons lose their energy by the production of an  $e^- - e^+$  pair. At lower energy scales, other processes contribute. In the MeV

range, the Compton scattering<sup>6</sup> and photoelectric effect<sup>7</sup> are the dominant interactions for energy loss for photons, while the ionisation and excitation are for the charged particles ( $e^-$  and  $e^+$ ).

### Hadronic shower

When a hadron interacts with the passive material, this shower is initialised. Both strong and EM interactions are involved in the development of this type of shower and they present a larger variety of particle components. Therefore, the hadronic showers are significantly more complex than the EM. Figure 3.26 shows the processes leading to a hadronic cascade.

The production of neutral pions represents about a third of the energy loss of hadronic interactions. These pions decay 98.8% of times to two photons [150] that are starting the EM showers. The rest of hadronic interactions consist of the production of charged mesons, nuclear fragments and protons, soft neutrons and photons or unpredictable loss through undetectable processes.

#### 3.3.3.2 Electromagnetic calorimeter

The ECAL [148] absorbs the energy of the  $e^-$ ,  $e^+$  or a  $\gamma$  covering a pseudorapidity range of  $|\eta| < 1.475$  in the barrel. It is made of a lead absorber and LAr detector following an accordion shape, as can be seen in Figure 3.27a, where the different layers are clearly visible. The shower originated at the absorber layer ionise the LAr producing a measurable current proportional to the energy of the original particle. The LAr layer operates at 87 K.

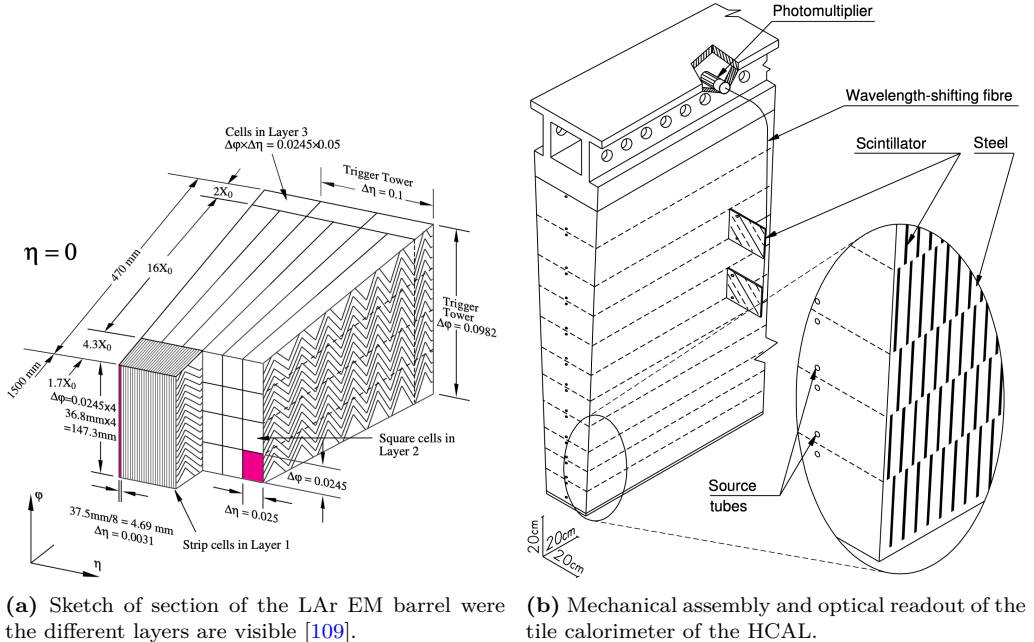
The barrel part is split into two identical half-barrels separated by a small gap at  $z = 0$ . Each end-cap calorimeter is composed of two coaxial wheels that cover  $|\eta| < 1.475$ .

The total amount of material in the ECAL corresponds to 25-35 radiation lengths,  $X_0$ , and 2-4 nuclear interaction lengths,  $\lambda$ , over the entire  $\eta$  range. Characteristic of each material, the ration length is the mean distance over which a high-energy electron lose all but  $1/e$  of its energy by bremsstrahlung. The radiation length is the mean free path between interactions required to reduce the number of relativistic charged particles by the factor  $1/e = 0.37$  as they pass through matter.

---

<sup>6</sup>Scattering of a photon after interacting with a charged particle, usually an electron.

<sup>7</sup>Emission of photoelectrons when the EM radiation interacts with matter.



(a) Sketch of section of the LAr EM barrel were the different layers are visible [109]. (b) Mechanical assembly and optical readout of the tile calorimeter of the HCAL.

**Figure 3.27:** Sketch of a section of the ATLAS (a) ECAL and (b) HCAL [109].

The energy resolution of a calorimeter can be parametrised as:

$$\frac{\sigma_E}{E} = \frac{a}{\sqrt{e}} \oplus \frac{b}{E} \oplus c = \frac{10\%}{\sqrt{e}} \oplus \frac{170 \text{ MeV}}{E} \oplus 0.7\%$$

Where  $a$  is the stochastic term,  $b$  the electronic noise and  $c$  a constant that includes detector instabilities and increases with  $E$  [151].

### 3.3.3.3 Hadronic calorimeter

The ATLAS HCAL [148] is made of a sampling calorimeter of steel and plastic scintillator tiles covering the pseudorapidity region of  $|\eta| < 1.7$  in the barrels. The end-caps are made of copper and LAr, covering  $1.5 < |\eta| < 3.2$ , and are emended in the end-caps of the ECAL. This calorimeter uses 9800 electronic channels in the barrel and 5600 in the end-cap. With 2900 tones, the HCAL is the heaviest part of the ATLAS detector. It has 420000 scintillator tiles and 9500 photomultiplier tubes [147]. All these elements are shown in Figure 3.27b, where the tiles, the fibres and the photomultipliers are visible.

The contribution of the electronic noise is negligible, therefore, the energy resolution for the tile calorimeter is [148]:

$$\frac{\sigma_E}{E} = \frac{5.9\%}{\sqrt{e}} \oplus 5.7\%$$

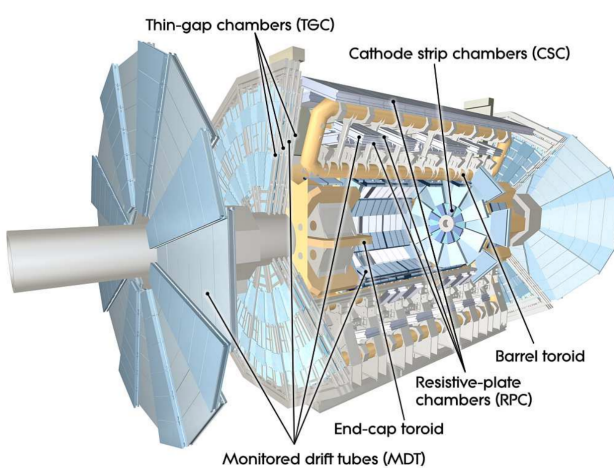


**Figure 3.28:** Conceptual layout of the MS (blue). The magnet system (yellow) is also shown [109].

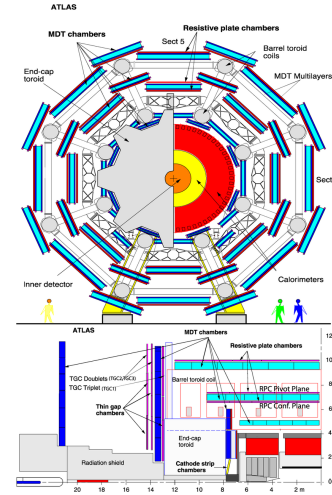


**Figure 3.29:** ATLAS Muon detectors.

### 3.3.3.4 Forward calorimeter

In addition to the ECAL and HCAL, a smaller calorimeter is placed in the end-caps surrounding the beam pipe in order to cover the forward region ( $3.1 < |\eta| < 4.9$ ), the forward calorimeter (FCAL). This coverage is required for many physics tasks such as the reconstruction of the  $E_T^{\text{miss}}$  of the forward-jet tagging.

This calorimeter is a sampling calorimeter based on LAr as active medium and copper as absorber. The thickness of the FCAL is optimised to achieve high absorption, approximately,  $10 X_0$  [151].

This detector has a resolution of:

$$\frac{\sigma_E}{E} = \frac{100\%}{\sqrt{e}} \oplus 10\%$$

### 3.3.4 Muon Spectrometer

The muons can penetrate through calorimeters and reach the last layer of the ATLAS detector, the MS [152]. Figure 3.28 shows a schematic cut-away view of the ATLAS muon system.

The MS surrounds the calorimeters and its aim is to measure the trajectories of muons to determine their direction and momentum with excellent tracking precision as well as their electric charge in a pseudorapidity coverage of  $|\eta| < 2.7$ . To bend the particle tracks after they exit the HCAL, the MS uses eight large superconducting air-core toroid magnets in  $|\eta| < 1.4$

Type	Purpose	Location	Coverage
MDT	Tracking	Barrel + end-cap	$0.0 <  \eta  < 2.7$
CSC	Tracking	End-cap layer 1	$2.0 <  \eta  < 2.7$
RPC	Trigger	Barrel	$0.0 <  \eta  < 1.0$
TGC	Trigger	End-cap	$1.0 <  \eta  < 2.4$

**Table 3.3:** ATLAS MS sub-detectors [153].

region. For the  $1.6 < |\eta| < 2.7$ , the tracks are bent by magnets inserted in the end-caps. In the transition region,  $1.4 < |\eta| < 1.6$ , the magnetic field responsible of bending the particles is provided by both the air-core toroid magnets and the smaller end-cap magnets. These fields are perpendicular to the trajectory of the muons originated in the IP. More details about the magnet systems of the MS can be found in Section 3.3.5.

The MS instrumentation is based, on one hand, on precision chambers for the coordinate measurements in the bending plane: Monitored Drift Tube chambers (MDT) and Cathode-Strip Chambers (CSC), and, on the other hand, on trigger chambers: Resistive Plate Chambers (RPC) and Thin Gap Chambers (TGC). Table 3.3 gives a summary of the MS detector components. In Figure 3.29 the distribution of the MS detectors is described.

- **Monitored Drift Tube chambers (MDTs)** [154]: The MDT chambers provide precise momentum measurements by determining with high accuracy the curve of the tracks. This part of the MS cover a pseudorapidity range of  $|\eta| < 2$ . The MDTs are designed to have stand-alone measurement capability in order to safeguard against any unanticipated background and to ensure good discovery potential in the scenario of unexpected topologies. In the barrel region, the MDTs are arranged in three cylindrical stations coaxial to the beam axis and in the end-cap, the MDTs are vertically installed in three layers. An MTD chamber consists of six layers of drift tubes (as depicted in Figure 3.30), each of them with 3 cm of diameter, filled with gas. A tube can achieve a single wire resolution of 80  $\mu\text{m}$  [153]. In the entire MDT system, there are 1 171 chambers with a total of 354 240 tubes.
- **Cathode-Strip Chambers (CSC)**: It is the innermost tracking layer of the MS. Due to its higher rate capability and time resolution, it is located close to the beam axis, where the particle fluxes are higher. This component of the muon detector system covers the  $\eta$  range  $2.0 < |\eta| < 2.7$ . It measures with precision the coordinates at

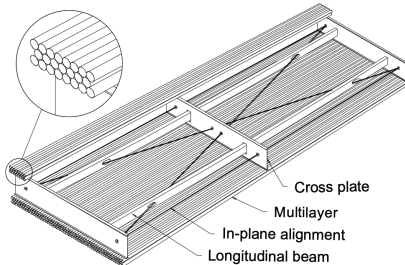


**Figure 3.30:** Schematic view of an MDT chamber.

the ends of the detector. With its 70 000 electric channel, provides a resolution around 60  $\mu\text{m}$ .

- **Resistive Plate Chambers (RPC)** [155]: This is the barrel element of the trigger system. These chambers are located on both sides of the central CSC and inside the outermost CSC station. The RPCs are gaseous detectors used for triggering and for measuring the second coordinate in the barrel region. RCPs provide a time-space resolution of 1 cm  $\times$  1 ns. The gas gap is of the order of 2 mm and the plate external surfaces are coated by thin layers of graphite painting. This part of the MS is composed of 3 800 electric channels.
- **Thin Gap Chambers (TGC)** [156]: As a first-level trigger, they have to provide high efficiency and excellent time resolution for bunch-crossing tagging in a high-background environment. The particle flux received by the TCG is higher than that of the RPC. The three TGCs are located near the middle end-cap MDT station, in the forward regions. TGCs measure the second coordinate in the non-bending direction with its circa 440 000 electrical channels.

### 3.3.5 Magnet system

The curvature in the track of the particles is fundamental to measure the transverse momentum and the charge of the particles. To bend the path of charged particles, these are immersed in a homogeneous magnetic field which is produced by the both the toroidal and solenoid magnets. The bending power is proportional to  $\int B dl$ , where  $B$  is the magnetic field component orthogonal to the charged direction.

ATLAS magnetic system is divided into three subsystems: the central solenoid magnet, the barrel toroids (BT) and the end-cap toroid (ECT).

### 3.3.5.1 Central solenoid magnet

The ATLAS solenoid surrounds the ID providing a 2 T magnetic field at the centre of the tracking volume. This magnet is very thin, having only 4.5 cm thickness, which minimises the interaction of the particles with the magnet material. It is important to not use a lot of material here because, otherwise, the interaction of the particles with the solenoid magnet would impact negatively in the performance of the calorimeters. To achieve such a field within a small thickness, 9 km of niobium-titanium superconductor wires are strengthened, pure aluminium strips and cooled down to 4.5 K are used. The central solenoid magnet has a cylindrical shape with a diameter of 5.6 m and a length of 2.56 m, and it weights 5 tonnes.

### 3.3.5.2 Toroid magnets

Three large air-core toroids (one barrel and two end-caps) generate the magnetic field in the MS. Each toroid consists of eight coils assembled with cylindrical symmetry (see the yellow elements in Figure 3.28). The coils are based on an aluminium stabilised Niobium-Titanium alloy (Al/NbTi/Cu) superconductor operating at 4.5 K. The main difference between the barrel and end-cap toroids for the cold mass is that the latter has a higher critical current and less aluminium than the former [157].

#### Barrel Toroid

The Barrel Toroid magnet is the largest component of the ATLAS magnet system. It generates a toroidal magnetic field which, as introduced in Section 3.3.4, is almost completely perpendicular to the track of the particles. In order to minimise the impact (i.e. reduce any interaction apart from applying magnetic field) of the magnet system with the particles, the barrel toroid is designed as an open and light structure. The barrel toroid coils are housed in eight individual cryostats, with the linking elements between them providing the overall mechanical stability. A view of the coils of the barrel toroid in their cryostats is in Figure 3.31.

The magnetic flux density delivered by this magnet is 3.9 T on the superconductor. For the toroid barrel, the bending power ( $\int B dl$ ) is in the interval 1.5 Tm to 5.5 Tm in  $0 < |\eta| < 1.4$ . It is the largest toroidal magnet ever built (25.3 m in length), being probably the most iconic and characteristic element of ATLAS. It weights 830 tonnes and uses more than 56 km of superconducting wire [147].

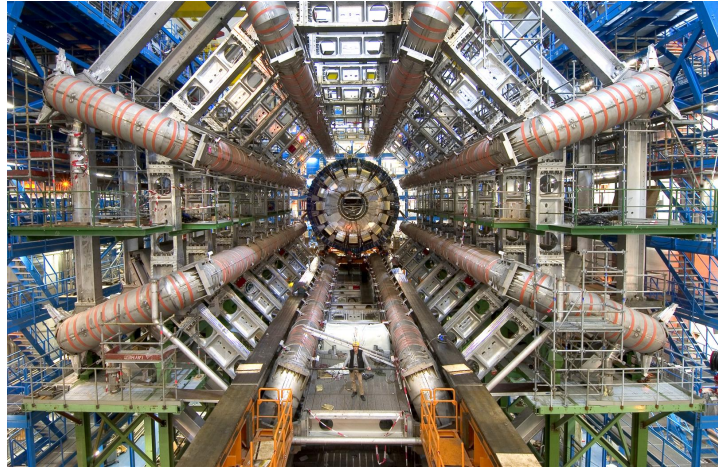


**Figure 3.31:** Very cool picture of the installation ATLAS calorimeters. The eight coils that compose the ATLAS barrel toroid magnets are already installed in the cryostats. Thus view is one of the most iconic of the ATLAS detector.

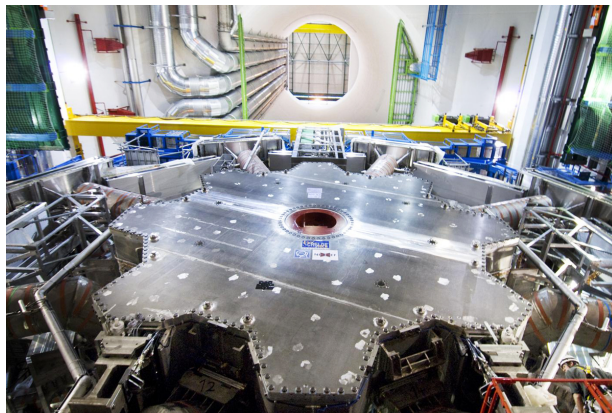


**Figure 3.32:** One of the two end-cap toroidal magnets. Each is made by eight superconducting coils with a magnetic field peaking at 4.1 T.

### End-cap Toroid

The end-caps extend the magnetic field of the barrel toroid to the beam pipe. These magnets are constrained by the inner radius of the barrel toroid and the axial length of the experiment.

As well as in the barrel toroid, it has a 4.1 T magnetic field on the superconductor. For the end-cap toroid, the  $\int B dl \in [4, 8]$  Tm in the pseudorapidity range  $1.6 < |\eta| < 2.7$  [157]. In the transition region where the end-cap and barrel toroids overlap ( $1.4 < |\eta| < 1.6$ ), the bending power is lower. Each end-cap magnet (Figure 3.32) has a diameter 10.7 m and weights 240 tonnes [147].

### 3.3.6 Trigger and Data Acquisition System

The proton bunches cross at the center of the ATLAS detector 40 million times per second, resulting in approximately (using Run-2 mean pile-up  $\langle\mu\rangle = 33.7$ ) 1 200 million proton collisions per second. Reading out and storing all the information from this interactions is not feasible since it has a combined data volume of more than 60 million megabytes per second. Only some of these events are of interest to physics studies and, consequently, only this subset need to be saved into permanent storage for later analysis. In order to select only interesting data, ATLAS uses a complex and highly distributed Trigger and Data Acquisition System (TDAQ) [158] that reduces the rate of recorded data from the initial 1 200 MHz of interactions to just an average of 1 kHz. The reduction through the trigger is carried in two steps: The electronic performs an initial selection and, afterwards, a large computer farm analyses the data that pass the initial filter.

The TDAQ system is an essential component of ATLAS in charge of processing the events online, selecting the relevant ones and storing them. To do so, the TDAQ verifies for each bunch crossing if at least one among the hundred conditions is satisfied. These conditions, also known as “triggers”, are based on identifying both combinations of candidate physics objects (“signatures”) and global properties of the events [159]. Figure 3.33 shows a diagram of the TDAQ system, in this figure can be seen the different components as well as the detector read-out and data flow.

The first-level trigger (LVL1) is a hardware-based filter performed by ATLAS sub-detectors. The LVL1 uses the information of the Calorimeters and the MS to select events up to the maximum-readout rate of the detector (100 kHz) within a latency of  $2.5\ \mu\text{s}$ . Additionally, the LVL1 identify the regions of interest (RoI), which includes the position and the  $p_{\text{T}}$  of the candidate objects.

For each event accepted by the LVL1, the Front-End (FE) detector electronics read the detectors data and pass it to the ReadOut Drivers (ROD). The ROD performs the initial processing and formatting and the ReadOut Systems (ROS) buffers this data.

The data from the different sub-detectors is sent from the ROS to the software-based trigger, the so called “High Level Trigger” (HLT), when is requested by the HLT. This system is comprised by the second-level trigger (LVL2) and the Event Filter (EF or third-level), both made of several farms of computers (about 40 000 CPU cores) interconnected by Ethernet networks. Using modest computing power, LVL2 provides high rejection power with fast and limited precision algorithms. With higher computing power, the EF features lower rejection power with slower but higher preci-

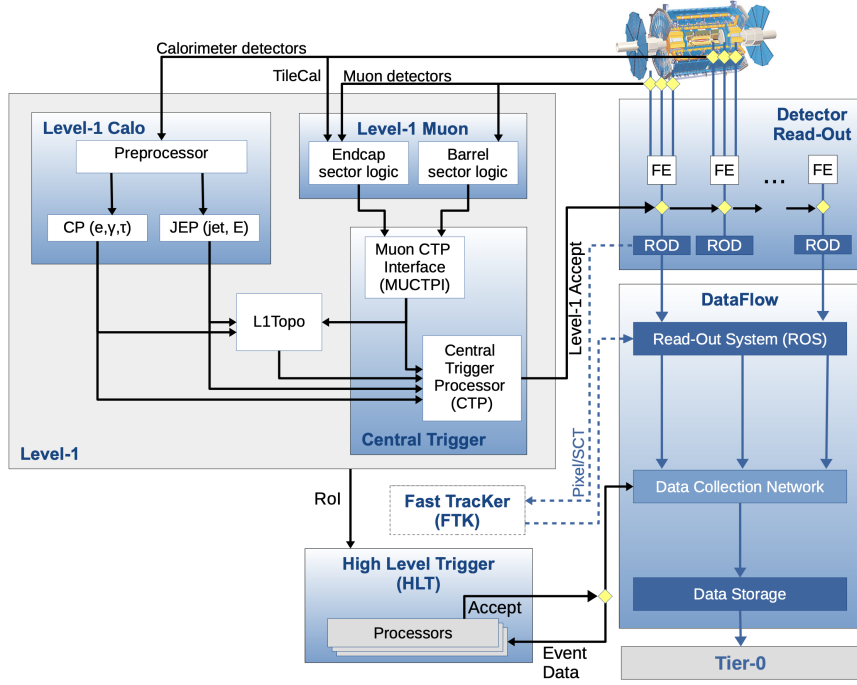


**Figure 3.33:** The ATLAS TDAQ system in Run-2.

sion algorithms [158]. This combination is a cost-effective and flexible way of implementing the HLT. The ID, which was not used by the LVL1, is of key importance for the HLT because on, one hand, the LVL2 reconstruction algorithms are specifically designed to meet strict timing requirements and, on the other hand, the track reconstruction on the EF is less time constrained. This is done by the ID's Fast TracKer (FTK) as the Figure 3.33 shows.

An average 1.2 kHz output rare for Run-2 pass the HLT (with a latency of just  $200\ \mu\text{s}$ ) and is sent by the Sub-Farm Output (SFO) to the Tier-0 facilities for permanent storage and later offline physics analysis. It is important to highlight that the decisions performed by trigger about whether or not to store an event are irrevocable. If an event does not pass the trigger requirements, it is not stored.

### 3.4 Alignment of the inner detector

A fundamental part for the correct operation of the ATLAS detector is its alignment [160]. The goal of the detector alignment is to determine the detector geometry as accurately as possible in order to correct the effects of the time-dependent displacements. In this section, the need of an

adequate alignment is motivated, its principles discussed and my contributions presented.

As commented in Section 3.3.2, the ID is used to reconstruct the trajectories of the charged particles by combining into tracks the energy deposits (hits) of the particles as well as identifying primary and secondary vertices. These functionalities are essential for some tasks such as the lepton reconstruction or the  $b$ -jet tagging.

To be able to have proper tracking, the full resolution of the ID has to be exploited and to do so it is crucial to know the geometry of the detector, i.e. the location and orientation of each of its elements. Due to several factors such as thermal expansion/contraction, the detector is constantly experiencing small movements that affect to its geometry. With the alignment it is possible to account online for this displacements, re-calibrate and correct its effects. The alignment algorithm's accuracy is such that the position of the various detector parts may be established with a few microns of accuracy [83]. This accuracy is superior to that attained by directly measuring the module placements. Any missalignment of the different elements of the ID will degrade the quality of the track reconstruction, which is vital to perform any physics analysis. During the development of this thesis, I have contributed to the alignment of the ID through the refurbishment of the software package for monitoring the track-based ID alignment results obtained at the calibration loop and show them as a web-based service.

### 3.4.0.1 Local coordinate frame

In Section 3.3.1 the global ( $x$ ,  $y$ ,  $z$ ) Cartesian coordinate system of ATLAS was introduced. The local coordinate frame of an individual sensor of the detector ( $x'$ ,  $y'$ ,  $z'$ ) is also a Cartesian system. The local system is a right-handed frame with the origin placed at the geometrical centre of the module. According to the convention, the  $x'$ -axis and  $y'$ -axis are within the plane of the component and the  $z'$ -axis points outside of this plane. The  $x'$ -axis points to the most sensitive direction of the module. For the Pixel and IBL modules this is the shorter pitch side and, for the SCT, the perpendicular to the strip orientation. In the case of the TRT the  $y'$ -axis points along the wire while the  $x'$ -axis remains perpendicular to both the wire and the radial direction. The local coordinates are represented schematically in Figure 3.34.

The hits are reconstructed in the local coordinate frame of the different modules.

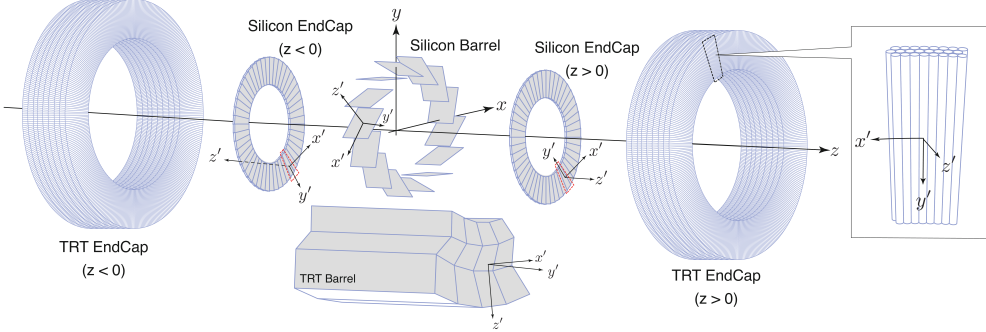


**Figure 3.34:** Schematic representation of the ATLAS global ( $x, y, z$ ) and local ( $x', y', z'$ ) reference frames [160]. The local coordinates are shown for the Pixel, IBL, SCT and TRT.

### 3.4.0.2 Track parameters

The trajectory followed by a charged particle within a magnetic field  $B$  is an helix that can be fully parametrised by the five track parameters:  $\boldsymbol{\tau} = (d_0, z_0, \phi_0, \theta_0, q/p)$ , where  $d_0$  and  $z_0$  are the transverse and longitudinal impact parameters;  $\phi_0$  and  $\theta_0$  the azimuthal and polar angles of the track. Lastly, the  $q/p$  is ratio between the particles charge and momentum and it measures the curvature of the tracks.

### 3.4.0.3 Alignment levels and degrees of freedom

The orientation of a rigid body can be described by a total of six degrees of freedom. This is translated into what are known as alignment parameters  $\boldsymbol{\alpha} = (T_x, T_y, T_z, r_x, R_y, R_z)$ . These correspond to the three translations with respect to the origin of the local reference frame ( $T_{x,y,z}$ ) and three rotations ( $R_{x,y,z}$ ) around the local Cartesian axes.

### 3.4.0.4 Residuals

In tracking, a residual is the distance between a hit and the intersection point of the extrapolated track in the sensor. The residual vector ( $\mathbf{r}$ ) is define as:

$$\mathbf{r} = (\mathbf{m} - \mathbf{e}(\boldsymbol{\tau}, \boldsymbol{\alpha}))$$

where  $\mathbf{m}$  is the vector to center of the module and  $\mathbf{e}(\boldsymbol{\tau}, \boldsymbol{\alpha})$  is the vector to the track intersection with the surface. For every track and module there is a residual, as it is shown in Figure 3.35.

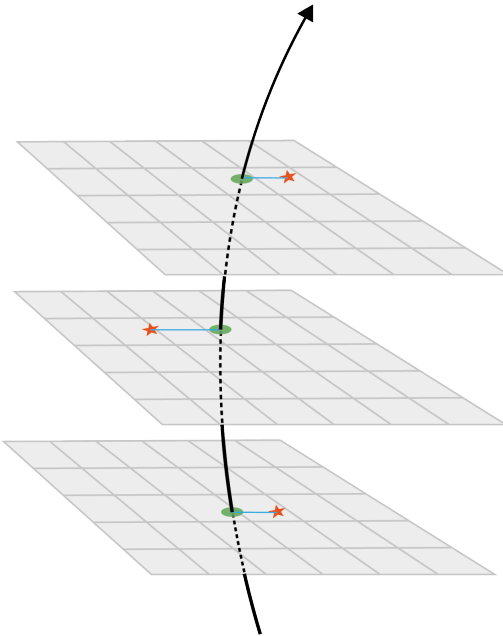


**Figure 3.35:** Schematic representation of a charged particle crossing detector planes [160]. The red star measures represents the measurement in each layer ( $m_i$ ). The black line is the fitted trajectory for a given set of track parameters. The position of the intersection of the fitted track with the surface ( $e_i$ ) on which the  $i^{th}$  measurement is made is indicated with a green ellipse. The residuals ( $r_i$ ) are shown in blue.

### 3.4.1 Track based alignment

The distance between the hits and the fitted track should be null if the detector were perfectly aligned, and the residual distribution would be centred at zero and have a width that corresponded to the module resolution. Therefore, any deviation from the in the residual distribution would indicate a misalignment of the detector.

A schematic description of the alignment chain is illustrated in the three panels of Figure 3.36. The blue rectangles on the left panel of Figure 3.36 represent the true position of the detector modules. A charged particle deposits part of its energy in each module producing the hits, which are marked with red dots. The track of the particle is marked with a red line. The  $x$  distance is the deviation of the module from its apparent position. In the middle panel, the white rectangles represent the apparent position of each module. Here can be seen how the real position and the apparent one is not the same by an unknown distance  $x$ . This deviation leads to a discrepancy between the reconstructed tracks and the true ones. The residuals in the middle panel are represented by a green line, which corresponds to the difference between the recorded track (red dots) and the reconstructed one (blue dots). The residual distributions in this panel are displaced from

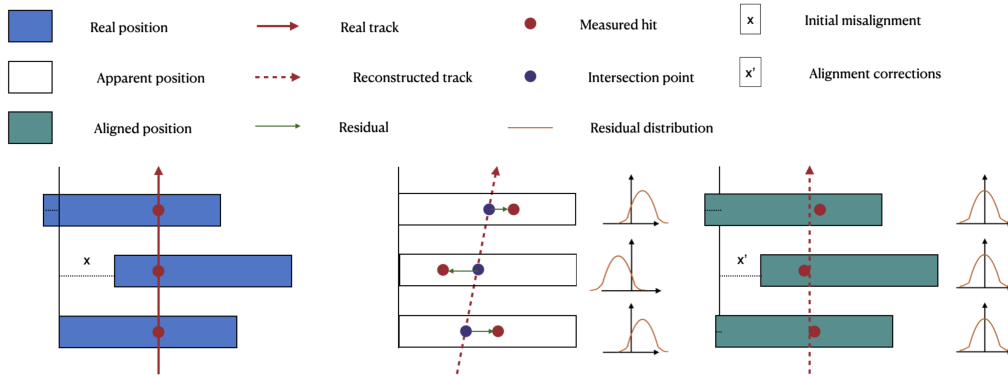


**Figure 3.36:** Alignment procedure scheme where each rectangle is a detector module. The left panel represents the real position of the detector modules and the charged particle track. The middle panel shows the initially-expected position of the modules and the reconstructed track. The right panel exemplifies how the position of the detectors has been updated to resemble the real one. This update is done by the track-based alignment procedure. **I need to vectorise this image**

zero, indicating a misalignment. The purpose of the alignment algorithm is to center this distributions in zero by minimising these residuals. As a result of the alignment procedure, the position of the detectors has been updated a distance  $x'$  for each module. After this, the new expected position of the modules (green rectangles) is much closer to the real one and, hence, the residuals are more centred at zero. Anyhow, this is not perfect and the different  $x'$  are not all equal to  $x$ . To improve the precision, the alignment procedure is carried iteratively.

### 3.4.1.1 Global $\chi^2$ algorithm

To correct the position of the the ID, the alignment constants ( $\boldsymbol{\alpha}$ ) are obtained as result of the minimisation of the  $\chi^2$  function. This function is built from the track-hit residuals:

$$\chi^2 = \sum_t \sum_h \left( \frac{r_{t,h}(\boldsymbol{\tau}, \boldsymbol{\alpha})}{\sigma_h} \right)^2,$$

where the index  $t$  runs over the reconstructed tracks and the  $h$  is the set of hits associated to each track  $t$ . The residual of each hit associated to track  $t$  is  $r_{t,h}$  and  $\sigma_h$  is the hit's uncertainty. In vector notation, the  $\chi^2$  function can be expressed as:

$$\chi^2 = \mathbf{r}^T \Omega^{-1} \mathbf{r},$$

where  $\omega$  is the covariance matrix of the corresponding measurements. The track parameters,  $\boldsymbol{\tau}$ , are those that minimise the  $\chi^2$  and, therefore, first and

second derivatives of  $\chi^2$  with respect  $\boldsymbol{\tau}$  are used.

$$\frac{d\chi^2}{d\boldsymbol{\tau}} = \sum_t \left[ \left( \frac{d\mathbf{r}}{d\boldsymbol{\alpha}} \right)^T \Omega^{-1} \mathbf{r} \right]^T + \sum_t \left[ (\mathbf{r}^T \Omega^{-1} \left( \frac{d\mathbf{r}}{d\boldsymbol{\alpha}} \right)) \right] = 0$$

It is worth to remind that  $\mathbf{r}$  and  $\Omega$  are defined for a single track, so the summary will accumulate the residuals from all considered tracks from all the events in the data sample. The last expresión can be simplified taking into account that  $\Omega^{-1}$  is symmetric and it takes the form:

$$2 \sum_t \left( \frac{d\mathbf{r}}{d\boldsymbol{\alpha}} \right)^T \Omega^{-1} \mathbf{r} = 0 \quad (3.10)$$

Since  $\mathbf{r} = \mathbf{r}(\boldsymbol{\tau}, \boldsymbol{\alpha})$ , the partial derivatives have to be taken into account:

$$\frac{d\mathbf{r}}{d\boldsymbol{\alpha}} = \frac{\partial \mathbf{r}}{\partial \boldsymbol{\tau}} \frac{d\boldsymbol{\tau}}{d\boldsymbol{\alpha}} + \frac{\partial \mathbf{r}}{\partial \boldsymbol{\alpha}}$$

Inserting this into Equation 3.10, the condition for minimising the  $\chi^2$  turns to be:

$$\sum_t \left( \frac{\partial \mathbf{r}}{\partial \boldsymbol{\tau}} \frac{d\boldsymbol{\tau}}{d\boldsymbol{\alpha}} + \frac{\partial \mathbf{r}}{\partial \boldsymbol{\alpha}} \right)^T \Omega^{-1} \mathbf{r} = 0 .$$

Here, the term  $d\boldsymbol{\tau}/d\boldsymbol{\alpha}$  is of particular importance since its contains the relationship between the track and alignment parameters, and it will determine the difference between the *Local* and *Global*  $\chi^2$  algorithms.

If the algorithm assumes that track parameters do not depend on the alignment, i.e.  $d\boldsymbol{\tau}/d\boldsymbol{\alpha} = 0$ , it is the so-called *Local*  $\chi^2$  algorithm. On the other hand, the *Global*  $\chi^2$  is based on the assumption that the track and alignment parameters are dependent.

### 3.4.1.2 Weak modes

## 3.4.2 Alignment results during Run-2

[Preguntar a Paolo sobre esto](#)

## 3.4.3 Alignment towards Run-3

[Preguntar a Paolo sobre esto](#)

### 3.4.3.1 Pseudo-real-time-online monitoring

## 3.4.4 Web-based display for alignment monitoring

The ID Alignment Monitoring Web Display is an application intended for monitoring the track-based alignment results obtained at the calibration loop for the ID. It helps to evaluate the computed alignment correction as well as many graphical distributions related with the performance (for example, the detector residuals).

The web application consists in a server, managed by ATLAS Distributed Computing, and a collection of scripts to produce distributions, update the information and handle the http requests.

New code:

- Changed both the back-end and front-end of the application.
- Previous version of the code need to have the year hardcoded, now it is automatic
- Now it is possible to update a single run or list of runs but in the previous version it was necessary to execute over all runs again.
- Debug levels implemented
- The web uses the standard athena setup instead of loading a bash script with the version hardcoded
- Depending on which run was decided top plot it was necessary to hardcode the year in the scripts, now it can be done from the web tool
- In the old version the `serverManageOutputs201X.py` had to be redone every year but now this is not necessary anymore. The year is indicated as an input.
- A lot of duplicities have been suppressed. The same lines were written over and over. Now functions and methods for addition of variables and classification are used.
- The aesthetics of the web page are the more visible change in the monitor display. Using the cherrypy library. And enhanced display has been built that allows to choose which information is shown. Mobile adapted with bootstrap.

- The old information was not able to read the information form ami while now we are able.
- code migrated
- Before we used to make a loop over all runs (`runListInTestingFolder`) and if for a certain run the info had to be updated or it was new, we added this run to a list (`RunsWithData`) over which we made a second loop fill the information. Now we do everything in a single loop over all runs filling the info on the fly if necessary. This makes the code more clean, clear and understandable.

# Chapter 4

## Recording data and simulating events in ATLAS

[161]

### 4.1 Data

- How is data collected in ATLAS? DAQ
- Pileup (differentiate LHC pileup from ATLAS pileup during Run 2)
- What are triggers

#### 4.1.1

#### 4.1.2

#### 4.1.3

### 4.2 Monte Carlo

In order to study the physics taking place into the ATLAS detector, the signals and backgrounds in the analysis are simulated by Monte Carlo generators according to the cross sections predicted by the SM. The use of the MC simulations is vast and there are many different models generators and techniques. As all MC algorithms, these methods rely on repeated random sampling to obtain numerical results. In the context of this work,

the MC generators provide a detailed simulation of the processes from the event generation through to output in a format which is identical to that of the true detector.

Typically, the simulation chain is divided into these three steps [161]:

1. Generation of the events and immediate decays: An event generator produce the result of the collisions in terms of particles created and stores any stable particle expected to propagate through the detector. At this point, the geometry of the detector is not considered because only the immediate decays are taken into account. Here
2. Simulation of the detector and physic interactions: At this point, all particles from the previous step are propagated though the full ATLAS detector using GEANT4. This part simulates all major components and materials as well as the interactions of particles such us ionisation in trackers, energy deposition in calorimeters, intermediate decays, ration and scattering
3. Digitalisation of the energy deposits on the sensitive regions of the detector.

The output of the full simulation chain is an object with the exact same format as a real event registered by the ATLAS DAQ system. This and the entire simulation chain are shown in Figure 4.1 and compared to the path that the data follows when it is originated from an actual collision.

The so called “truth” data is kept for each event and particle in both event generation and detector simulation. The truth is a history of the interactions from the generator. In the analysis presented in Chapter 6, the truth information has several uses such us the determination of fake rates or the lepton origin assignment. An important part of the work carried during the thesis was the proper implementation of the truth information at generator level within ATLAS software framework, Athena.

### 4.2.1 MC simulations

The generation of the simulated event samples includes the effect of multiple  $pp$  interactions per bunch crossing, as well as the effect on the detector response due to interactions from bunch crossings before or after the one containing the hard interaction.

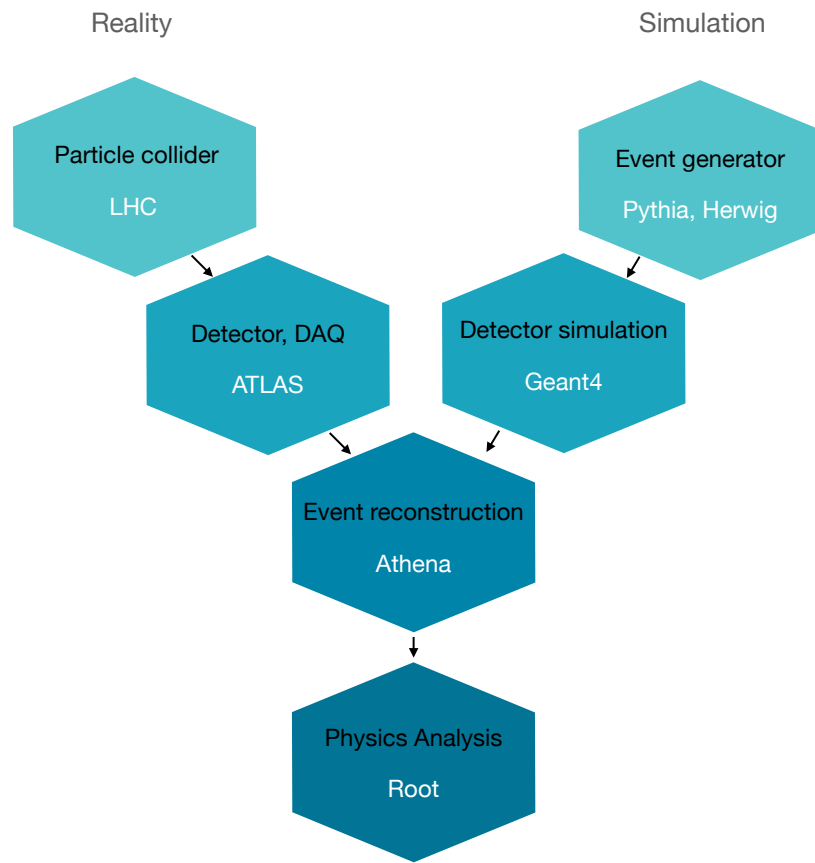


**Figure 4.1:** Comparison of the paths followed by data recorded by the ATLAS detector and the simulated samples.

#### 4.2.1.1 Parton shower simulation

#### 4.2.1.2 Hadronisation simulation

#### 4.2.1.3 Underlying decay simulation

#### 4.2.1.4 Hadron decay simulation

#### 4.2.1.5 Pile-up simulation

### 4.2.2 MC generators

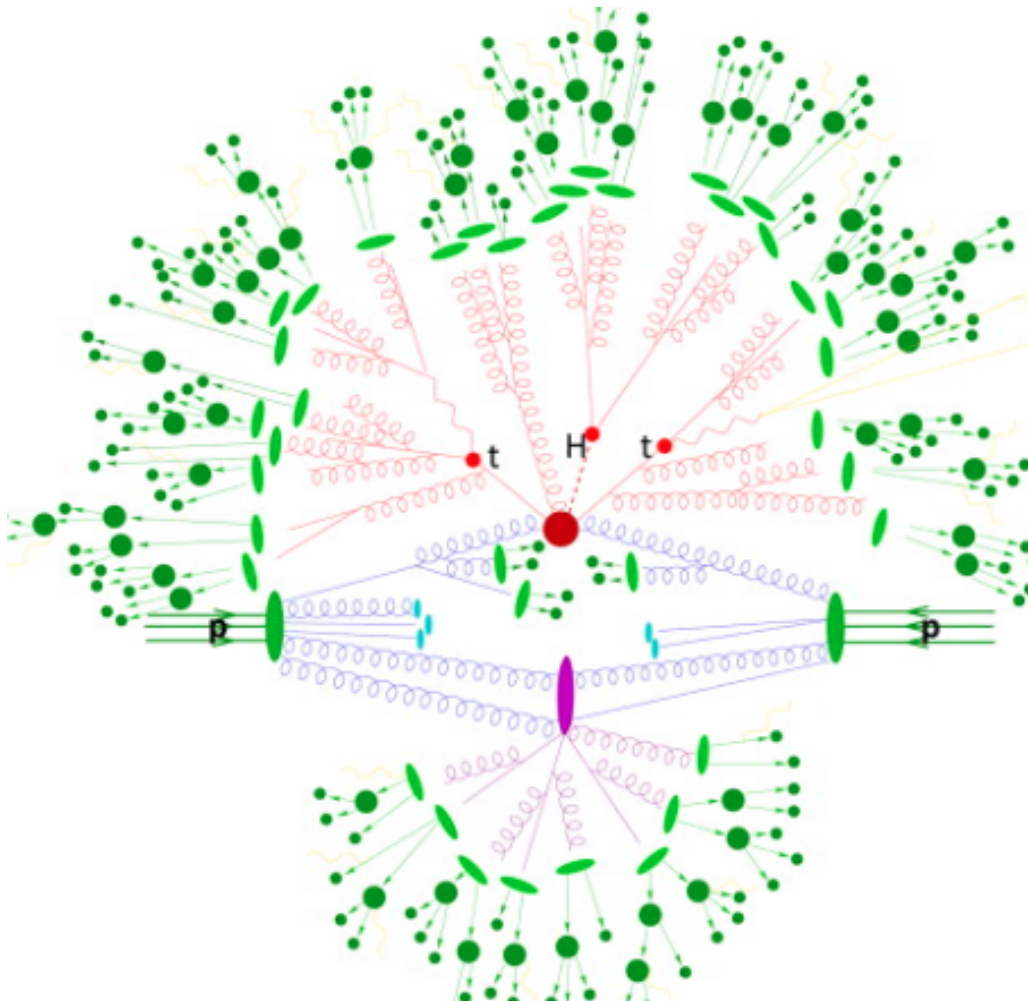


**Figure 4.2:** Representation of a  $t\bar{t}H$  event as produced by an event generator [162]. The big red blob is the hard interaction, which is followed by the decay of the Higgs boson and the two top quarks, represented by the three small red blobs. The additional QCD radiation produced is in red. The secondary interaction, in purple, occurs before the hadronisation of the the final-state partons (light green). In darker green, the hadron decay is presented and in the photon radiation appears in yellow.

# Chapter 5

## Object reconstruction and identification

### Highlight the importance of alignment for the reconstruction

To reconstruct the physical objects, the information of all the sub-detectors and systems of ATLAS is employed. A detailed description of all of them is presented in Section 3.3. After passing the trigger preselection, the raw data is analysed to build the physics objects that constitute the subject of the physical analyses. The process of constructing these elements is known as reconstruction. Figure 3.16 illustrates how each particle interacts with the different layers of the ATLAS detector. The reconstructed objects are the particles tracks and vertices, the leptons, the photons, jets (and their flavour tag) and the missing transverse momentum.

### 5.1 Tracking

The detection and measurement of charged particles moment is an essential aspect of any large particle physics experiment. Regardless of the medium through which a charged particle travels, it always leaves a trail of ionised atoms and liberated electrons. By detecting this it is possible to reconstruct the trajectory of a charged particle. ATLAS does this through its silicon detectors.

The trajectories followed by particles are referred as “tracks”. For charged particles, the tracks are reconstructed using, mainly, the information of the ID and, in the case of muons, the MS. A charged particle passing through the ID will interact with its active sensors, the pixel detector and SCT (Figures 3.22 and 3.23 respectively) providing a three-dimensional

measurement of space-points. While each hit in the pixel detector is directly translated into a space-point, for the SCT two hits are needed to reconstruct one space-point. These space-points can be given by a single pixel activation or by several neighbouring pixels activated simultaneously. Since the ID is submerged in a solenoidal magnetic field, the charged particles have their trajectories curved by the Lorentz force, this allows to calculate its  $p_T$  using the sagitta method. The track reconstruction is performed in two s

**Highlight the importance of the alignment for the object definition and its reconstruction. Link this section with 3.4**

### 5.1.1 Sagitta method

## 5.2 Vertices

## 5.3 Electrons and photons

## 5.4 Muons

## 5.5 Jets

At accelerator based detectors, quarks and gluons are detected by the jets of hadronic particles that they produce in the detector soon after they are created (remember that, as stated in Section 1.1.4, free quarks are suppressed due to color confinement). An exception to this rule are the top quarks, whose lifetime is smaller than the hadronisation time by two orders of magnitude and, hence, they are detected by its decay products. For the gluons and the rest of quarks, hadronisation showers (Section 3.3.3.1) take place and jet clustering algorithms merge the clusters and tracks produced by these jets to reconstruct them. In the majority of ATLAS analyses, the “Anti- $k_t$ ” algorithm is used [163] to analyse the data from hadronic collisions. Modelling the jet as a cone, the algorithm uses a specific choice of radius parameter ( $R$ ) defining the radial size of the jet. The distance between all pairs of objects  $i$  and  $j$  ( $d_{ij}$ ) and the distance between the objects and beam pipe ( $d_{iB}$ ) are used in:

$$d_{ij} = \min(k_{ti}^{2p}, k_{tj}^{2p}) \frac{\Delta_{ij}^2}{R^2}$$

$$d_{iB} = k_{ti}^{2p}$$

where

$$\Delta_{ij}^2 = (y_i - y_j)^2 - (\phi_i - \phi_j)^2$$

and  $k_{ti}$ ,  $y_i$  and  $\phi_i$  are respectively the transverse momentum, the rapidity and the azimuthal angle of object  $i$ . The parameter  $p$  accounts for the relative power of the energy versus geometrical ( $\Delta_{ij}$ ) scales. For the Anti- $k_t$ ,  $p$  is set to  $-1$ . Other clustering algorithms use different choices of  $p$  such as  $p = 0$  (Cambridge/Aachen algorithm) or  $p = 1$  (inclusive  $k_t$  algorithm).

The algorithm iterates over the topological-cluster (or, simply, top-clusters) objects of the calorimeter as it follows: First it proceeds to identify the smallest distances with among all the combinations of  $d_{ij}$  and  $d_{iB}$ . If the distance is a  $d_{iB}$ , the entity  $i$  is labeled as “jet” and removed from the list of entities. If, on the contrary, it is a  $d_{ij}$ , the objects  $i$  and  $j$  are merged together. This way, before clustering among themselves, soft components (low- $p_T$ ) tend to be merged to the hard ones (high- $p_T$ ). Then the distances are recalculated and the process repeated. This is done iteratively until all entities are assigned to a particular jet.

If a hard particle has no hard neighbours within a  $2R$  distance, all soft particles will be assigned to it, resulting in a perfectly conical jet. But if another hard particle is present in that  $2R$  distance, then there will be two hard jets and it will be impossible for both to be perfectly conical.

### Work in progress

Typically, the cone size  $R$  is selected to be 0.4 or 0.6, though the most standard used in ATLAS is 0.4. If  $R = 1$ , the jet is labeled a Large- $R$  and if  $R = 0.4$  then as Small- $R$  jet.

#### 5.5.1 Jet energy calibration and resolution

The jet calibrations and the associated uncertainties are clearly extremely important in many top analyses. This often makes them the leading experimental uncertainties in Top analyses

### 5.5.2 Bottom quark induced jets

In general, it is impossible to determine which quark flavour was produced or even whether the jet was originated by a quark or a gluon. However, if a  $b$  quark is created, the hadronisation will produce a jet of hadrons, one of which will be a  $b$ -type hadron (B hadron). The B hadrons turn out to be relatively-long-lived particles ( $1.5 \times 10^{-12}$  s). If this larger longevity is combined with the Lorentz time-dilation that particles experience when produced in high energy collisions, it results in the B hadron traveling on average a few mm before disintegrating.

As a result, the experimental signature of a  $b$  quark is a jet of particles emerging from the point of collision (primary vertex) and a secondary vertex resulting from  $b$ -quark decay that is several mm away from the primary vertex. Therefore, the capacity to resolve secondary vertices from the parent vertex is crucial for identifying  $b$ -quark jets.

## 5.6 Missing transverse energy

## 5.7 Overlap removal

# Chapter 6

## Search for rare associate $tHq$ production

### 6.1 Introduction

#### Describe the strategy for the $2\ell + 1\tau_{\text{had}}$ analysis

The study of the  $tHq$  production can be classified attending to the number of light-flavour leptons ( $\ell$ ), i.e. electrons or muons, and hadronically-decaying tau leptons ( $\tau_{\text{had}}$ ). According to this criteria, the channels presented in Table 6.1 have been defined. As can be seen in the table, the study of the  $1\ell$  channel uses only the  $H \rightarrow t\bar{t}$ , which is the most dominant decay mode for the Higgs boson with a 58% BR as is reported in Section 2.2.3. However, for the multileptonic channels the  $H \rightarrow W^+W^-$ ,  $H \rightarrow \tau^-\tau^+$  and  $H \rightarrow ZZ$  are considered. These three Higgs decay channels combined account for a total 21% BR.

#	0 $\tau_{\text{had}}$	1 $\tau_{\text{had}}$	2 $\tau_{\text{had}}$
$1\ell (e/\mu)$	$tHq (b\bar{b})$ $1\ell$		$tHq (WW/ZZ/\tau\tau)$ $1\ell + 2\tau_{\text{had}}$
$2\ell (e/\mu)$	$tHq (WW/ZZ/\tau\tau)$ $2\ell \text{ SS}$	$tHq (WW/ZZ/\tau\tau)$ $2\ell + 1\tau_{\text{had}}$	
$3\ell (e/\mu)$	$tHq (WW/ZZ/\tau\tau)$ $3\ell$		

**Table 6.1:** Different channels for  $tHq$  production according to the presence of light-flavoured leptons and hadronically-decaying taus in the final state.

Moreover, depending on the relative charge between the light charged leptons, the  $2\ell + 1\tau_{\text{had}}$  channel is further subdivided in two sub-channels. The so-called  $2\ell \text{SS} + 1\tau_{\text{had}}$  channel is defined by the events in which the two light leptons have the same electric charge. In contrast, the one in which they have opposite electric charge is known as  $2\ell \text{OS} + 1\tau_{\text{had}}$  channel. For simplicity, through this document, these two sub-channels are usually referred just as SS and OS respectively.

The work of this thesis is focused in the  $2\ell + 1\tau_{\text{had}}$  channels. To do so, the  $2\ell \text{SS} + 1\tau_{\text{had}}$  and  $2\ell \text{OS} + 1\tau_{\text{had}}$  are treated separately since they have different background compositions, being the  $2\ell \text{SS} + 1\tau_{\text{had}}$  the one with the lower background contribution.

- different MVAs trained for each channel

When assuming that one of the light-flavoured leptons is originated from the Higgs-boson decay and the other one from the top-quark decay, the determination of which lepton comes from which particle is direct for the  $2\ell \text{OS} + 1\tau_{\text{had}}$  but not for the  $2\ell \text{SS} + 1\tau_{\text{had}}$ . Since knowing the origin of the light-flavoured leptons can be very useful to define variables with the power to discriminate the  $tHq$  signal from the background, tools are developed to associate these leptons to its parent particles.

- The fake rate estimates for light leptons and tau leptons are being checked to see if there is anything that has to be treated differently for the two sub-channels.

## 6.2 Data and simulated events

- the tH samples were done with MADGRAPH5\_AMC@NLO +PYTHIA 8 +EVTGEN

The underlying event is generally done with Pythia8 in ATLAS. In the  $tHq$  samples we used MADGRAPH5\_AMC@NLO for the calculation of the matrix element and PYTHIA 8 for the hadronisation and parton showering. We are also working on alternative samples with HERWIG 7 as parton shower generator. **While in section 3 I describe how the events and samples are generally generated and simulated, in this section I should describe what is specifically used in this analysis**

### 6.2.1 Single lepton triggers

## 6.3 Object definition

**Highlight the importance of alignment**

## 6.4 Signal

In this section, it is discussed how it is find what we know as signal. In a particular study, the “signal” is the set of events in the dataset that correspond to the process of interest. Therefore, in this case, the signal is composed by  $tHq$  production events with a  $2\ell + 1\tau_{\text{had}}$  final state. In contrast, the background processes are those which, a priori, look like the signal process but it is not. A more detailed definition of what a background is and how it is classified can be found in Section 6.5.

### 6.4.1 Signal generation and validation

**rivet**

### 6.4.2 Parton-level truth validation

- > Describe what are truth level and reconstruction level.
  - > The truth information is whatever comes from the generator, the physics without taking into account the effects of the detector. The truth level does not include the effects of the interaction with matter. The truth also includes the parton shower and hadronisation information.
  - > truth = generator + parton shower + hadronisation
  - > The studies I did were done at generator level
  - > Particle level is part of truth information
  - > Detector level = reconstruction level + calibration +
  - > Creo que esto se explica bien en la tesis de florencia
- (maybe write the calculations of BR\_tHq in the Section 6.4.2 )**

### 6.4.3 Lepton assignment

The two light leptons in the final state of the  $2\ell + 1\tau_{\text{had}}$  channel can originate either from the Higgs boson or the top quark. The ambiguities regarding the origin of these light-flavoured leptons, make the reconstruction of the top quark and Higgs boson systems extremely difficult. Nevertheless, the electric charge of these leptons could provide us useful information to probe their origins.

To have knowledge of whether the light-flavoured leptons in the final state are originated from the Higgs boson or the top quark is very beneficial in order to both reconstruct the event and design variables at reconstruction level with high discriminant power. As is shown in Sections 6.6.4 and 6.6.5, the variables using the lepton assignment information play a relevant role not only in the definition of the signal-enriched section but also in the determination of the control regions to constrain the most important background processes.

According to the calculations performed by combining the BR of the Higgs boson, the top quark and all its decay products (see Section 6.4.2), in the  $2\ell + 1\tau_{\text{had}}$  channel of  $tHq$  production, the  $\tau_{\text{had}}$  is produced 83.7% of times as a product of the Higgs-boson decay in opposition to the 16% in which it comes from the top-quark disintegration.

#### Opposite-sign Leptons

In the dominant scenario ( $\tau_{\text{had}}$  from Higgs) the association of which light-flavoured lepton comes from the top-quark decay and which one comes from the Higgs-boson decay can be done directly if these two leptons have opposite electric charge, i.e. in the  $2\ell \text{ OS} + 1\tau_{\text{had}}$  channel. Since in Higgs boson is neutrally charged, the sum of the charge of its decay products should be zero. Therefore, in the OS channel, while the light lepton with opposite charge to that of the  $\tau_{\text{had}}$  is the one coming from the Higgs, the other lepton, i.e. the one with the same charge as  $\tau_{\text{had}}$ , is the one originated from the top-quark decay.

#### Same-sign Leptons

In contrast to the the  $2\ell \text{ OS} + 1\tau_{\text{had}}$  channel, in the case of  $\tau_{\text{had}}$  from Higgs, when the two light leptons have the same electric charge (the so called  $2\ell \text{ SS} + 1\tau_{\text{had}}$ ) it is not possible to know, a priori, which of the leptons comes from the top-quark system and which from the Higgs-boson decay.

In order to perform this association for the  $2\ell \text{ SS} + 1\tau_{\text{had}}$  several methods relying in the truth-level information have been tested. **Describir superficialmente los métodos listados en el ítemize**

- First method (Cyrus): Assume that the leading lepton was originated from the top
- Second method (Mathias): Cut in two variables
  - Cut 1:  $m_{vis,H}(\text{lep}(t)) - m_{vis,H}(\text{lep}(H)) > 57.0 \text{ GeV}$
  - Cut 2:  $m_{pred,t}(\text{lep}(H)) - m_{pred,t}(\text{lep}(t)) > 0.0 \text{ GeV}$
- BDT based method presented in this work

#### 6.4.3.1 Labelling the $2\ell \text{ SS} + 1\tau_{\text{had}}$ with the reconstruction-level and truth-level matching

Even though at reconstruction level it is not known which are the parents of the particles in the final state, at parton level this informations is accesible, in other words, the origin<sup>1</sup> of the light leptons is known. For a given event, it is possible to access to both the particle-level and parton-level information simultaneously. Having the parton-level leptons, whose parents are known, and the reconstruction level leptons, whose parents need to be identified, it is possible to compare them to create an association. Specifically, identify which parton-level lepton correspond to which reconstructed lepton. The aim of this relation is to assign the leading ( $\ell_1$ ) and sub-leading ( $\ell_2$ ) light leptons at reconstruction level to the the “lepton from top-quark-decay chain” ( $\ell_{\text{top}}$ ) and “lepton from Higgs-boson-decay chain” ( $\ell_{\text{Higgs}}$ ) at truth level.

In order to link the reconstruction-level light leptons to the parton-level light leptons, a  $\Delta R < 0.01$  cone around each of the reconstructed leptons is built. When inside that cone there is exactly one truth-level light lepton, there is what is called “a match”. Figure 6.1 presents the possibles scenarios of the association. In order to identify properly determine the lepton origin in an event, it is required that both leptons at reconstruction level have a match. There are two different cases for this. The first situation is that in which the leading-light lepton is  $\ell_{\text{top}}$  and the sub-leading is  $\ell_{\text{Higgs}}$ . For the sake of simplicity, this configuration is named “Type 1” and it is represented in Figure 6.1a. The second double-matching combination is the other way around, the leading-light lepton is  $\ell_{\text{Higgs}}$  and the sub-leading is

---

<sup>1</sup>By origin of a light lepton is meant whether it comes from the Higgs-boson-decay chain or the top-quark-decay chain.

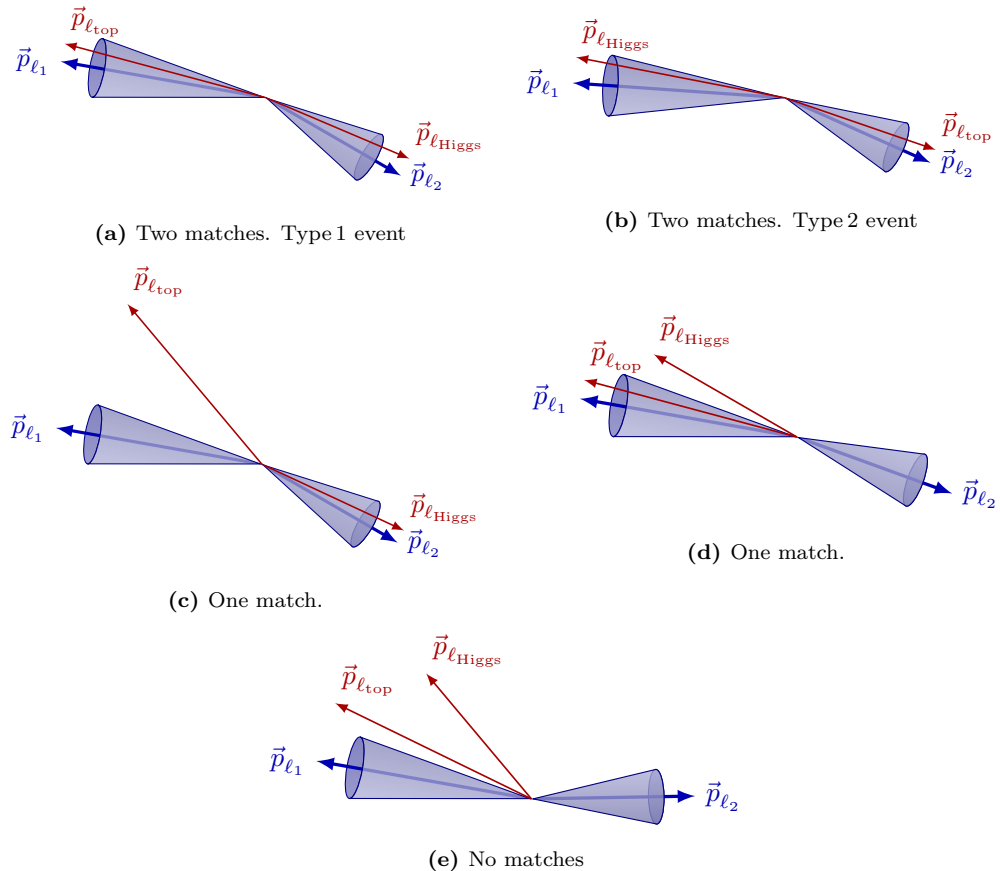


**Figure 6.1:** Association between reconstruction-level (blue) and parton-level (red) light leptons. Note that the labels  $\ell_{\text{top}}$  and  $\ell_{\text{Higgs}}$  are only available for the parton-level particles.

$\ell_{\text{top}}$ . Pictured in Figure 6.1b, this type of events are called “Type 2”. On the contrary, if only one of the two reconstructed light leptons is matched (Figure 6.1c), none of the leptons are classified. If a less strict criteria was used, it would be possible requiere only one of the two leptons matching in order to classify the event (the unmatched reconstruction-level lepton would be assigned to the unmatched parton-level lepton). The problem of the lax strategy is that while in cases like that on Figure 6.1c it seems clear that unmatched parton correspond to the unmatched reconstructed lepton, for events such as the illustrated in Figure 6.1d the unmatched particle does not necessarily belong to the  $\ell_2$  cone. For this reason, it is mandatory that both reconstructed light leptons have a match. Finally, in the scenario in which none of the parton-level leptons fall into the cones (Figure 6.1e), no assignation takes place.

To perform this labelling, it has been required that the  $\tau_{\text{had}}$  is originated in from the Higgs-boson system. This is imposed in order to guarantee

that there are both a  $\ell_{\text{top}}$  and a  $\ell_{\text{Higgs}}$ . The Higgs-decay channels used for these studies are the  $H \rightarrow \tau\tau$  (one  $\tau$  decaying leptonically and the other hadronically) and the  $H \rightarrow WW$ . The  $H \rightarrow ZZ$  channel has not been included since its impact in the on the  $2\ell + 1\tau_{\text{had}}$  production when the  $\tau_{\text{had}}$  comes from the Higgs is very tiny. If the  $\tau_{\text{had}}$  is originated in the Higgs system, only a 2.0% of the events correspond to the  $H \rightarrow ZZ$  decay channel, contrasting with the 76.5% of the  $H \rightarrow \tau\tau$  and the 21.5% of the  $H \rightarrow WW$ .

**Should add the fraction of events that are labeled from a) the total  $2\ell + 1\tau_{\text{had}}$  sample and b) from the total  $2\ell \text{ SS} + 1\tau_{\text{had}}$ .**

#### 6.4.3.2 BDT-based method for lepton association

- Describe the idea of using reco-level variables to predict (on unlabelled data) whether it is a “Type 1” or “Type 2” event by means of a BDT trained with labeled data (isLep1fromTop)
- Describe with a few words what a BDT is and reference appendix B.
- Using root.TMVA - Advantages: Nowadays most of ML frameworks (keras, pyTorch, scikit-learn, XGBoost, etc..) are based on python. These libraries expect numpy arrays or panda data-frames as input, so the first thing to do when using the analysis NTuples is to convert the ROOT data-frame. An advantage of using TMVA library of ROOT is that this data conversion is not necessary. is that
- Describe the particularities of this gradient BDT with detail
- One way to reap the benefits of a large training set and large test set is to use cross validation: k-folding.
  - Programmed in an external-to-tHqLoop script
  - Trained only over SS signal events. In contrast to the BDT of SR that trains over all process, this one trains only over signal because its objective is to determine which lepton comes from which particle in the signal events and this classification only makes sense in signal processes.
- Present the feature importance
  - Present distributions of used variables and a list with the meaning of this variables
  - Present correlations between pairs of used variables. Note that the correlation maps search for bidimensional correlations (i.e.

between pairs of two variables) and the BDT uses N-dimensional relations. (Page 26 of the TMVA guide)

—

- Discuss the negative weight strategy: Present used distributions with 'all weights' and with 'positive weights'
  - in contrast to XGboost, ROOT.TMVA can deal with negative weights
- Hyperparameter optimisation
- Present BDT response, ROC curve, ¿something else?
- Compare to the results using other MVA methods.
- The BDT is integrated in tHqLoop (weights.xml) ¿Where do I describe what tHqLoop is?
- From tHqLoop, the BDT score can be calculated for all the events (signal or not) and then the efficiency of the lepton association can be calculated depending on the threshold point which is chosen to define whether the event is Type1 or Type2. Note that this efficiency is computed only over signal events. → Table of 'efficiency vs cutpoint'

#### 6.4.4 Top quark and Higgs boson reconstruction

**En aras de que esto es extremadamente complicado y no se logró hacer ¿tiene sentido redactar una sección?**

### 6.5 Background estimation

The background can be defined as everything in a subset of the data that simulates the signal processes without truly being a signal event. In other words, in this studies, everything that is not signal, is background. In this case, whatever that mimics the signature of an associated  $tHq$  production with  $2\ell + 1\tau_{\text{had}}$  final state is referred as background.

In order to perform the physics analysis, it is fundamental to subtract the background events from the dataset as much as possible in order to achieve higher signal purity. By doing this, the analysed dataset resembles more to the process that is desired to study. This procedure is the so called "event selection" and its described in Section 6.6

There are two different types of background: “reducible” backgrounds, where particles imitate the particles we are looking for (for instance, a high-energy electron can mimic a high-energy photon), and “irreducible” backgrounds, where particles are the same kind as the ones we are looking for.

The main source of background in the  $2\ell + 1\tau_{\text{had}}$  channel is due to signatures of hadronic tau decays, more specifically, of jets faking  $\tau_{\text{had}}$ .

[Add Oleh pieCharts](#)

### 6.5.1 Fakes estimation

$\tau^-$  fakes are more important than light lepton fakes

**This is taken from the intNote. I have to reorganise and rephrase this information** The requirements for the objets defined in section (ref ref) provide significant suppression of events with jets wrongly selected as leptons is achieved by asking electrons and muons to pass the tight requirement that combines `tightLH ID` for leptons and `medium` for muons and `PLImprovedTight` isolation working points

Similarly, the hadronic taus are required to pass the `medium` requirement of the RNN-based discriminator. Even so, the selected data sample is expected to be contaminated with such type of reducible background. It is also expected that the simulation of jets faking leptons (electron, muon, hadronic tau) in ATLAS detector is imprecise or unreliable. Therefore, an important step of the analysis is to estimate this background in data.

**Light-lepton fakes** Particles from the hard scattering process are referred as ‘prompt’. Acceptance, quality and isolation requirements are applied to select these leptons Non-prompt leptons and non-leptonic particles may satisfy these selection criteria, giving rise to so called ‘non-prompt and fake’ lepton backgrounds. Fake electrons/muons will not be explicitly distinguished and are referred as fake leptons. The mis-identified lepton background arises from leptons from heavy-flavour ( $\ell_{\text{HF}}$ ) hadron decay and electrons from  $\gamma$ -conversions. These leptons are mainly produced in  $t\bar{t}$ ,  $Z + \text{jets}$  and  $tW$  events.

The estimation of the fake/non-prompt lepton background is done with the template fit method or via the matrix method

The fake and real lepton efficiencies (fake/real rates) are defined as the probabilities of a fake or real electron or muon to pass the nominal electron/muon requirements. They are given by the tight over loose ratio

- Get some ideas from here: <https://cds.cern.ch/record/1951336/files/ATLAS-CONF-2014-058.pdf>

**Tau fakes** In the analysis channels involving hadronic taus, all methods used for fake background estimation rely on MC-based templates. These are splits of simulation according to a type of object mimicking the lepton of interest. Construction of MC templates related to the electron and muon fakes is based on `TruthClassificationTool` tool. [Describe the TruthClassificationTool](#)

- counting method
- template fit method

The extracted SFs are then applied to the simulated background component in the region with taus passing the preselection requirements.

### 6.5.1.1 $t\bar{t}$

### 6.5.1.2 $Z + \text{jets}$

## 6.5.2 Reducible backgrounds

All the processes whose signature is the same as the process of interest are known as reducible backgrounds as in contrast to the fake or irreducible backgrounds described in Section 6.5.1. The objects in the reducible backgrounds are prompt. The main reducible backgrounds are:

### 6.5.2.1 Diboson

#### 6.5.2.2 $tW$

#### 6.5.2.3 $t\bar{t}Z$

#### 6.5.2.4 $t\bar{t}H$

#### 6.5.2.5 $t\bar{t}W$

#### 6.5.2.6 $tZq$

## 6.6 Event selection

### The event selection

As more and more stringent requirements are made to eliminate these backgrounds we also lose signal events, so there is a trade off background rejection against signal acceptance. Since the data is not only limited but also scarce when it refers to the  $tHq$  signal, the event selection is a highly non-trivial process that requieres a lot of attention.

The signal selection is done in several steps and using different methods. First of all, it is defined a preselection region (PR) where the physical objects are selected according to the detector acceptance. The PR is a cut-based region. Then, discriminant variables are defined and used as input for a BDT. Finally, the BDT outputs are used to define the signal region (SR) and control regions (CR).

Two figures of merit are used to simultaneously optimise the fraction of signal events in the data and the absolute number of signal events. These metrics are the  $S/B$  or purity and the signal significance.

**Purity** : The purity of a process is defined as the ratio between the event yields of the target process and the total yields. Usually, for the signal, the signal to background ratio ( $S/B$ ) is used instead of the purity.

**Significance** : This metric does not only account to the relative fraction of the process of interest but also to the total amount events. Using the significance as metric enhances the importance of keeping enough statistics.

Process	SS	OS	SS + OS
$tHq$	0.9	1.2	2.1
$tZq$ (with $Z \rightarrow \ell\ell$ )	6.2	32.9	39.1
$t\bar{t}$	47.9	2965.0	3012.9
$tW$	2.3	118.9	121.2
$W$ + jets	1.9	0.5	2.4
$Z$ + jets	6.7	1956.2	1962.9
VV + jets (V= $W/Z$ )	8.9	121.6	130.5
$t\bar{t}W$	21.0	43.4	64.4
$t\bar{t}Z$	17.5	101.2	118.7
$t\bar{t}H$	17.8	43.2	61.0
$tWZ$ (with $Z \rightarrow \ell\ell$ )	3.1	16.4	19.5
$tWH$	0.6	1.5	2.1
Other	1.9	9.3	11.2
Total	136.7	5411.3	5548.0
S/B (%)	0.6627	0.0222	0.0379
Significance	0.0771	0.0163	0.0282

**Table 6.2:** Event yields at preselection level for SS, OS and SS+OS combination. **The  $W$  and  $Z$  MC only feature leptonic decays**

The definition of the significance estimator used in this work is the one given in reference [164]

$$\text{Significance} = \sqrt{2[(s+b)\ln(1+s/b) - s]}, \quad (6.1)$$

where  $s$  is the number of events of the target process and  $b$  is the number of yields for the rest of processes combined. This can be used not only to evaluate the signal significance but also the significance of the background processes in the dedicated CRs.

### 6.6.1 Preselection

**Refer to chapter 2 and the geometrical acceptance of the detector to justify the PR cuts**

Preselection requirements

### 6.6.2 Discriminant variables

To enhance the capability of discrimination between processes, new variables are build out of several others. Some of these are useful to improve the separation. The first task in this regard is to substitute the classification of the light leptons from leading ( $\ell_1$ ) and subleading ( $\ell_2$ ) lepton to  $\ell_{\text{top}}$  and  $\ell_{\text{Higgs}}$ . The variables using the light-lepton origin are more discriminant than the ones that classify them by the the  $p_{\text{T}}$ . **Aportar un figura donde se vea la diferencia entre emplear ( $\ell_1$ ,  $\ell_2$ ) y ( $\ell_{\text{top}}$ ,  $\ell_{\text{Higgs}}$ )**

### 6.6.3 BDT

Since a BDT is going to be used for both the lepton assignment and region definition, it may be interesting to describe the technicalities of the BDT in an appendix

Maybe, it can also be a good idea to explain the generalities of the BDT for region definition here and then put the BDT results into "Signal Region" and "Control Regions" section.

#### 6.6.3.1 Performance

#### 6.6.3.2 Ranking of variables

#### 6.6.3.3 Hyperparameter optimisation

Grid search

Genetic algorithm

**6.6.3.4 Negative-weights strategy****6.6.3.5 k-Folding****6.6.4 Signal Region****6.6.4.1 Same Sign channel****6.6.4.2 Opposite Sign channel**

Here I shall explain the problem with some variables such us MET that, despite having great separation power, produce the effect of not differentiating the  $tHq$  signal from the  $t\bar{t}$  contributions.

**6.6.5 Control Regions****6.6.5.1 Same Sign channel** $t\bar{t}$  $t\bar{t} W$  $t\bar{t} Z$  $t\bar{t} H$ **6.6.5.2 Opposite Sign channel** $t\bar{t}$  $Z +\text{jets}$ **Diboson** $t W$

## 6.7 Systematic uncertainties

Particle collision physics distinguish two types of uncertainties, the statistical uncertainty and the systematic uncertainty. The statistical uncertainty is the result of stochastic fluctuations in data and is the result of a limited size of analysed dataset. It is fully uncorrelated between subsequent measurements. On the other hand there are the systematic uncertainties, which are defined as everything that is not a statistical error. These are fully correlated between subsequent measurements and are associated with all sort of sources such us the measurement apparatus, the assumptions made, the model used, the MC generator and many others.

While the statistical uncertainty is usually intrinsically added in the inference method, the inclusion of the systematic uncertainties and its propagation through the statistical analysis are not trivial.

Alternative samples are produced to evaluate the systematics:

- Herwig<sup>7</sup>
- > parton shower
- asdfas. -> modelling

### 6.7.1 Theoretical uncertainties

### 6.7.2 Modelling uncertainties

### 6.7.3 Experimental uncertainties

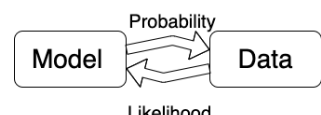
## 6.8 Fit results

### 6.8.1 Likelihood fit

**Maybe I move the statistics description to an appendix** The likelihood fit....

The likelihood function is defined as the probability of observing a certain set of data ( $\vec{x}$ ) given a model or hypothesis with certain parameter values ( $\vec{\theta}$ ). It is given by

$$L(\vec{\theta}) = \mathcal{P}(\vec{x}|\vec{\theta}) = \prod_i \mathcal{P}(x_i|\vec{\theta})$$



where  $i$  runs over the data points. By maximising the likelihood function, the parameters  $\vec{\theta}$  of the model that better fit the data are obtained. These are known as estimated values. The fit is the parameter estimation via the Likelihood maximisation,  $\vec{\theta}_{estimated} = \text{argmax}_{\vec{\theta}} L(\vec{\theta})$ .

For binned distributions the likelihood function can be written as

$$L(\vec{n}|\vec{\theta}) = \prod_{i \in bins} \mathcal{P}(n_i^{obs}|n_i^{exp}(\vec{\theta})) = \prod_{i \in bins} \mathcal{P}(n_i^{obs}|S_i^{exp}(\vec{\theta}) + B_i^{exp}(\vec{\theta}))$$

Here,  $i$  runs over the bins of the histogram,  $n_i^{obs}$  and  $n_i^{exp}$  are the observed and expected number of entries in the bin  $i$ . The predicted signal and background entries in the bin  $i$  are  $S_i$  and  $B_i$ .

Since particle physics experiments are counting experiments, the distribution follows the poissonian statistics. The Poisson distribution is a discrete probability distribution that expresses the probability of a given number of events occurring in a fixed interval of time or space if these events occur with a known constant mean rate and independently of the time since the last event

From the frequentist point of view the probability is defined as the fraction of times an event occurs, in the limit of very large number ( $N \rightarrow \infty$ ) of repeated trials

$$\mathcal{P} = \lim_{N \rightarrow \infty} \frac{\text{Number of favorable cases}}{N}$$

where  $N$  is the number of trials. Even though this infinity can be conceptually unpleasant, for LHC experiments, the amount of events is so large that this  $\mathcal{P}$  definition becomes acceptable [165].

In contrast, for the Bayesian (or subjective) probability expresses the degree of belief that a claim is true. Starting from a prior probability, following some observation, the probability can be modified into a posterior probability. The more information an individual receives, the more Bayesian probability is insensitive on prior probability [165].

The Bayes theorem [166] states that considering two events  $A$  and  $B$ , the probability of  $A$  to happen given that  $B$  takes places is

$$\mathcal{P}(A|B) = \frac{\mathcal{P}(B|A)\mathcal{P}(A)}{\mathcal{P}(B)}$$

where  $\mathcal{P}(B|A)$  is the conditional probability of  $B$  given  $A$  and  $\mathcal{P}(B)$  the probability of the event  $B$  to happen. Here,  $\mathcal{P}(A)$  has the role of prior probability while  $\mathcal{P}(A|B)$  is known as posterior probability.

**6.8.2 Strategy****6.8.3 Fit with Asimov data****6.8.3.1 Post-fit****6.8.3.2 Pruning****6.8.3.3 Nuisance Parameters****6.8.3.4 Correlation matrix****6.8.3.5 Ranking****6.8.4 Fit to data****6.8.4.1 Post-fit****6.8.4.2 Pruning****6.8.4.3 Nuisance Parameters****6.8.4.4 Correlation matrix****6.8.4.5 Ranking****6.8.5 Results****6.8.6 Data fit****6.9 Combination results**

Discuss results, compare them with CMS, future perspectives

...

**6.10 Conclusions**



# **Chapter 7**

## **Conclusion**



# Appendix A

## Effect of negative weights

### A.1 Negative weights uncertainties

- What is a weight in a MC event?
- Why are there negatively weighted events?
- Why are negative weights problematic?

### A.2 Statistical uncertainty of negative weights

Assume that there is a sample of  $N$  Monte Carlo simulated events. Of these, a fraction  $x$  have negative weights and, therefore, a fraction  $(1 - x)$  has a positive weight. The effective number of events is  $(N_+ - N_-)$ , being  $N_+ = (1 - x)N$  the amount of positively weighted events and  $N_- = xN$  the same for the negative weights.

The statistical fluctuations are calculated in terms of  $x$  and the standard deviation ( $\sigma_N = \sqrt{N}$ ). The number of positive and negative events can fluctuate randomly between  $\pm\sigma_-$  for the later and  $\pm\sigma_+$  for the former. Here,  $\sigma_- = \sqrt{xN} = \sqrt{x}N$  and  $\sigma_+ = \sqrt{1-x}N$

The variance ( $V = \sigma^2$ ) of the sample is then

$$V(N_+ - N_-) = xV(N) + (1 - x)V(N) = V(N)$$

and the fractional uncertainty

$$\frac{\sigma(N_+ - N_-)}{N_+ - N_-} = \frac{\sigma_N}{(1 - x)N - xN} = \frac{1}{1 - 2x} \frac{\sigma_n}{N}$$

When the fraction of negative events is  $x = 0$ ,  $\frac{\sigma(N_+ - N_-)}{N_+ - N_-} = \frac{\sigma_n}{N}$  as expected. In contrast, if  $x = 0.5$  the fractional uncertainty is infinite, as expected.

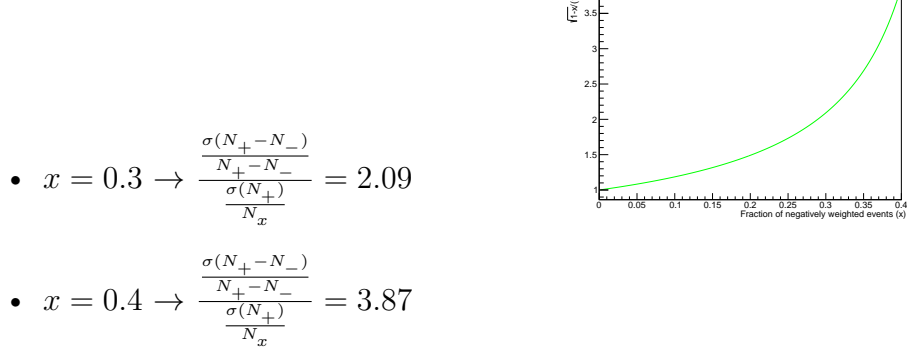
For the signal  $tHq$   $2\ell + 1\tau_{\text{had}}$  MC signal sample the fraction of negative weights is between 0.3 and 0.4 depending on the production used.

- $x = 0.3 \rightarrow \frac{\sigma(N_+ - N_-)}{N_+ - N_-} = \frac{1}{0.2} \frac{\sigma_n}{N} = 5.0 \frac{\sigma_n}{N}$
- $x = 0.4 \rightarrow \frac{\sigma(N_+ - N_-)}{N_+ - N_-} = \frac{1}{0.4} \frac{\sigma_n}{N} = 2.5 \frac{\sigma_n}{N}$

The uncertainty of the effective number of events can be compared to that of using only the positively weighted events. If the two fractional uncertainties are divided:

$$\frac{\frac{\sigma(N_+ - N_-)}{N_+ - N_-}}{\frac{\sigma(N_+)}{N_x}} = \frac{\frac{1}{1-2x} \frac{\sigma_n}{N}}{\frac{1}{\sqrt{(1-x)N}}} = \frac{\sqrt{1-x} \sigma_n}{1-2x} \frac{1}{N} = \frac{\sqrt{1-x}}{1-2x}$$

In the range of  $x$  values for the  $2\ell + 1\tau_{\text{had}}$  simulated signal events.



In Figure A.1, several  $\Delta R$  distributions generated using all the events and just the positively weighted ones. As expected, the uncertainty bands are bigger for the 'All events' than for the 'Positive events'. These histograms were produced to verify that using only the events with positive weights in the training of the BDT for lepton assignment in the SS scenario (Section 6.4.3) was not biasing the result. The size of the error bands is calculated by ROOT as the square root of the quadratic sum of the weights, as explained below.

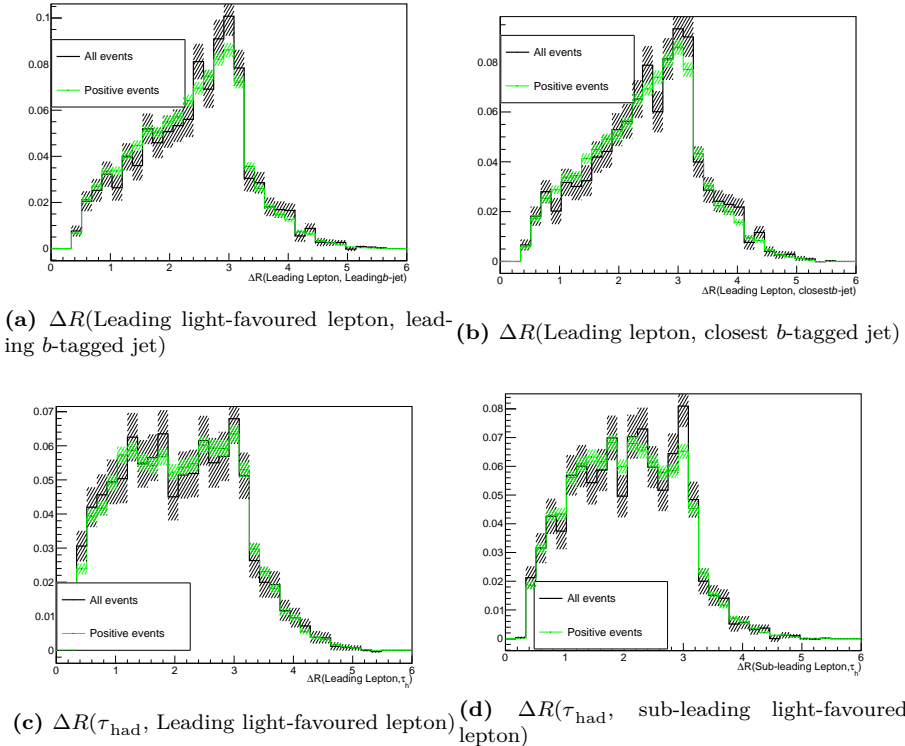


**Figure A.1:** Some normalised distributions for all the signal events in the  $2\ell \text{SS} + 1\tau_{\text{had}}$  (black) and just the positively weighted events (green). For each bin, the error band is calculated as the square root of the quadratic sum of the weights.

### A.2.1 Errors in binned histograms

If a bin of a histogram has  $n$  entries of weighted events  $w_i$  with  $i = 1, 2, \dots, n$ , the size of the bar is  $\sum_{i=1}^n w_i$ . Therefore, the error of that bar is

$$\sqrt{\sum_{i=1}^n w_i^2} \quad (\text{A.1})$$

This expression for the error of a bin in a histogram is based on error propagation and intrinsic poissonian statistics only. The variance, i.e. the error on the weighted number of events" in that bin, is given by error propagation:

$$V\left(\sum_{i=1}^n w_i\right) = \sqrt{\left(\sum_{i=1}^n w_i^2\right)^2} = \sum_{i=1}^n w_i^2 = \sum_{i=1}^n V(w_i)$$

The variance of the weight  $w_i$ ,  $V(w_i)$ , is determined only by the statistical fluctuation of the number of events considered:  $V(w_i) = w_i^2$ .

### A.3 Negative weights in MVA methods

Events coming from the MC generator can be produced with (unphysical) negative weights in some phase-space regions. Such occurrences are frequently inconvenient to deal with, and whether or not they are handled effectively is dependent on the MVA method’s actual implementation. Within the ROOT TMVA library, probability and multi-dimensional probability density estimators, as well as BDTs, are among the methods that correctly include occurrences with negative weights. In cases where a method does not properly treat events with negative weights, it is advisable to ignore such events for the training but to include them in the performance evaluation to not bias the results.

# Appendix B

## Boosted Decision Trees

A boosted decision tree, typically referred just by its acronym BDT, is a supervised<sup>1</sup> machine learning (ML) technique used for classification. The analysis presented in this thesis uses several BDTs. Both the light lepton origin assignment (Section 6.4.3) and the signal to background separation (Section 6.6.3) are based on a BDT. This tool is applied in more scenarios within within ATLAS. In the  $b$ -tagging, for instance, a BDT is trained to discriminate  $b$ -jets from light-jets [167].

### B.1 How does a BDT work?

A BDT is an ensamble of decision trees. A decision tree is a map of possible results of related decisions. A decision tree takes a set of input features and splits input data recursively based on those features. This results in a tree structure that resembles that of a flow charts with a decision or split at each node. The last level of the trees are the so called leaves and each represents a class. An example of a tree can be seen on Figure B.1, where an event is classified in one of the two categories following a set of yes-no questions.

Boosting is a technique for turning numerous weak classifiers (trees in this case) into a powerful one. Each tree is created iteratively depending on the prior ones. The output of each tree ( $h_t(x)$ ) is given a weight ( $w_t$ ) relative to its accuracy. The ensamble output is the weighted sum

$$\hat{y}(x) = \sum_t w_t h_t(x) \quad (\text{B.1})$$

---

<sup>1</sup>Supervised learning means that the data used in the training is labeled.

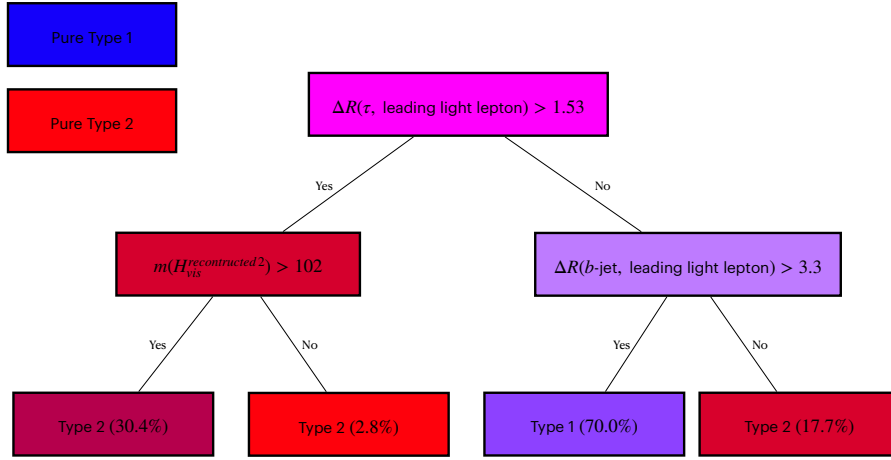


**Figure B.1:** Example of a decision tree with three nodes. This particular example corresponds to one of the trees in the BDT for the light lepton origin assignment (see Section 6.4.3). The color of the boxes represents the purity on Type 1 or Type 2 events that arrive to each node.

where  $t$  run over the trees. The goal of the boosting is to minimise an objective function

$$O(x) = \sum_i l(\hat{y}_i, y_i) + \sum_t \Omega(f_t) \quad (\text{B.2})$$

where  $l(\hat{y}_i, y_i)$  is the loss function (the distance between the truth and the prediction of the  $i^{th}$  sample) and  $\Omega(f_t)$  is the regularisation function (penalises the complexity of the  $t^{th}$  tree).

There are several types of boosting for BDTs. Some of the most common are AdaBoost, Gradient Boosting and XGBoost. The later, which stands for “eXtreme Gradient Boosting”, is the used in this work and its details can be found in reference [168].

### B.1.1 Training

For a ML algorithm to train means to learn or determine good values for all the weights within that model. To do so, the algorithm takes the labelled data and fits the model. For instance, for the signal discrimination, the ML model takes al the MC samples, where all the events are labeled either as signal or background events. A renormalisation can take place if needed (see comment below). Apart from the data, the model also needs a set of variables that have some power to discriminate between our categories. A condition on one discriminant variable is set on each node of the BDT to split the phase space into two parts. The aim of the training is to find

the optimal cut in each node so that after it the separation between the categories is maximised, i.e. one part is enriched in background and the other in signal. This is done in a loop over all discriminating variables and trying to test as many as possible values for each cut (the default in TMVA is trying 20 values for each variable). The best splitting is defined on the basis of the splitting index, which works as a measure of inequality because we want to measure the inequality between the two categories in each split node. A low splitting index value means a high inequality between the classes, i.e. high purity. The best cut is defined as the one that yields the highest splitting index difference between the parent node and the two children node (each weighted by the total number of events in the corresponding block). Then it is possible keep splitting blocks until a stopping requirement is satisfied. A single tree is a very weak classifier because it is very sensitive to statistical fluctuations in the training MC sample.

### Internal reweight of events in training sample

Sometimes, MC generators may provide event weights which may turn out to be extremely small or very high. To avoid artefacts, TMVA can renormalise the signal and background training weights internally so that their respective sums of effective (weighted) events are equal. By doing this, the performance of the BDT can be improved since some classifiers are sensitive to the relative amount of each category (Type1/Type2 or signal/background) in the training data. While for the lepton assignment this renormalisation does not play an important role (the amount of Type1 and Type2 signal events is similar), for the  $tHq$  signal discrimination the signal sample in the training test has to be reweighted.

#### B.1.1.1 Loss function

#### B.1.1.2 Overtraining

Let's consider a ML model  $f(x|\theta)$ , where  $x$  are the data points used as input and  $\theta$  the tuneable parameters of the model. The function  $f(x|\theta)$  outputs the prediction of the model. The parameters  $\theta$  of the model are tuned during the training process using a training set ( $\mathcal{T}$ ). The true output ( $y$ ) of the elements in  $\mathcal{T}$ . When successful, the training finds the  $\theta$  that performs as good as possible on new, unseen, data.

For a given  $f(x|\theta)$  model, the training error,  $\text{err}(\mathcal{T})$ , is defined by [169]:

$$\text{err}(\mathcal{T}) = \frac{1}{N_t} \sum_{n=1}^{N_t} L(y_n, f(x_n|\theta)) \quad (\text{B.3})$$

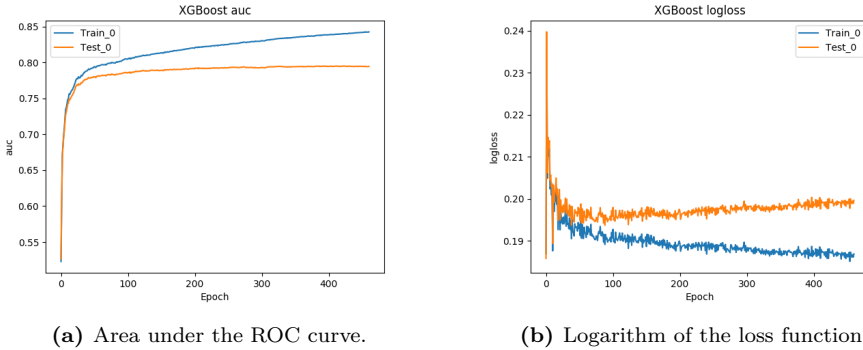


**Figure B.2:** Example of the evolution of the BDT metrics when overtraining occurs. The x-axis shows the training iteration.

where  $N_t$  is the number of events used for the training and  $L$  the chosen loss function and  $x_n$  and  $y_n$  the points in the training set.

The  $\text{err}(\mathcal{T})$  is a poor estimator of the model's performance on new, data. It usually decreases as the number of training cycles increases, and it can begin to adapt to noise in the training data. When this happens the training error continues to decrease but the error on the data outside of the training set starts increasing, jeopardising the general performance of the model. This effect is the so called overfitting or overtraining.

Overtraining occurs when a ML model can accurately predict training examples but is unable to generalise<sup>2</sup> to new data. When overtraining takes place, the ML model has learnt the details of the training data to an extent in which these knowledge do not reflect the behaviour of the test sample. This results in poor field performance.

Figure B.2 shows how an overtrained BDT evolves. In B.2a can be seen that as the training of the BDT continues, the ability of the model to classify the events in  $\mathcal{T}$  (blue) improves while for the data in the test sample (orange) it doesn't. This means that the model is not generalising properly. With the plot of the loss function (Figure B.2b) can be seen how the error of the test data slightly increases while for the training samples is strongly reduced.

When tested on the training sample, overtraining results in an apparent improvement in classification or regression performance over the objectively achievable one, but an effective performance loss when measured on an independent test sample (even though, there is a risk that it can still happen even if we use separate test data). Until deployed to real unseen data, there

---

<sup>2</sup>By generalise is meant that the model recognises only those characteristics of the data that are general enough to also apply to some unseen data.

is a danger that overtraining will go unnoticed. This makes of overtraining one of the greatest dangers in ML. Other names for this phenomenon are overfitting and type III error.

Usually, this is a result of too little data or data that is too homogenous. Overtraining arises when there are too few degrees of freedom, because too many model parameters of an algorithm were adjusted to too few data points. Not all MVA methods are equally sensible to overtraining. While Fisher discriminant hardly suffers from it, BDTs usually suffer from at least partial overtraining, owing to their large number of nodes. Nevertheless, for the BDTs some countermeasures can be applied to preserve the ability to generalise:

- Never test the model on the data used for the training.
- The number of nodes in boosted decision trees can be reduced by removing insignificant ones (“tree pruning”). There are two types, pre-pruning and post-pruning
  - Pre-pruning: Refers to the early stopping of the growth of the decision tree
  - Post-pruning: Allows the decision tree model to grow to its full depth, then removes the tree branches to prevent the model from overfitting
- Cross validation is a powerful technique to use all the data for training at the same time that all the data for testing is employed while avoiding overfitting. This method is based in cleverly iterating the test and training split around and it is described in Section B.3.

### B.1.2 Evaluation / Validation

### B.1.3 Application

## B.2 Treatment of negative weights

## B.3 Cross validation and $k$ -folding

Cross validation is a technique consisting in training several ML models on different subsets of the input data and evaluated on the complementary subset of the data. The goal cross validation is to estimate the performance

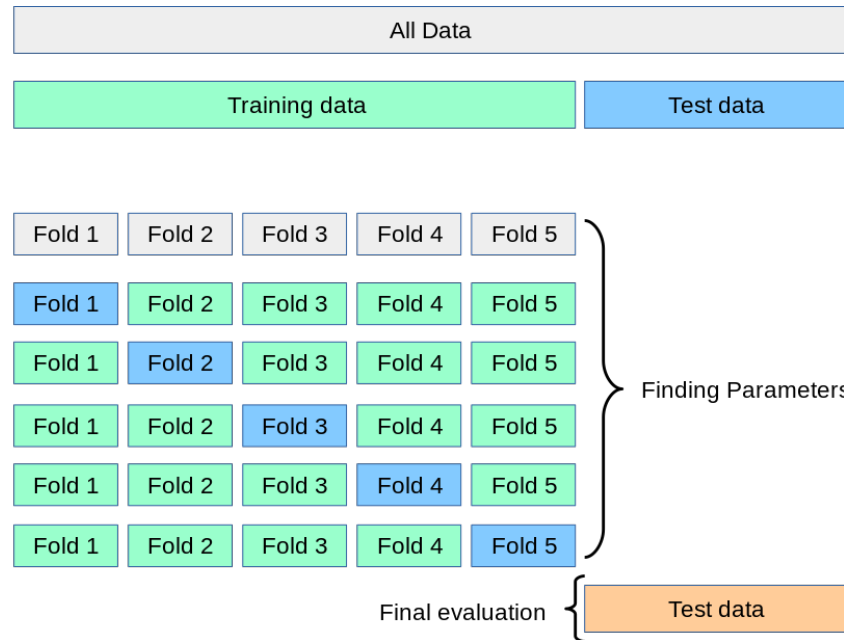


**Figure B.3:** Illustration of  $k$ -folding cross validation using 5 folds.

of a machine learning model. It can identify overfitting or recognise the failure of the model to generalise a pattern.

One particular method to do this is the  $k$ -folding. It consists on splitting the input data into  $k \in \mathcal{N}$  equally-sized subsets. Each of these is known as fold. With this procedure the ML model is trained  $k$  times. For each train  $k - 1$  folds are used as training set and the non-used fold is the subset of date where the evaluation takes place. All folds are used once as test sample and  $k - 1$  times in the train sample.

$k$ -folding cross validation resample is of particular interest when the data available is limited because, by using it, all events are used in the training phase. It generally results in a less biased or less optimistic estimate of the model skill than other methods, such as a simple train/test split.

Note that when the score of the model is applied, each event gets the score that was assigned when it was used as test event. Not doing this would bias the model.



# Abbreviations

Acronym	Meaning
AD	Antiproton Decelerator
ALICE	A Large Ion Collider Experiment
ATLAS	A Toroidal LArge AparatuS
AWAKE	Advanced Proton Driven Plasma Wakefield Acceleration Experiment
CERN	European Organization for Nuclear Research
CMS	Compact Muon Solenoid
CP	Charge conjugation Parity
CSC	Cathode-Strip Chambers
DAQ	Data Acquisition
ECAL	Electromagnetic Calorimeter
EF	Event Filter
EM	Electromagnetic
EW	Electro Weak
EWSB	Electroweak Symmetry Breaking
FASER	ForwArd Search ExpeRiment
FCAL	Forward calorimeter
FTK	Fast TracKer
GR	General Relativity
HCAL	Hadronic Calorimeter
HLT	High Level Trigger
IBL	Insertable B-Layer
IP	Interaction Point

Acronym	Meaning
IR	Insertion Regions
ISOLDE	On-Line Isotope Mass Separator
ITk	Inner Tracker
LAr	Liquid Argon
LCG	LHC Computing Grid
LEIR	Low Energy Ion Ring
LEP	Large Electron-Positron
LHC	Large Hadron Collider
LHCb	The Large Hadron Collider Beauty
LHCf	Large Hadron Collider forward
LINAC2	Linear Accelerator 2
LINAC3	Linear Accelerator 3
LINAC4	Linear Accelerator 4
LO	Leading Order
LVL1	Level-1 Trigger
LVL2	Level-2 Trigger
MATHUSLA	Massive Timing Hodoscope for Ultra Stable neutrAL pArticles
MDT	Monitored Drift Tube
MoEDAL	Monopole and exotic particle detector at the LHC
MS	Muon Spectrometer
NLO	Next-to-Leading Order
NNLO	Next-to-Next-to-Leading Order
PDF	Parton Distribution Function
PS	Proton Synchrotron
PSB	Proton Synchrotron Booster
QCD	Quantum Chromodynamics
QED	Quantum Electrodynamics
QFT	Quantum Field Theory

Acronym	Meaning
RF	Radio Frequency
ROD	ReadOut Drivers
RoI	Regions of interest
ROS	ReadOut Systems
RPC	Resistive Plate Chambers
SCT	Semiconductor Tracker
SFO	Sub-Farm Output
SM	Standar Model
SPS	Super Proton Synchrotron
SSB	Spontaneus Symmetry Breakin
SSC	Superconducting Super Collider
SUSY	Supersimmetry
TGC	Thin Gap Chambers
TI	Transfer Injection

# Bibliography

- <sup>1</sup>G. Aad et al., *Observation of a new particle in the search for the Standard Model Higgs boson with the ATLAS detector at the LHC*, *Phys. Lett. B* **716** (2012) 1–29 (2012) (cit. on pp. v, 43, 54).
- <sup>2</sup>S. Chatrchyan et al., *Observation of a New Boson at a Mass of 125 GeV with the CMS Experiment at the LHC*, *Phys. Lett. B* **716** (2012) 30–61 (2012) (cit. on pp. v, 43, 54).
- <sup>3</sup>F. Demartin, F. Maltoni, K. Mawatari and M. Zaro, *Higgs production in association with a single top quark at the LHC*, *Eur. Phys. J. C* **75** (2015) 267 (2015) (cit. on pp. v, 49–51).
- <sup>4</sup>D. de Florian et al., *Handbook of LHC Higgs Cross Sections: 4. Deciphering the Nature of the Higgs Sector*, **2/2017** (2016) (2016) (cit. on pp. vi, 45, 46).
- <sup>5</sup>Online Etymology Dictionary, "Physics", (2022) <https://www.etymonline.com/word/physics> (visited on 20/01/2022) (cit. on p. 1).
- <sup>6</sup>Perseus Digital Library, "fusiko", (2022) <https://www.perseus.tufts.edu/hopper/text?doc=Perseus:text:1999.04.0057:entry=fusiko/s> (visited on 20/01/2022) (cit. on p. 1).
- <sup>7</sup>C Singer, *A Short History of Science to the Nineteenth Century*, p. 35. (Streeter Press, 2008) (cit. on p. 1).
- <sup>8</sup>C. C. W. Taylor et al., *The atomists, leucippus and democritus: fragments: a text and translation with a commentary*, Vol. 5 (University of Toronto Press, 2010) (cit. on p. 1).
- <sup>9</sup>O. Leaman, *Key concepts in eastern philosophy* (Routledge, 2002) (cit. on p. 1).
- <sup>10</sup>A. Purcell, *Go on a particle quest at the first CERN webfest. Le premier webfest du CERN se lance à la conquête des particules*, (2012) 10 (2012) (cit. on p. 2).

- <sup>11</sup>A. Einstein, *The Foundation of the General Theory of Relativity*, Annalen Phys. **49** (1916) 769–822, edited by J.-P. Hsu and D. Fine (1916) (cit. on p. 2).
- <sup>12</sup>M. Aaboud et al., *Measurement of the W-boson mass in pp collisions at  $\sqrt{s} = 7$  TeV with the ATLAS detector*, Eur. Phys. J. C **78** (2018) 110, [Erratum: Eur.Phys.J.C 78, 898 (2018)] (2018) (cit. on p. 3).
- <sup>13</sup>S. Schael et al., *Precision electroweak measurements on the Z resonance*, Phys. Rept. **427** (2006) 257–454 (2006) (cit. on p. 3).
- <sup>14</sup>F. Englert and R. Brout, *Broken Symmetry and the Mass of Gauge Vector Mesons*, Phys. Rev. Lett. **13** (1964) 321–323, edited by J. C. Taylor (1964) (cit. on p. 3).
- <sup>15</sup>P. W. Higgs, *Broken Symmetries and the Masses of Gauge Bosons*, Phys. Rev. Lett. **13** (1964) 508–509, edited by J. C. Taylor (1964) (cit. on p. 3).
- <sup>16</sup>P. A. M. Dirac, *On the theory of quantum mechanics*, Proceedings of the Royal Society of London. Series A, Containing Papers of a Mathematical and Physical Character **112** (1926) 661–677 (1926) (cit. on p. 3).
- <sup>17</sup>R. Aaij et al., *Observation of a narrow pentaquark state,  $P_c(4312)^+$ , and of two-peak structure of the  $P_c(4450)^+$* , Phys. Rev. Lett. **122** (2019) 222001 (2019) (cit. on p. 4).
- <sup>18</sup>A. Pich, ‘The Standard model of electroweak interactions’, 2006 European School of High-Energy Physics (2007) 1 (cit. on pp. 4, 16).
- <sup>19</sup>E. Noether, *Invariante variationsprobleme*, ger, Nachrichten von der Gesellschaft der Wissenschaften zu Göttingen, Mathematisch-Physikalische Klasse **1918** (1918) 235–257 (1918) (cit. on p. 6).
- <sup>20</sup>C. A. Moura and F. Rossi-Torres, *Searches for Violation of CPT Symmetry and Lorentz Invariance with Astrophysical Neutrinos*, Universe **8** (2022) 42 (2022) (cit. on p. 9).
- <sup>21</sup>J. S. Bell, *Time reversal in field theory*, Proc. Roy. Soc. Lond. A **231** (1955) 479–495 (1955) (cit. on p. 9).
- <sup>22</sup>R. F. Streater and A. S. Wightman, *PCT, spin and statistics, and all that* (1989) (cit. on p. 9).

- <sup>23</sup>T. D. Lee and C.-N. Yang,  
*Question of Parity Conservation in Weak Interactions*,  
Phys. Rev. **104** (1956) 254–258 (1956) (cit. on p. 10).
- <sup>24</sup>C. S. Wu, E. Ambler, R. W. Hayward, D. D. Hoppes and R. P. Hudson,  
*Experimental Test of Parity Conservation in  $\beta$  Decay*,  
Phys. Rev. **105** (1957) 1413–1414 (1957) (cit. on p. 10).
- <sup>25</sup>J. H. Christenson, J. W. Cronin, V. L. Fitch and R. Turlay,  
*Evidence for the  $2\pi$  Decay of the  $K_2^0$  Meson*,  
Phys. Rev. Lett. **13** (1964) 138–140 (1964) (cit. on p. 10).
- <sup>26</sup>L.-L. Chau and W.-Y. Keung,  
*Comments on the Parametrization of the Kobayashi-Maskawa Matrix*,  
Phys. Rev. Lett. **53** (1984) 1802 (1984) (cit. on p. 11).
- <sup>27</sup>P. A. Zyla et al., *Review of Particle Physics*,  
PTEP **2020** (2020) 083C01 (2020) (cit. on p. 12).
- <sup>28</sup>A. M. Sirunyan et al.,  
*Measurement of the weak mixing angle using the forward-backward asymmetry of Drell-Yan events in pp collisions at 8 TeV*,  
Eur. Phys. J. C **78** (2018) 701 (2018) (cit. on p. 14).
- <sup>29</sup>O. W. Greenberg, *Spin and Unitary Spin Independence in a Paraquark Model of Baryons and Mesons*, Phys. Rev. Lett. **13** (1964) 598–602 (1964) (cit. on p. 15).
- <sup>30</sup>D. D. Ryutov, *Using Plasma Physics to Weigh the Photon*,  
Plasma Phys. Control. Fusion **49** (2007) B429 (2007) (cit. on p. 19).
- <sup>31</sup>F. J. Yndurain, *Limits on the mass of the gluon*,  
Phys. Lett. B **345** (1995) 524–526 (1995) (cit. on p. 19).
- <sup>32</sup>J. Goldstone, A. Salam and S. Weinberg, *Broken Symmetries*,  
Phys. Rev. **127** (1962) 965–970 (1962) (cit. on p. 21).
- <sup>33</sup>D. M. Webber et al., *Measurement of the Positive Muon Lifetime and Determination of the Fermi Constant to Part-per-Million Precision*,  
Phys. Rev. Lett. **106** (2011) 041803 (2011) (cit. on p. 25).
- <sup>34</sup>M. Aker et al.,  
*Direct neutrino-mass measurement with sub-electronvolt sensitivity*,  
Nature Phys. **18** (2022) 160–166 (2022) (cit. on p. 26).
- <sup>35</sup>N. Aghanim et al., *Planck 2018 results. VI. Cosmological parameters*,  
Astron. Astrophys. **641** (2020) A6, [Erratum: Astron. Astrophys. 652, C4 (2021)] (2020) (cit. on p. 28).
- <sup>36</sup>S. Weinberg, *A New Light Boson?*, Phys. Rev. Lett. **40** (1978) 223–226 (1978) (cit. on p. 29).

- <sup>37</sup>F. Wilczek,  
*Problem of Strong P and T Invariance in the Presence of Instantons*,  
*Phys. Rev. Lett.* **40** (1978) 279–282 (1978) (cit. on p. 29).
- <sup>38</sup>V. C. Rubin and W. K. Ford Jr., *Rotation of the Andromeda Nebula from a Spectroscopic Survey of Emission Regions*,  
*Astrophys. J.* **159** (1970) 379–403 (1970) (cit. on p. 29).
- <sup>39</sup>A. N. Taylor, S. Dye, T. J. Broadhurst, N. Benitez and E. van Kampen,  
*Gravitational lens magnification and the mass of abell 1689*,  
*Astrophys. J.* **501** (1998) 539 (1998) (cit. on pp. 29, 31).
- <sup>40</sup>P. A. R. Ade et al., *Planck 2015 results. XIII. Cosmological parameters*,  
*Astron. Astrophys.* **594** (2016) A13 (2016) (cit. on p. 29).
- <sup>41</sup>M. Banner et al., *Observation of Single Isolated Electrons of High Transverse Momentum in Events with Missing Transverse Energy at the CERN anti-p p Collider*, *Phys. Lett. B* **122** (1983) 476–485 (1983) (cit. on p. 30).
- <sup>42</sup>G. Arnison et al., *Experimental Observation of Lepton Pairs of Invariant Mass Around 95-GeV/c\*\*2 at the CERN SPS Collider*,  
*Phys. Lett. B* **126** (1983) 398–410 (1983) (cit. on p. 30).
- <sup>43</sup>I. Zurbano Fernandez et al., *High-Luminosity Large Hadron Collider (HL-LHC): Technical design report*,  
**10/2020** (2020), edited by I. Béjar Alonso et al. (2020) (cit. on p. 30).
- <sup>44</sup>M. Kobayashi and T. Maskawa,  
*CP Violation in the Renormalizable Theory of Weak Interaction*,  
*Prog. Theor. Phys.* **49** (1973) 652–657 (1973) (cit. on p. 32).
- <sup>45</sup>J. E. Augustin et al.,  
*Discovery of a Narrow Resonance in e<sup>+</sup>e<sup>-</sup> Annihilation*,  
*Phys. Rev. Lett.* **33** (1974) 1406–1408 (1974) (cit. on p. 32).
- <sup>46</sup>S. W. Herb et al., *Observation of a Dimuon Resonance at 9.5-GeV in 400-GeV Proton-Nucleus Collisions*,  
*Phys. Rev. Lett.* **39** (1977) 252–255 (1977) (cit. on p. 32).
- <sup>47</sup>F. Abe et al., *Observation of top quark production in p̄p collisions*,  
*Phys. Rev. Lett.* **74** (1995) 2626–2631 (1995) (cit. on p. 32).
- <sup>48</sup>S. Abachi et al., *Observation of the top quark*,  
*Phys. Rev. Lett.* **74** (1995) 2632–2637 (1995) (cit. on p. 32).
- <sup>49</sup>J. Jimenez Pena and C. Nellist,  
*Top quark mass summary plots June 2022*, tech. rep.,  
All figures including auxiliary figures are available at  
<https://atlas.web.cern.ch/Atlas/GROUPS/PHYSICS/PUBNOTES/ATL-PHYS-PUB-2022-032>: CERN, 2022 (cit. on pp. 32, 34).

- <sup>50</sup>S. Amoroso et al.,  
*Strategy for ATLAS top quark mass measurements: 2021-2023*,  
 tech. rep., CERN, 2020 (cit. on pp. 32, 33).
- <sup>51</sup>Particle Data Group Web Page, *top-quark Mass (Direct Measurements)*,  
 (2022) <https://pdglive.lbl.gov/DataBlock.action?node=Q007TP>  
 (visited on 22/01/2022) (cit. on p. 33).
- <sup>52</sup>M. Aaboud et al.,  
*Measurement of the top quark mass in the  $t\bar{t} \rightarrow \text{lepton+jets}$  channel  
 from  $\sqrt{s} = 8$  TeV ATLAS data and combination with previous results*,  
*Eur. Phys. J. C* **79** (2019) 290 (2019) (cit. on p. 33).
- <sup>53</sup>A. M. Sirunyan et al.,  
*Measurement of the Jet Mass Distribution and Top Quark Mass in  
 Hadronic Decays of Boosted Top Quarks in  $pp$  Collisions at  $\sqrt{s} = 13$  TeV*,  
*Phys. Rev. Lett.* **124** (2020) 202001 (2020) (cit. on p. 33).
- <sup>54</sup>Combination of CDF and D0 results on the mass of the top quark using  
 up  $9.7 \text{ fb}^{-1}$  at the Tevatron, (2016) (2016) (cit. on p. 33).
- <sup>55</sup>M. Czakon and A. Ferroglia, *Top quark pair production at complete  
 NLO accuracy with NNLO+NNLL corrections in QCD*,  
*Chinese Physics C* **44** (2020) 083104 (2020) (cit. on p. 34).
- <sup>56</sup>P. Kant et al., *HatHor for single top-quark production: Updated  
 predictions and uncertainty estimates for single top-quark production in  
 hadronic collisions*, *Comput. Phys. Commun.* **191** (2015) 74–89 (2015)  
 (cit. on p. 37).
- <sup>57</sup>M. Aliev et al.,  
*HATHOR – HAdronic Top and Heavy quarks crOss section calculatoR*,  
*Comput. Phys. Commun.* **182** (2011) 1034–1046 (2011) (cit. on p. 37).
- <sup>58</sup>J. A. Aguilar-Saavedra,  
*Single top quark production at LHC with anomalous  $Wtb$  couplings*,  
*Nucl. Phys. B* **804** (2008) 160–192 (2008) (cit. on p. 38).
- <sup>59</sup>J. Butterworth et al., *PDF4LHC recommendations for LHC Run II*,  
*J. Phys. G* **43** (2016) 023001 (2016) (cit. on pp. 39, 71).
- <sup>60</sup>A. D. Martin, W. J. Stirling, R. S. Thorne and G. Watt,  
*Parton distributions for the LHC*, *Eur. Phys. J. C* **63** (2009) 189 (2009)  
 (cit. on pp. 39, 72).
- <sup>61</sup>A. D. Martin, W. J. Stirling, R. S. Thorne and G. Watt,  
*Uncertainties on  $\alpha_S$  in global PDF analyses and implications for  
 predicted hadronic cross sections*, *Eur. Phys. J. C* **64** (2009) 653–680  
 (2009) (cit. on p. 39).

- <sup>62</sup>H.-L. Lai et al., *New parton distributions for collider physics*, Phys. Rev. D **82** (2010) 074024 (2010) (cit. on p. 39).
- <sup>63</sup>R. D. Ball et al., *Parton distributions with QED corrections*, Nucl. Phys. B **877** (2013) 290–320 (2013) (cit. on p. 39).
- <sup>64</sup>Particle Data Group Web Page, *Higgs-boson Mass*, (2022) <https://pdglive.lbl.gov/DataBlock.action?node=S126M> (visited on 22/01/2022) (cit. on p. 43).
- <sup>65</sup>M. Aaboud et al., *Measurement of the Higgs boson mass in the  $H \rightarrow ZZ^* \rightarrow 4\ell$  and  $H \rightarrow \gamma\gamma$  channels with  $\sqrt{s} = 13$  TeV  $pp$  collisions using the ATLAS detector*, Phys. Lett. B **784** (2018) 345–366 (2018) (cit. on p. 43).
- <sup>66</sup>A. M. Sirunyan et al., *A measurement of the Higgs boson mass in the diphoton decay channel*, Phys. Lett. B **805** (2020) 135425 (2020) (cit. on p. 43).
- <sup>67</sup>F. Englert and R. Brout, *Broken symmetry and the mass of gauge vector mesons*, Phys. Rev. Lett. **13** (9 1964) 321–323 (1964) (cit. on p. 43).
- <sup>68</sup>P. W. Higgs, *Broken symmetries and the masses of gauge bosons*, Phys. Rev. Lett. **13** (16 1964) 508–509 (1964) (cit. on p. 43).
- <sup>69</sup>G. S. Guralnik, C. R. Hagen and T. W. B. Kibble, *Global conservation laws and massless particles*, Phys. Rev. Lett. **13** (20 1964) 585–587 (1964) (cit. on p. 43).
- <sup>70</sup>T. Aaltonen et al., *Combined search for the standard model Higgs boson decaying to a  $bb$  pair using the full CDF data set*, Phys. Rev. Lett. **109** (2012) 111802 (2012) (cit. on p. 43).
- <sup>71</sup>V. M. Abazov et al., *Combined Search for the Standard Model Higgs Boson Decaying to  $bb$  Using the D0 Run II Data Set*, Phys. Rev. Lett. **109** (2012) 121802 (2012) (cit. on p. 43).
- <sup>72</sup>B. Mellado Garcia, P. Musella, M. Grazzini and R. Harlander, *CERN Report 4: Part I Standard Model Predictions*, (2016) (2016) (cit. on p. 46).
- <sup>73</sup>M. Farina, C. Grojean, F. Maltoni, E. Salvioni and A. Thamm, *Lifting degeneracies in Higgs couplings using single top production in association with a Higgs boson*, JHEP **05** (2013) 022 (2013) (cit. on p. 48).
- <sup>74</sup>S. Biswas, E. Gabrielli and B. Mele, *Single top and Higgs associated production as a probe of the  $Htt$  coupling sign at the LHC*, JHEP **01** (2013) 088 (2013) (cit. on p. 48).

- <sup>75</sup>T. Appelquist and M. S. Chanowitz, *Unitarity Bound on the Scale of Fermion Mass Generation*, Phys. Rev. Lett. **59** (1987) 2405, [Erratum: Phys.Rev.Lett. 60, 1589 (1988)] (1987) (cit. on p. 48).
- <sup>76</sup>M. Aaboud et al., *Observation of Higgs boson production in association with a top quark pair at the LHC with the ATLAS detector*, Phys. Lett. B **784** (2018) 173–191 (2018) (cit. on p. 48).
- <sup>77</sup>K. Skovpen, ‘First observation of the  $t\bar{t}H$  process at CMS’, 11th International Workshop on Top Quark Physics (2018) (cit. on p. 48).
- <sup>78</sup>G. Aad et al., *Search for  $H \rightarrow \gamma\gamma$  produced in association with top quarks and constraints on the Yukawa coupling between the top quark and the Higgs boson using data taken at 7 TeV and 8 TeV with the ATLAS detector*, Phys. Lett. B **740** (2015) 222–242 (2015) (cit. on p. 49).
- <sup>79</sup>V. Khachatryan et al., *Search for the associated production of the Higgs boson with a top-quark pair*, JHEP **09** (2014) 087, [Erratum: JHEP 10, 106 (2014)] (2014) (cit. on p. 49).
- <sup>80</sup>T. M. P. Tait and C. P. Yuan, *Single top quark production as a window to physics beyond the standard model*, Phys. Rev. D **63** (2000) 014018 (2000) (cit. on p. 51).
- <sup>81</sup>S. Biswas, E. Gabrielli, F. Margaroli and B. Mele, *Direct constraints on the top-Higgs coupling from the 8 TeV LHC data*, JHEP **07** (2013) 073 (2013) (cit. on p. 51).
- <sup>82</sup>V. Khachatryan et al., *Search for the associated production of a Higgs boson with a single top quark in proton-proton collisions at  $\sqrt{s} = 8$  TeV*, JHEP **06** (2016) 177 (2016) (cit. on p. 51).
- <sup>83</sup>A. Airapetian et al., *ATLAS: Detector and physics performance technical design report. Volume 2*, (1999) (1999) (cit. on pp. 53, 94).
- <sup>84</sup>CERN Web Page, *Our Member States*, (2022) <https://home.web.cern.ch/about/who-we-are/our-governance/member-states> (visited on 11/01/2022) (cit. on p. 54).
- <sup>85</sup>T. Fazzini, G. Fidecaro, A. W. Merrison, H. Paul and A. V. Tollestrup, *Electron decay of the pion*, Phys. Rev. Lett. **1** (7 1958) 247–249 (1958) (cit. on p. 54).
- <sup>86</sup>F. J. Hasert et al., *Observation of Neutrino Like Interactions Without Muon Or Electron in the Gargamelle Neutrino Experiment*, Phys. Lett. B **46** (1973) 138–140 (1973) (cit. on p. 54).

- <sup>87</sup>P. M. Watkins, *Discovery of the w and 2 bosons*, *Contemporary Physics* **27** (1986) 291–324 (1986) (cit. on p. 54).
- <sup>88</sup>D. Decamp et al., *Determination of the Number of Light Neutrino Species*, *Phys. Lett. B* **231** (1989) 519–529 (1989) (cit. on p. 54).
- <sup>89</sup>G. Baur et al., *Production of anti-hydrogen*, *Phys. Lett. B* **368** (1996) 251–258 (1996) (cit. on p. 54).
- <sup>90</sup>G. D. Barr et al., *A New measurement of direct CP violation in the neutral kaon system*, *Phys. Lett. B* **317** (1993) 233–242 (1993) (cit. on p. 54).
- <sup>91</sup>V. Fanti et al., *A New measurement of direct CP violation in two pion decays of the neutral kaon*, *Phys. Lett. B* **465** (1999) 335–348 (1999) (cit. on p. 54).
- <sup>92</sup>R. Aaij et al., *Observation of J/ψ Resonances Consistent with Pentaquark States in  $\Lambda_b^0 \rightarrow J/\psi K^- p$  Decays*, *Phys. Rev. Lett.* **115** (2015) 072001 (2015) (cit. on p. 54).
- <sup>93</sup>S. Maury, *The Antiproton Decelerator: AD*, *Hyperfine Interact.* **109** (1997) 43–52 (1997) (cit. on p. 54).
- <sup>94</sup>R. Alemany et al., *Summary Report of Physics Beyond Colliders at CERN*, (2019), edited by J. Jaeckel, M. Lamont and C. Vallée (2019) (cit. on p. 54).
- <sup>95</sup>R. Catherall et al., *The ISOLDE facility*, *J. Phys. G* **44** (2017) 094002 (2017) (cit. on p. 54).
- <sup>96</sup>E. Gschwendtner et al., *AWAKE, The Advanced Proton Driven Plasma Wakefield Acceleration Experiment at CERN*, *Nucl. Instrum. Meth. A* **829** (2016) 76–82, edited by U. Dorda et al. (2016) (cit. on p. 54).
- <sup>97</sup>M. Aguilar et al., *The Alpha Magnetic Spectrometer (AMS) on the International Space Station. I: Results from the test flight on the space shuttle*, *Phys. Rept.* **366** (2002) 331–405, [Erratum: *Phys.Rept.* 380, 97–98 (2003)] (2002) (cit. on p. 55).
- <sup>98</sup>CERN Council holds special session on the Large Hadron Collider project, (1991) 3 p, Issued on 19 December 1991 (1991) (cit. on p. 55).
- <sup>99</sup>T. S. Pettersson and P Lefèvre, *The Large Hadron Collider: conceptual design*, tech. rep., 1995 (cit. on pp. 55, 57, 58).

- <sup>100</sup>S. Myers,  
*The LEP Collider, from design to approval and commissioning*,  
John Adams' memorial lecture, Delivered at CERN, 26 Nov 1990  
(CERN, Geneva, 1991) (cit. on p. 56).
- <sup>101</sup>B. Müller, J. Schukraft and B. Wysłouch,  
*First Results from Pb+Pb Collisions at the LHC*,  
[Annual Review of Nuclear and Particle Science 62 \(2012\) 361–386 \(2012\)](https://home.cern/science/accelerators/large-hadron-collider) (cit. on p. 56).
- <sup>102</sup>CERN Web Page, *The Large Hadron Collider*, (2022)  
<https://home.cern/science/accelerators/large-hadron-collider> (visited on 11/01/2022) (cit. on p. 56).
- <sup>103</sup>R. Steerenberg et al., ‘Operation and performance of the cern large hadron collider during proton run 2’,  
[10th international particle accelerator conference \(2019\) MOPMP031](#) (cit. on p. 56).
- <sup>104</sup>by Rende Steerenberg and A. Schaeffer, *LHC Report: The LHC is full!*,  
[\(2018\) \(2018\)](#) (cit. on p. 56).
- <sup>105</sup>*8th International Conference on High-Energy Accelerators*,  
CERN (CERN, Geneva, 1971) (cit. on p. 57).
- <sup>106</sup>*LHC Machine*,  
[JINST 3 \(2008\) S08001](#), edited by L. Evans and P. Bryant (2008)  
(cit. on pp. 57, 59).
- <sup>107</sup>*Radiofrequency cavities*, [\(2012\) \(2012\)](#) (cit. on p. 58).
- <sup>108</sup>L Lari, H Gaillard and V Mertens,  
*Scheduling the installation of the LHC injection lines*, tech. rep.,  
CERN, 2004 (cit. on p. 59).
- <sup>109</sup>G. Aad et al.,  
*The ATLAS Experiment at the CERN Large Hadron Collider*,  
[JINST 3 \(2008\) S08003 \(2008\)](#) (cit. on pp. 59, 77, 81, 82, 86, 87).
- <sup>110</sup>S. Chatrchyan et al., *The CMS Experiment at the CERN LHC*,  
[JINST 3 \(2008\) S08004 \(2008\)](#) (cit. on p. 60).
- <sup>111</sup>A. A. Alves Jr. et al., *The LHCb Detector at the LHC*,  
[JINST 3 \(2008\) S08005 \(2008\)](#) (cit. on p. 61).
- <sup>112</sup>K. Aamodt et al., *The ALICE experiment at the CERN LHC*,  
[JINST 3 \(2008\) S08002 \(2008\)](#) (cit. on p. 61).
- <sup>113</sup>O. Adriani et al.,  
*The LHCf detector at the CERN Large Hadron Collider*,  
[JINST 3 \(2008\) S08006 \(2008\)](#) (cit. on p. 61).

- <sup>114</sup>C. Alpigiani et al., *A Letter of Intent for MATHUSLA: A Dedicated Displaced Vertex Detector above ATLAS or CMS.*, (2018) (2018) (cit. on p. 61).
- <sup>115</sup>J. H. Yoo, *The milliQan Experiment: Search for milli-charged Particles at the LHC*, PoS ICHEP2018 (2018) 520. 4 p, proceeding for ICHEP 2018 SEOUL, International Conference on High Energy Physics, 4-11 July 2018, SEOUL, KOREA (2018) (cit. on p. 61).
- <sup>116</sup>V. A. Mitsou, *The MoEDAL experiment at the LHC: status and results*, J. Phys. Conf. Ser. **873** (2017) 012010, edited by B. Grzadkowski, J. Kalinowski and M. Krawczyk (2017) (cit. on p. 61).
- <sup>117</sup>G. Anelli et al.,  
*The TOTEM experiment at the CERN Large Hadron Collider*, JINST **3** (2008) S08007 (2008) (cit. on p. 61).
- <sup>118</sup>A. Ariga et al.,  
*Letter of Intent for FASER: ForwArd Search ExpeRiment at the LHC*, (2018) (2018) (cit. on p. 61).
- <sup>119</sup>*LHC computing Grid. Technical design report*, (2005), edited by I. Bird et al. (2005) (cit. on p. 62).
- <sup>120</sup>WLCG Web Page, *Resources*, (2022)  
<https://wlcg-public.web.cern.ch/resources> (visited on 31/01/2022) (cit. on p. 63).
- <sup>121</sup>*ATLAS computing: Technical design report*, (2005), edited by G. Duckeck et al. (2005) (cit. on p. 62).
- <sup>122</sup>WLCG Web Page, *Tier centres*, (2022)  
<https://wlcg-public.web.cern.ch/tier-centres> (visited on 31/01/2022) (cit. on pp. 62, 64).
- <sup>123</sup>W. Herr and B Muratori, *Concept of luminosity*, (2006) (2006) (cit. on pp. 65, 66).
- <sup>124</sup>A. Hoecker, ‘Physics at the LHC Run-2 and Beyond’, 2016 European School of High-Energy Physics (2016) (cit. on pp. 65, 66, 73).
- <sup>125</sup>M. Aaboud et al., *Luminosity determination in pp collisions at  $\sqrt{s} = 8$  TeV using the ATLAS detector at the LHC*, Eur. Phys. J. C **76** (2016) 653 (2016) (cit. on p. 65).
- <sup>126</sup>G. Aad et al., *ATLAS data quality operations and performance for 2015–2018 data-taking*, JINST **15** (2020) P04003 (2020) (cit. on p. 67).
- <sup>127</sup>*Luminosity determination in pp collisions at  $\sqrt{s} = 13$  TeV using the ATLAS detector at the LHC*, tech. rep., CERN, 2019 (cit. on p. 67).

- <sup>128</sup>F. S. Cafagna, *Latest results for Proton-proton Cross Section Measurements with the TOTEM experiment at LHC*, PoS ICRC2019 (2021) 207 (2021) (cit. on p. 70).
- <sup>129</sup>Particle Data Group Web Page, *Data files and plots of cross-sections and related quantities for hadrons*, (2022) <https://pdg.lbl.gov/2021/hadronic-xsections/> (visited on 08/02/2022) (cit. on p. 70).
- <sup>130</sup>*Shrek*, 2001 (cit. on p. 75).
- <sup>131</sup>G. Aad et al., *Measurements of the Higgs boson production and decay rates and constraints on its couplings from a combined ATLAS and CMS analysis of the LHC pp collision data at  $\sqrt{s} = 7$  and 8 TeV*, JHEP 08 (2016) 045 (2016) (cit. on p. 74).
- <sup>132</sup>G. Aad et al., *Measurement of the top quark-pair production cross section with ATLAS in pp collisions at  $\sqrt{s} = 7$  TeV*, Eur. Phys. J. C 71 (2011) 1577 (2011) (cit. on p. 74).
- <sup>133</sup>G. Aad et al., *Evidence for Electroweak Production of  $W^\pm W^\pm jj$  in pp Collisions at  $\sqrt{s} = 8$  TeV with the ATLAS Detector*, Phys. Rev. Lett. 113 (2014) 141803 (2014) (cit. on p. 74).
- <sup>134</sup>M. Aaboud et al., *Evidence for light-by-light scattering in heavy-ion collisions with the ATLAS detector at the LHC*, Nature Phys. 13 (2017) 852–858 (2017) (cit. on p. 74).
- <sup>135</sup>M. Aaboud et al., *Search for the standard model Higgs boson produced in association with top quarks and decaying into a bb pair in pp collisions at  $\sqrt{s} = 13$  TeV with the ATLAS detector*, Phys. Rev. D 97 (2018) 072016 (2018) (cit. on p. 74).
- <sup>136</sup>M. Aaboud et al., *Observation of  $H \rightarrow b\bar{b}$  decays and VH production with the ATLAS detector*, Phys. Lett. B 786 (2018) 59–86 (2018) (cit. on p. 74).
- <sup>137</sup>S. Amoroso, *Precision measurements at the LHC*, tech. rep., CERN, 2020 (cit. on p. 76).
- <sup>138</sup>H. Pacey, *EW SUSY Production at the LHC*, tech. rep., CERN, 2021 (cit. on p. 76).
- <sup>139</sup>S. Das Bakshi, J. Chakrabortty, C. Englert, M. Spannowsky and P. Stylianou, *CP Violation at atlas in effective field theory*, Phys. Rev. D 103 (5 2021) 055008 (2021) (cit. on p. 76).
- <sup>140</sup>B. T. Carlson, *Dark Matter searches with the ATLAS detector*, (2020) (2020) (cit. on p. 76).

- <sup>141</sup>J. L. Pinfold, *ATLAS and astroparticle physics*, Nucl. Phys. B Proc. Suppl. **175-176** (2008) 25–32, edited by K. S. Cheng et al. (2008) (cit. on p. 76).
- <sup>142</sup>N. D. Brett et al., *Discovery Reach for Black Hole Production*, (2009) (2009) (cit. on p. 76).
- <sup>143</sup>*ATLAS inner detector: Technical Design Report, 1*, Technical design report. ATLAS (CERN, Geneva, 1997) (cit. on p. 77).
- <sup>144</sup>G. Aad et al., *The ATLAS Inner Detector commissioning and calibration*, Eur. Phys. J. C **70** (2010) 787–821 (2010) (cit. on p. 77).
- <sup>145</sup>M Capeans et al., *ATLAS Insertable B-Layer Technical Design Report*, tech. rep., 2010 (cit. on pp. 79, 80).
- <sup>146</sup>*Technical Design Report for the ATLAS Inner Tracker Pixel Detector*, tech. rep., CERN, 2017 (cit. on pp. 80, 82).
- <sup>147</sup>ATLAS Experiment Web Page, *Detector and Technology*, (2022) <https://atlas.cern/discover/detector> (visited on 02/02/2022) (cit. on pp. 80, 83, 86, 90, 91).
- <sup>148</sup>F. Cavallari, *Performance of calorimeters at the LHC*, Journal of Physics: Conference Series **293** (2011) 012001 (2011) (cit. on pp. 82, 85, 86).
- <sup>149</sup>C. Grupen and B. Shwartz, ‘Calorimetry’, *Particle detectors*, 2nd ed., Cambridge Monographs on Particle Physics, Nuclear Physics and Cosmology (Cambridge University Press, 2008) 230–272 (cit. on p. 84).
- <sup>150</sup>Particle Data Group Web Page,  $\pi^0$  Decay Modes, (2022) <https://pdglive.lbl.gov/DataBlock.action?node=Q007TP> (visited on 02/02/2022) (cit. on p. 85).
- <sup>151</sup>A. Tarek Abouelfadl Mohamed, ‘The lhc and the atlas experiment’, *Measurement of higgs boson production cross sections in the diphoton channel: with the full atlas run-2 data and constraints on anomalous higgs boson interactions* (Springer International Publishing, Cham, 2020) 61 (cit. on pp. 86, 87).
- <sup>152</sup>*ATLAS muon spectrometer: Technical design report*, (1997) (1997) (cit. on p. 87).
- <sup>153</sup>K. Ishii, *The ATLAS muon spectrometer*, PoS **HEP2001** (2001) 253, edited by D. o. Horváth, P. Lévai and A. Patkós (2001) (cit. on p. 88).
- <sup>154</sup>M Livan, *Monitored drift tubes in ATLAS*, tech. rep., CERN, 1996 (cit. on p. 88).

- <sup>155</sup>G. Cattani, *The resistive plate chambers of the ATLAS experiment: performance studies*, Journal of Physics: Conference Series **280** (2011) 012001 (2011) (cit. on p. 89).
- <sup>156</sup>K. Nagai, *Thin gap chambers in ATLAS*, Nucl. Instrum. Meth. A **384** (1996) 219–221, edited by F. Ferroni and P. Schlein (1996) (cit. on p. 89).
- <sup>157</sup>*ATLAS magnet system: Technical Design Report*, 1, Technical design report. ATLAS (CERN, Geneva, 1997) (cit. on pp. 90, 91).
- <sup>158</sup>*ATLAS high-level trigger, data acquisition and controls: Technical design report*, (2003) (2003) (cit. on pp. 92, 93).
- <sup>159</sup>G. Aad et al., *Performance of the ATLAS Trigger System in 2010*, Eur. Phys. J. C **72** (2012) 1849 (2012) (cit. on p. 92).
- <sup>160</sup>G. Aad et al., *Alignment of the ATLAS Inner Detector in Run-2*, Eur. Phys. J. C **80** (2020) 1194 (2020) (cit. on pp. 93, 95, 96).
- <sup>161</sup>G. Aad et al., *The ATLAS Simulation Infrastructure*, Eur. Phys. J. C **70** (2010) 823–874 (2010) (cit. on pp. 101, 102).
- <sup>162</sup>T. Gleisberg et al., *Event generation with SHERPA 1.1*, JHEP **02** (2009) 007 (2009) (cit. on p. 104).
- <sup>163</sup>P. Mato, *GAUDI-Architecture design document*, (1998) (1998) (cit. on p. 106).
- <sup>164</sup>G. Cowan, K. Cranmer, E. Gross and O. Vitells, *Asymptotic formulae for likelihood-based tests of new physics*, Eur. Phys. J. C **71** (2011) 1554 (2011) (cit. on p. 120).
- <sup>165</sup>L. Lista, ‘Practical Statistics for Particle Physicists’, 2016 European School of High-Energy Physics (2017) 213 (cit. on p. 124).
- <sup>166</sup>T. Bayes Rev., *An essay toward solving a problem in the doctrine of chances*, Phil. Trans. Roy. Soc. Lond. **53** (1764) 370–418 (1764) (cit. on p. 124).
- <sup>167</sup>I. Connelly, *Performance and calibration of b-tagging with the ATLAS experiment at LHC Run-2*, EPJ Web Conf. **164** (2017) 07025, edited by L. Bravina, Y. Foka and S. Kabana (2017) (cit. on p. 133).
- <sup>168</sup>T. Chen and C. Guestrin, ‘XGBoost’, Proceedings of the 22nd ACM SIGKDD international conference on knowledge discovery and data mining (2016) (cit. on p. 134).

<sup>169</sup>J Zimmermann,  
*Statistical learning methods: basics, control and performance*,  
Nuclear Instruments and Methods in Physics Research Section A:  
Accelerators, Spectrometers, Detectors and Associated Equipment **559**  
(2006) 106–114 (2006) (cit. on p. 135).

## **Summary of the results**



# Recerca de la producció associada de bosó de Higgs i un quark top amb dos leptons i tau hadrònic a l'estat final

## 1 Marc teòric

### 1.1 El Model Estàndard

Maybe, I could translate this for the SM summary:  
<https://www.quantamagazine.org/a-new-map-of-the-standard-model-of-particle-physics-20201022/>

### 1.2 La física del quark top

### 1.3 La física del bosó de Higgs

## 2 Dispositiu experimental

El treball desenvolupat al doctorat s'emmarca dins del detector ATLAS, que opera registrant les dades de les col·lisions del gran col·lisionador d'hadrons (LHC). El nom ATLAS prové de l'acronim angles d'un aparell toroidal del LHC.

Aquestes eines pertanyen al centre europeu de recerca en física de partícules, popularment conegut com a CERN.

### 3 L'experiment ATLAS del LHC al CERN

#### 3.1 El gran col·lisionador d'hadrons

#### 3.2 El detector ATLAS

### 4 Mesura de la polarització del quark top al canal-*t*

Mesura d'observables sensibles a la polarització del quark top

#### 4.1 Selecció d'esdeveniments

#### 4.2 Estimació del fons

#### 4.3 Fonts d'incertesa

#### 4.4 Resultats

### 5 Recerca de processos $tH$ amb un estat final $2\ell + 1\tau_{\text{had}}$

#### 5.1 Selecció d'esdeveniments

#### 5.2 Estimació del fons

#### 5.3 Fonts d'incertesa

#### 5.4 Resultats

### 6 Conclusions





# Contraportada

The discovery of a Higgs boson by the ATLAS and CMS experiments in 2012 opened a new field for exploration in the realm of particle physics. In order to better understand the Standard Model (SM) of particle physics, it is imperative to study the Yukawa coupling between this new particle and the rest of the SM components. Among these, of prominent interest is the coupling of the Higgs boson to the top quark ( $y_t$ ), which is the most massive fundamental particle and, consequently, the one with the strongest coupling to the Higgs

The direct measurement of  $y_t$  is only possible at LHC via two associated Higgs productions; with a pair of top quarks ( $t\bar{t}H$ ) and with single-top quark ( $tHq$ ). While the  $t\bar{t}H$  permits a model-independent determination of the magnitude of  $y_t$ , the only way of directly measuring its sign is through the  $tHq$  production. This is due to the fact that the two leading-order Feynman diagrams for  $tHq$  production interfere with each other depending on  $y_t$  sign. Current experimental constraints on  $y_t$  favour the SM predictions, even though an opposite sign with respect to the SM expectations is not completely excluded yet.

In this work it is presented a search for the production of a Higgs boson in association with a single-top quark in a final state with two light-floavoured-charged leptons and one hadronically decaying tau lepton (named  $2\ell + 1\tau_{\text{had}}$  channel). This analysis uses an integrated luminosity of  $139 \text{ fb}^{-1}$  of proton-proton collision data at centre-of-mass energy of  $13 \text{ TeV}$  collected by ATLAS during LHC Run 2.

This search is exceptionally challenging due to the extremely small cross section of the  $tHq$  process ( $70 \text{ fb}^{-1}$ ) in general and, more particularly, the the  $2\ell + 1\tau_{\text{had}}$  final-state channel, which only accounts for a 3.5% of the total  $tHq$  production.

Because of this, the separation of the  $tHq$  signal events from background events is done by means of machine-learning (ML) techniques using boosted-decision trees (BDT) to define both signal and control regions. The most relevant background processes are those related to top-pairs produc-

tion (such as  $t\bar{t}$ ,  $t\bar{t}H$ ,  $t\bar{t}Z$  and  $t\bar{t}W$ ),  $Z$ -boson plus jets and single-top processes.

Significant suppression of the background events with jets wrongly selected as leptons is achieved by demanding electrons and muons to pass strict isolation requirements. Simultaneously, hadronic-tau leptons are demanded to pass the requirement of the recurrent-neural-network-based discriminator to reduce misidentifications from jets.

The reconstruction of the events is also enhanced by similar ML methods since in the scenario in which the light-flavour leptons have the same sign, in principle, it is not possible to determine which lepton is originated from the Higgs boson and which from the top quark.

The possible observation of an excess of signal events with respect to the SM predictions, would be a clear evidence of new physics in terms of  $\mathcal{CP}$ -violating  $y_t$  coupling.

Additionally, the contribution to the single-top-quark polarisation first measurement is presented as well. In this other analysis the components of the full polarisation vector of the top quark are measured taking advantage of the peculiarities of the single-top-quark decay. Benefitting from the fact that the top quark lifetime is smaller than the depolarisation timescale, the decay products preserve the spin information of the top quark. Via angular distributions, it is measured in the top-quark rest frame.